Preparation, structure and reactivity of functionalized zirconium metal-organic frameworks

Dissertation for the degree of Philosophiae Doctor

Sigurd Øien-Ødegaard

Department of Chemistry

Faculty of Mathematics and Natural Sciences

University of Oslo

2016

Series of dissertations submitted to the
Faculty of Mathematics and Natural Sciences, University of Oslo
No. 1786

ISSN 1501-7710

Cover: Hanne Baadsgaard Utigard.
Print production: Reprosentralen, University of Oslo.

Foreword

In this Ph.D. thesis I summarize the results from four years of investigations of zirconium based metal-organic frameworks (Zr-MOFs). The work has been financed by the Climit and ProDIA grants, and the work has mainly been carried out at the Department of chemistry at the University of Oslo.

I am very grateful to have had the opportunity to work as a Ph.D. candidate, and to be able to pursue the topics of my interest. I have had the pleasure to cooperate with a group of talented chemists, physicists and chemical engineers, all of whom have provided useful guidance and a good working environment.

Single crystal X-ray diffraction has been a great passion of mine while I've worked with MOFs. In addition, I've become very fond of working at synchrotrons, large experimental facilities dedicated to cutting-edge scientific discoveries. The multinational communities formed at the beam lines are unique. Since 2013, I have had the pleasure of being one of the department's crystallographers, and get a sneak peek into many of the departments' research groups. Nothing beats the expression on a colleague's face when you show a totally different molecular structure than they expected!

My first encounter with the MOF UiO-66 was at one of the last lectures in introductory inorganic chemistry in the fall of 2009. It was instant attraction, a combination of the sheer beauty of complex crystal structures, and a material that is basically a molecular building toy. I feel incredibly privileged to have a job where I get to manipulate such a complex material at the atomic level.

I would like to thank my wonderful wife, Carine, for loving support! You inspire me every day, and I wouldn't be where I am if it wasn't for you. I want to thank my family who have always supported and encouraged my interest in math and natural science. I am also very grateful for all the great colleagues I've had in the catalysis group. Karl Petter, I think you have been an ideal supervisor for me, allowing me to follow the subjects I find fascinating. Mats, as my co-supervisor you have been an inspiration as a leader of your golden group. Carlo and Silvia, thanks for your hospitality, and for showing me the wonderful world of synchrotrons. Knut, without your linkers this thesis would've been a slim pamphlet. To the guys in the MOFfice, Greig, Sachin and Boris, it's been insanely great.

Table of contents

Foreword III

Table of contents IV

List of publications V

Author's contribution VI

Papers not included VII

Scope VIII

List of abbreviations and symbols X

1 Introduction 1

1.1 Metal-organic frameworks 1

2 Experimental methods 11

2.1 Zr-MOF synthesis 11

2.2 Single crystal X-ray diffraction 14

2.3 X-ray absorption spectroscopy 19

3 Results and discussion 22

3.1 Crystallization, structure and defects 22

3.2 Properties of UiO-67 type MOFs 34

3.3 Reactivity of Pt and Cu sites in UiO-67 55

4 Conclusions and outlook 74

4.1 Method development 74

4.2 Results 74

4.3 Outlook 76

References 77

Appendices 86

A1. Synthesis of reported samples 86

A2. SC-XRD experimental notes 89

A3. Published articles 101

List of publications

Paper I: *Detailed structure analysis of atomic positions and defects in zirconium metal-organic frameworks*, Sigurd Øien; David Wragg; Helge Reinsch; Stian Svelle; Silvia Bordiga; Carlo Lamberti; Karl Petter Lillerud. Crystal Growth & Design **2014**, *14,* 5370-5372.

Paper II: *Efficient, Scalable Syntheses of Linker Molecules for Metal-Organic Frameworks*, Knut T. Hylland; Sigurd Øien-Ødegaard; Karl Petter Lillerud; Mats Tilset. Synlett: Accounts and Rapid Communications in Synthetic Organic Chemistry **2015**, *26*, 1480 - 1485.

Paper III: *UiO-67-type Metal−Organic Frameworks with Enhanced Water Stability and Methane Adsorption Capacity*, Sigurd Øien-Ødegaard; Boris Bouchevreau; Knut T. Hylland; Lianpao Wu; Richard Blom; Carlos Grande; Unni Olsbye; Mats Tilset; Karl Petter Lillerud. Inorganic Chemistry **2016**, *55*, 1986 – 1991.

Paper IV: *Probing reactive platinum sites in UiO-67 zirconium metal-organic frameworks*, Sigurd Øien; Giovanni Agostini; Stian Svelle; Elisa Borfecchia; Kirill A. Lomachenko; Lorenzo Mino; Erik Gallo; Silvia Bordiga; Unni Olsbye; Karl Petter Lillerud; Carlo Lamberti. Chemistry of Materials **2015,** *27*, 1042-1056.

Paper V: *Exploring structure and reactivity of Cu-sites in functionalized UiO-67 MOFs*, Luca Braglia; Elisa Borfecchia; Lorenza Maddalena; Sigurd Øien; Kirill A. Lomachenko; Aram L. Bugaev; Silvia Bordiga; Alexander V. Soldatov; Karl Petter Lillerud; Carlo Lamberti. Catalysis Today **2016**, (available online, doi:10.1016/j.cattod.2016.02.039).

Author's contribution

Paper I: Performed synthesis of all samples. Application and reporting for synchrotron beam time. Performing all of the crystallographic experiments and data treatment. Performed TGA and PXRD measurements. Preparation of the manuscript and graphics.

Paper II: Performed all SC-XRD experiments. Participated in planning, manuscript preparation and revision.

Paper III: Performed synthesis of all MOFs. Performed TGA, N_2 adsorption, PXRD and SC-XRD measurements. Prepared the manuscript and graphics.

Paper IV: Performed synthesis of all samples. Performed all single crystal diffraction, PXRD, adsorption and NMR experiments. Participated in XAS measurements. Participated in manuscript preparation and revision.

Paper V: Performed synthesis of all MOFs. Performed synthesis and SC-XRD characterization of Cu reference compound. Participated in the preparation of manuscript and graphics (synthesis and crystallography part).

Papers not included

Di-μ-chlorido-bis[(2,2'-bipyridine-5,5'-dicarboxylic acid-κ^2N,N')chloridocopper(II)] dimethylformamide tetrasolvate, Sigurd Øien; David Wragg; Karl Petter Lillerud; Mats Tilset. Acta Crystallographica Section E: Structure Reports Online **2013**, *69*, m73 – m74.

A gold exchange: A mechanistic study of a reversible, formal ethylene insertion into a gold(III)-oxygen bond, Eirin Langseth; Ainara Nova; Eline Aa. Tråseth; Frode Rise; Sigurd Øien; Richard H. Heyn; Mats Tilset. Journal of the American Chemical Society **2014**, *136*, 10104-10115.

Atomic layer deposition of sodium and potassium oxides: Evaluation of precursors and deposition of thin films, Erik Østreng; Henrik Sønsteby; Sigurd Øien; Ola Nilsen; Helmer Fjellvåg. Dalton Transactions **2014**, *43*, 16666-16672.

Small-molecule activation at Au(III): Metallacycle construction from ethylene, water, and acetonitrile, Marte S. Holmsen; Ainara Nova; David Balcells; Eirin Langseth; Sigurd Øien-Ødegaard; Eline Aa. Tråseth; Richard. H. Heyn; Mats Tilset. Dalton Transactions, **2016**, *45*, 14719-14724.

NMR spectroscopic investigations into the mechanism of absorption and desorption of CO_2 by (tris-pyridyl)amine Zn complexes, Bjørnar Arstad; Terje Didriksen; Morten Frøseth; Richard Heyn; Sigurd Øien-Ødegaard; Richard Blom. Journal of CO_2 utilization **2016** (submitted).

Scope

The scope of the work presented herein was primarily to synthesize a wide range of Zr-based metal-organic frameworks (MOFs), and investigate their performance as adsorbents and catalysts. This class of materials have been intensely studied due to their adsorption and catalytic properties, making them promising candidates for applications in catalysis, gas separation, gas storage etc.

However, in the early stages of the work it became apparent that we were lacking knowledge about fundamental features of these materials. The relationship between synthesis parameters and the MOFs' properties was poorly understood, and large variations were observed in respect to material quality and yields. In particular, the synthesized MOFs showed huge variations in their stability towards water. To elucidate this further, several investigations were initiated. The results presented in this Ph.D. thesis regarding fundamental properties of Zr-MOFs are limited to synthesis optimization and crystallographic investigations. Calculations, gravimetric analysis, and investigations of how the synthesis conditions affect the porosity and stability of UiO MOFs have been explored by others in parallel.

Zr-MOF functionalization remained the primary aim of this Ph.D. thesis. The research has mainly been directed towards understanding the behavior of different functional groups incorporated into the MOF structure. UiO-67 (Figure 1) was used as the base MOF structure for the majority of the author's published work. This structure was chosen for its ability to accommodate a wide range of organic functional groups and metal complexes.

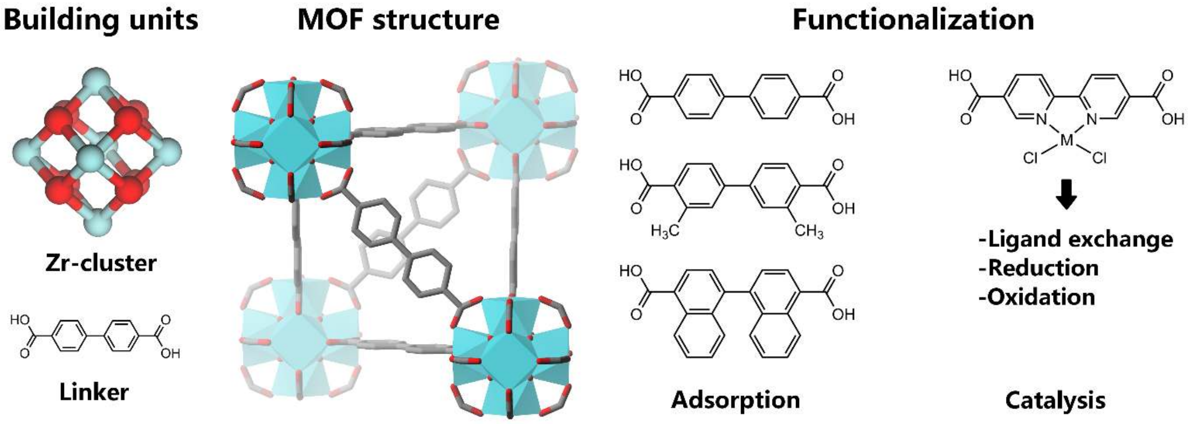

Figure 1.Graphical summary of the main topics in this Ph.D. thesis: The constituents and partial structure of UiO-67, which is the most investigated MOF in this work, where the Zr atoms are shown as green balls and square antiprisms, while carbon and oxygen atoms are shown as grey and red ball and stick models, respectively. As means of functionalization, UiO-67 has been synthesized with the linkers biphenyl-4,4'-dicarboxylic acid (H_2bpdc), 3,3'-dimethylbiphenyl-4,4'-dicarboxylic acid (Me_2-H_2bpdc),1,1'-binaphthyl-4,4'-dicarboxylic acid (H_2bndc). In order to impart catalytic function to the material, metal complexes of 2,2'-bipyridine-5,5'-dicarboxylic acid (H_2bpydc) have also been used as linkers.

This thesis is organized in three main chapters, two introductory chapters providing a brief discussion of the literature background (chapter 1) and the main experimental methods used (chapter 2), and a chapter summarizing the results reported in the author's published works (chapter 3). Since the work is rather diverse, the results are organized in three sections:

(1): Crystal growth optimization of the MOFs UiO-66 and UiO-67, and subsequent single crystal X-ray diffraction studies were performed to obtain detailed crystal structures, in particular information about defects in Zr-MOFs, as these are a very important feature of these materials.

(2): Several UiO-67 analogues have been synthesized in order to study linker-dependent properties, mainly focusing on water stability and adsorption properties. Adsorption and diffraction studies have been performed to explore the relationship between structure and properties in these MOFs.

(3): Pt and Cu complexes have been incorporated into the structure of UiO-67, to study their reactivity as potential catalysts. In situ X-ray absorption spectroscopy has been used to study the state of these incorporated metals at various stages: In the as-synthesized MOFs, under various "activation" treatments, or in reaction with substrates of interest.

List of abbreviations and symbols

ADP	Anisotropic displacement parameter (of atoms in crystal structures).
BET	Brunauer–Emmett–Teller theory of specific surface area determination.
DFT	Density Functional Theory
DMF	Dimethylformamide
EXAFS	Extended X-ray Absorption Spectroscopy Fine Structure
FT-IR	Fourier Transform Infrared Spectroscopy
MOF	Metal-Organic Framework
MS	Mass Spectrometry
R_1	Crystallographic R-factor from unwheighted structure factors
PSE	Postsynthetic exchange
PSF	Postsynthetic functionalizationh
PSM	Postsynthetic modification
PXRD	Powder X-ray Diffraction
SBU	Secondary Building Unit
SC-XRD	Single-Crystal X-ray Diffraction
TGA	Thermogravimetric Analysis
TPR	Temperature Programmed Reduction
wR_2	Crystallographic R-factor from wheighted squared structure factors
XANES	X-ray Absorption Near Edge Structure
XAS	X-ray Absorption Spectroscopy
Å	Ångstrøm (10^{-10} m)
µm	micrometer (10^{-6} m)
λ	Wavelength
ρ	Density (in this text, electron density in crystalline solids)
θ	Angle of diffraction
σ	Standard deviation

1 Introduction

1.1 Metal-organic frameworks

A metal-organic framework (MOF) is a solid which consists of a two- or three-dimensional coordination network with organic ligands, and also contains potential voids.[1] The inorganic constituents of a MOF is called secondary building units (SBUs), and they are interconnected by the organic ligands to form a network structure. According to this definition, MOFs can be either crystalline or amorphous. Schematics of two possible MOF structures are shown in Figure 2.

The SBUs are typically small clusters or infinite chains of oxide-sharing metal ions in a stable oxidation state. Other types of SBUs are also frequently reported, such as single metal ions. The organic ligands, (colloquially termed "linkers" or "spacers" in the literature) are molecules with multiple coordinating functional groups. These are very often Lewis bases like carboxylates,[2,3] imidazolates[4-6] or amines.[7,8] Carboxylate linkers are described interchangeably in their acid and carboxylate forms; these compounds are almost exclusively prepared and used for MOF synthesis in the acid form, but as part of MOFs they exist almost exclusively as carboxylates due to the formation of metal-carboxylate bonds.

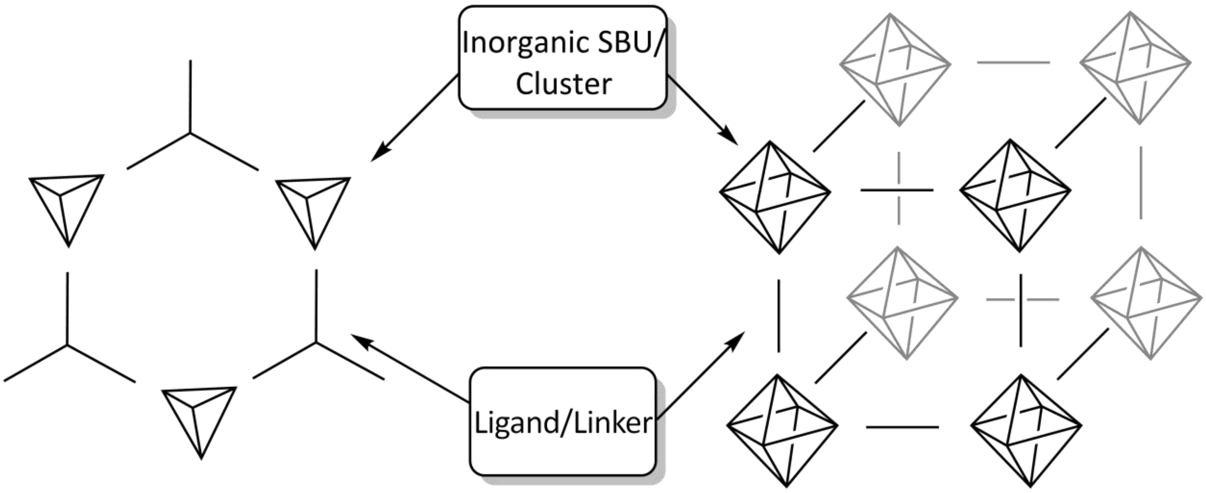

Figure 2. Schematic representation of two MOF structures, one constructed from tetrahedral inorganic SBUs and trigonal planar linkers (left) and one from octahedral inorganic SBUs and linear linkers (right).

MOFs form network structures based on the connectivity of the SBUs, and MOF structures are often described with their network topology.[9] The study of network structures (including MOF structures) is called reticular chemistry (from Latin *reticularis* meaning “little net”), and the term “isoreticular MOFs” is used to describe MOFs with the same network topology. Thus, the linkers in a series of isoreticular MOFs are different chemical compounds, often with different geometric extension, but with the same connectivity number. Notable examples of isoreticular MOFs include the IRMOF (IsoReticular Metal-Organic Framework)[10] and UiO (Universitetet i Oslo)[11,12] series (Figure *3*).

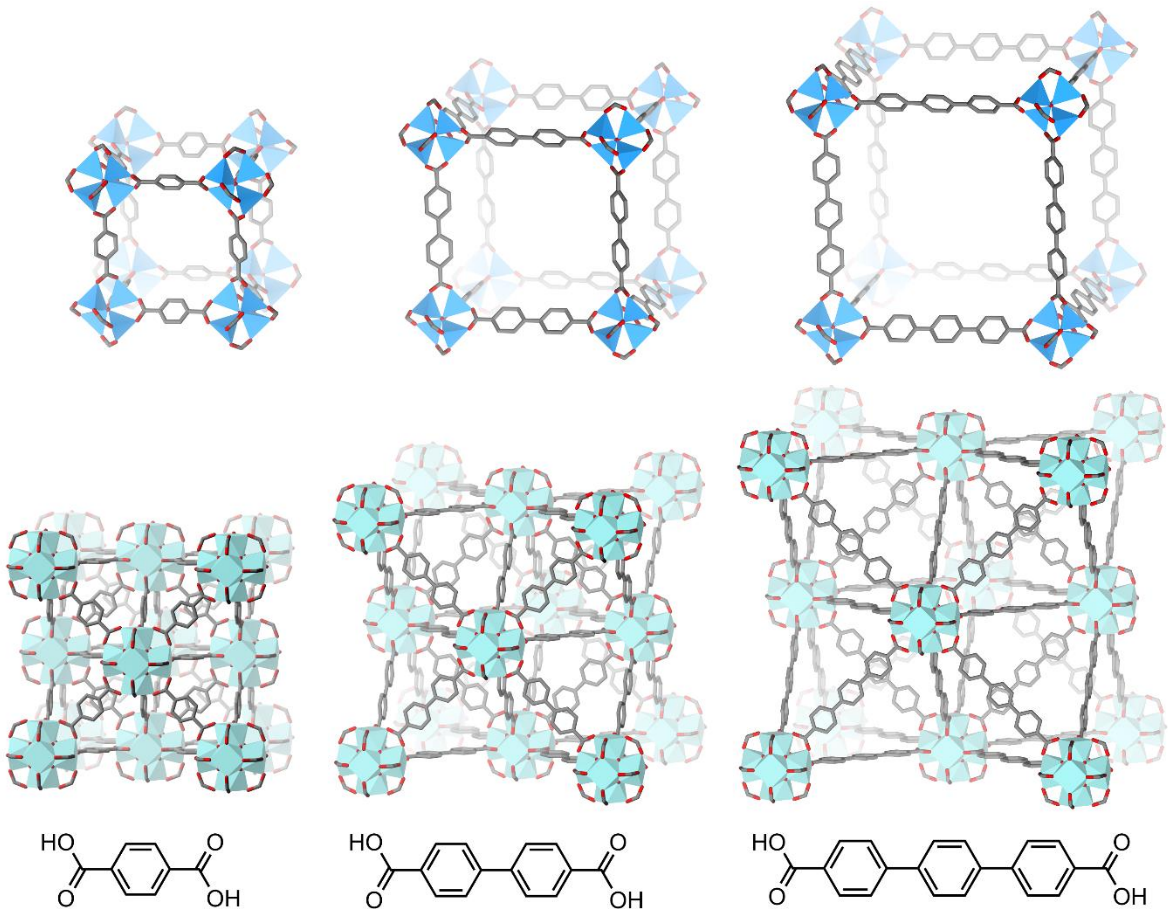

Figure 3. Two series of isoreticular MOFs, constructed from Zn_4O^{6+} and $Zr_6O_4(OH)_4^{12+}$ inorganic SBUs, and linear dicarboxylic acid linkers. Zn atoms are shown as blue tetrahedra, Zr atoms as green square antiprisms, C aroms as grey and O atoms as red sticks. H atoms are omitted for clarity. Top row: MOF-5/IRMOF-1, IRMOF-9 and IRMOF-16. Middle row: UiO-66, UiO-67 and UiO-68. Bottom row: Bond-line structures of the linkers terephthalic acid (H_2bdc), biphenyl-4,4'-dicarboxylic acid (H_2bpdc) and p-terphenyl-4,4’’-dicarboxylic acid (H_2tpdc).

An intrinsic feature of MOFs is the (potential) presence of voids inside the structure.[1] The size and shape of the pores are determined by the dimensions of the linker, and by the network topology of the MOF, as shown in Figure 3 for MOFs with different network topologies.

The flexible composition of MOFs allows for almost perfect control over pore size and pore surface properties. A wide range of functional groups can be incorporated onto the linkers, thereby altering the properties of the MOF. As an example, a small selection of linkers with the structural backbone of terephthalic acid is shown in Figure 4, all of which have been used to synthesize isostructural MOFs.[3] Exploiting this potential for chemical diversity, MOFs are frequently reported as well-performing materials in catalysis and gas adsorption.[13,14]

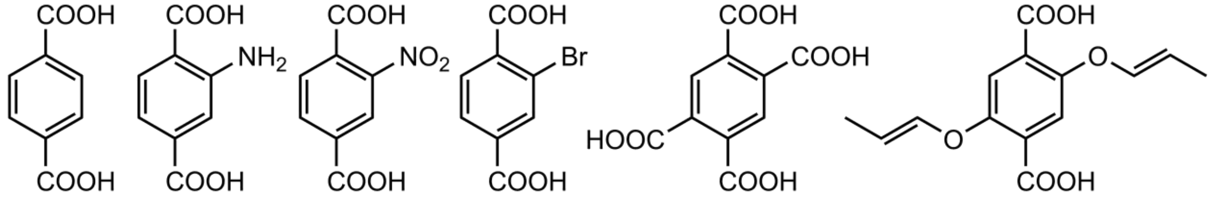

Figure 4. A selection of linkers that can be used to form isostructural MOFs with different properties, with the backbone of terephthalic acid. From left to right: Terephthalic acid (H_2bdc), aminoterephthalic acid (H_2bdc-NH_2), nitroterephthalic acid (H_2bdc-NO_2), bromoterephthalic acid (H_2bdc-Br), 1,2,4,5-benzenetetracarboxylic acid (H_2bdc-$(COOH)_2$) and 2,5-bis((prop-1-en-1-yl)oxy)terephthalic acid.

1.1.1 Structure of Zr-based MOFs

The first MOFs synthesized with a Zirconium-based SBU were reported in 2008, and were found to be remarkably stable, both chemically, mechanically and thermally (relative to other known MOFs at the time).[15] The MOFs consist of 12-connected $Zr_6(\mu^3\text{-}O)_4(\mu^3\text{-}OH)_4(COO)_{12}$, clusters and the linkers H_2bdc (UiO-66), H_2bpdc (UiO-67) and H_2tpdc (UiO-68, Figure 3). The stability of these MOFs originate from the strength of the Zr – O bonds, which are not easily hydrolyzed like e.g. Zn – O bonds found in the IRMOFs, and the high connectivity number of the cluster.[15-17]

The SBU of the UiO MOFs, based on 6 Zr(IV) ions arranged in an octahedron, occur in the majority of reported Zr-MOFs.[18,19] It has been known as a molecular cluster since 1997.[20] Each of the 8 facets of the Zr_6 octahedron is capped by a (μ^3-O) or (μ^3-OH), the OH situated farther from the centroid of the cluster than the O. The 4 OH groups are tetrahedrally arranged with respect to each other (as shown in Figure 5), as this is the most stable arrangement.[21] Each neighboring Zr – Zr pair is bridged by a carboxylate, meaning that 12 carboxylates coordinate to each cluster. If one regards the carbon atom of each carboxylate as a vertex of a polyhedron, then the cluster forms a regular cuboctahedron.

One interesting feature of cluster-based Zr-MOFs is that the Zr_6 cluster can undergo thermal dehydration by the following reaction:

$$Zr_6O_4(OH)_4 \overset{\Delta}{\leftrightarrow} Zr_6O_6 + 2\;H_2O$$

This results in a cluster of the same overall cuboctahedral connectivity, where the Zr-ions change from 8-coordinated square antiprismatic to a slightly distorted monocapped trigonal prismatic 7-coordination (Figure 5). The dehydrated cluster is truncated, with non-equal Zr – Zr distances, as determined by X-ray absorption spectroscopy (XAS), powder X-ray diffraction (PXRD) and periodic density functional theory (DFT) calculations.[22] The reaction is fully reversible.[15]

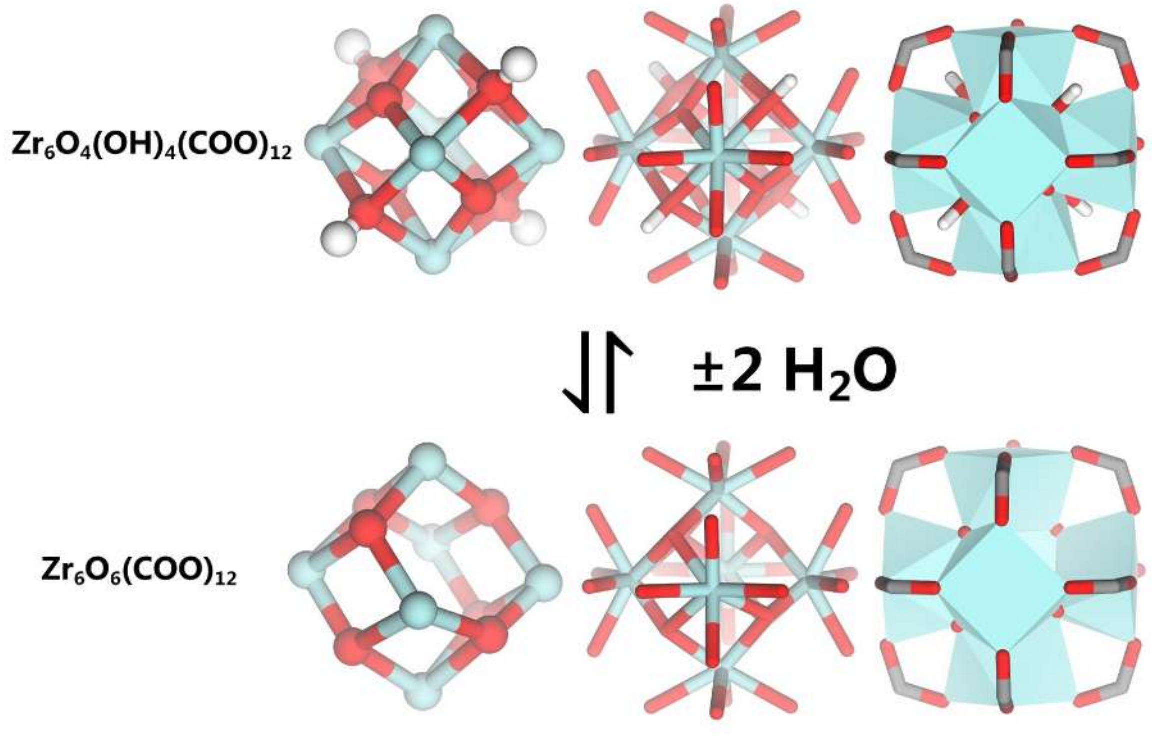

Figure 5. Representations of the Zr_6-cluster in its hydrated (top) and dehydrated (bottom) forms, Zr atoms green, O red, C gray and H white. From left to right: ball and stick representation of the inner cluster, only Zr and μ^3-O(H); stick representation with all Zr coordinated O atoms to show the full coordination environment of Zr; Polygon representation of full cluster with carboxylate carbon atoms.

When forming MOFs with linear ditopic linkers, as in the UiO series, the framework topology is fcu. The UiO MOFs thus feature two tetrahedral cages and one octahedral cavity per cluster (Figure 6).

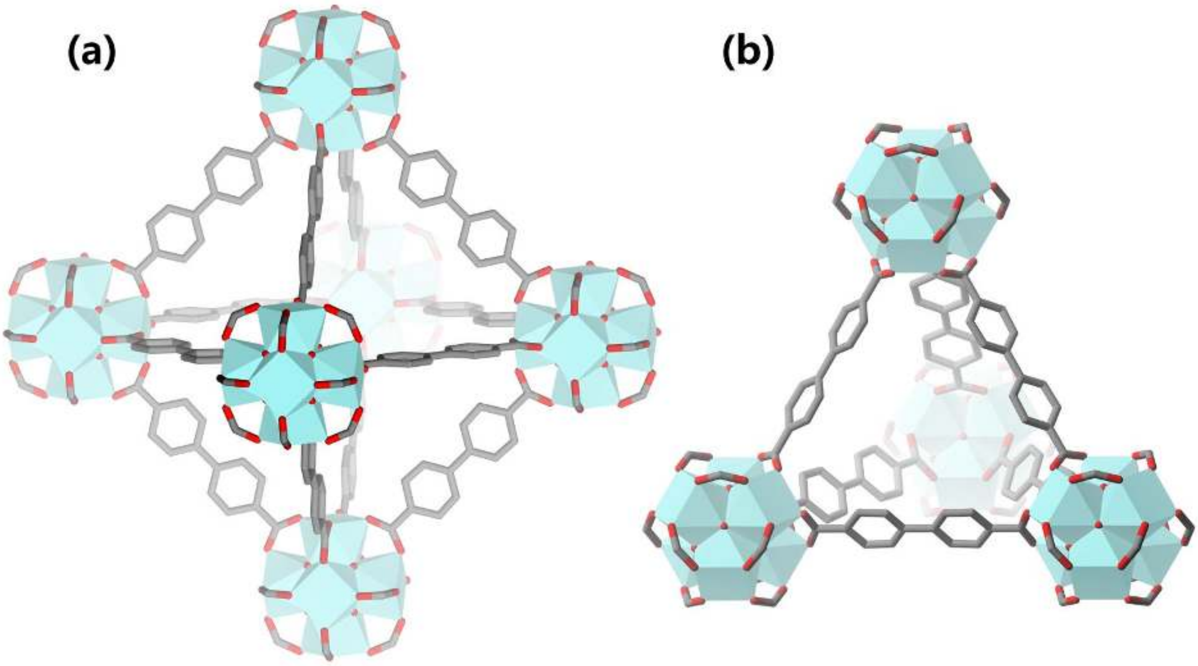

Figure 6. Representation of the two types of cages in UiO-67 (and thus all MOFs with fcu topology). (a): the octahedral cage and (b): the tetrahedral cage.

The Zr_6-cluster occurs in stable MOFs where 6, 8, 10 or 12 linkers are coordinated to each cluster, each of these forming different network topologies (Figure 7).[18,23] The Zr-capping fragments in the MOFs with less than 12 linkers to each cluster may be monocarboxylates,[24] water/hydroxide pairs[23] or other anions such as sulfate.[25,26]

Due to their favorable properties, Zr based MOFs were among the most frequently published by 2012,[19] with over 80 different Zr-MOF structures currently known (as of February 2016).[18] They have been shown to be stable, compatible with many organic linkers, and perform well as catalysts[27,28] and adsorbents.[23,29]

Other than the UiO MOFs, notable examples of cluster based Zr-MOFs include PCN-222[28] and MOF-525/545[30] with 4-coordinated planar porphyrinic linkers, porous interpenetrated Zr organic frameworks (PIZOFs)[31] which form two-fold interpenetrated networks, and several UiO-68 and UiO-69 (quaterphenyl based)[32] analogues.

A different class of Zr-MOFs, MIL-140 type MOFs (Figure 7), can be obtained from the same constituents as in the cluster-based MOFs based on the same linkers, by changing the synthesis conditions. The structure is based on infinite chains of facet sharing ZrO_7 units. They contain long channels in one direction rather than having an open framework structure as the cluster-based Zr-MOFs.[33]

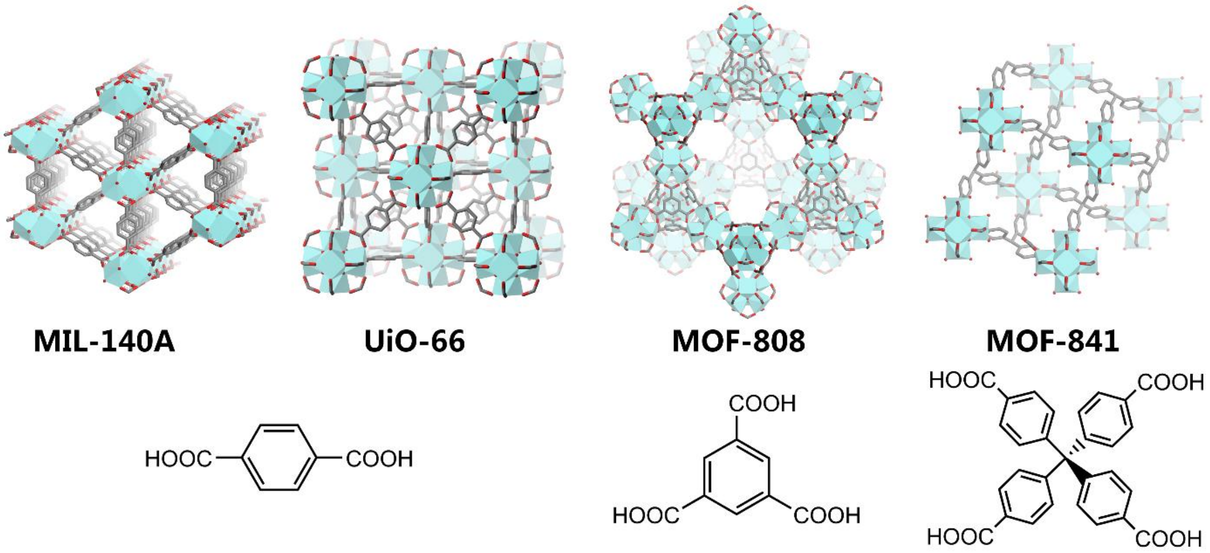

Figure 7. Four different Zr MOFs, depicted with their (partial) crystal structures (top) and their respective linkers (bottom). MIL-140A consists of infinite chains of facet sharing ZrO_7 units, whereas the other three are based on the $Zr_6O_4(OH)_4$ cluster. MOF-808 and MOF-841 consist of 6-coordinated and 8-coordinated Zr clusters respectively.

1.1.2 Defects in Zr-MOFs

Defects have great impact on the properties of Zr-MOFs, including stability, porosity and catalytic activity, and the study of defects in UiO-66 has been a very active field in recent years.[34-37] The two main types of defects in Zr-MOFs are cluster and linker vacancies, also referred to as "missing cluster" or "missing linker" defects. The notion of missing linker defects in UiO-type MOFs was first reported by Valenzano et al., by pointing out disproportionate weight loss of aromatics by TGA-MS, accompanied by the observation of absorption bands associated with OH groups by FT-IR at very high temperatures, where adsorbed water should be absent.[22] It was later reported that the amount of defects increases when acetic acid is used as a synthesis additive (the addition of monodentate ligands in the synthesis of MOFs is termed "modulation" and is discussed in section 2.1.2).[37] Recently, missing cluster defects have been identified in UiO-66 based on otherwise forbidden Bragg peaks appearing in the diffraction patterns of highly defective samples.[38]

The synthesis conditions leading to more or less defective UiO-66 samples are now better understood.[35,39] The relationship between defects and stability in particular has been discussed in great detail by Shearer et al.[35] Indeed, it has been shown that UiO-66 has a very high tolerance of defects, and unless extraordinary conditions are applied there will be 1-2 missing linkers per Zr cluster in UiO-66 as synthesized. Considering that stable Zr-MOFs are formed with clusters coordinating to just 6 linkers, it is not surprising that UiO-66 can be formed with 10 linkers bound to each cluster.

1.1.3 Mixed linker MOFs

MOFs can be synthesized using different linkers with the same structural backbone to obtain a MOF with a mixture of the two linkers in the same crystal structure (see Figure 8 for an example). The resulting materials are termed "mixed linker MOFs". It has been shown that a MOF single crystal with the structural topology of MOF-5 can accommodate at least 8 different linkers.[40] Mixed-linker MOFs allow further control of pore size and chemical functionality. Such MOFs are often prepared simply by using a mixture of linkers in the synthesis, although they can also be obtained through other methods such as postsynthetic linker exchange.[41,42]

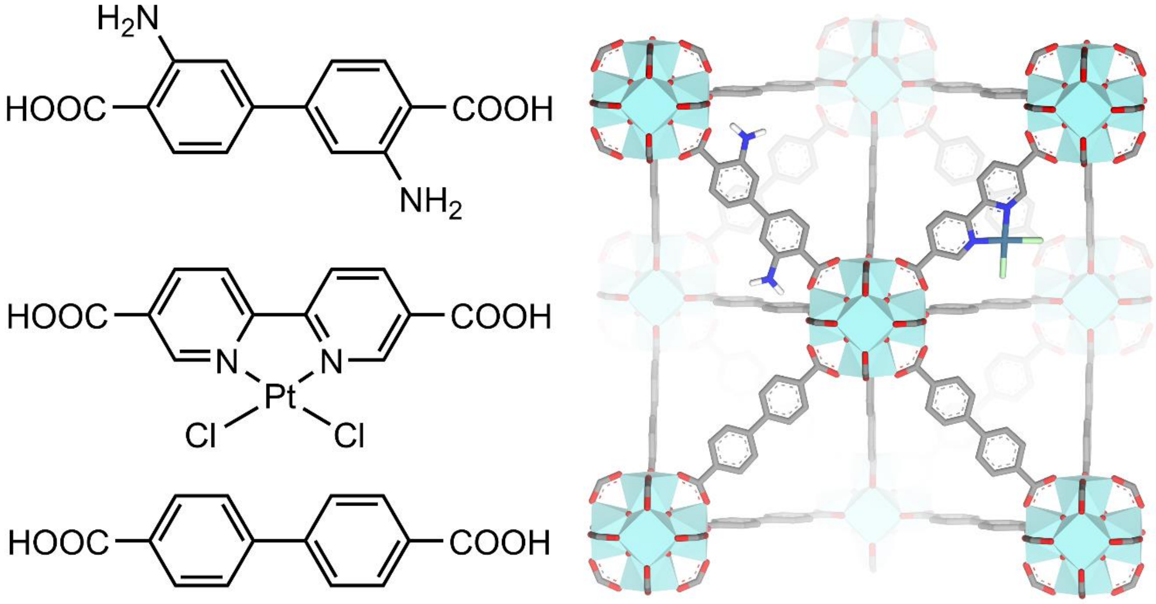

Figure 8. Example of a mixed linker MOF with UiO-67 topology consisting of three different linkers (right), and molecular structures of the linkers; 3,3'-diamino-4,4'-dicarboxylic acid (H_2bpdc-$(NH_2)_2$), 2,2′-bipyridine-5,5′-dicarboxylic acid-κ^{2}N,N′)dichloridoplatinum(II) ($PtCl_2$(H_2bpydc)) and H_2bpdc (left).

The numerous H_2bdc/H_2bdc-NH_2 frameworks are, perhaps, the most prominent mixed linker MOFs, shown for a large variety of SBUs. These MOFs form isostructural networks regardless of the ratio of H_2bdc/H_2bdc-NH_2, but display different stability, adsorption properties and catalytic activity.[43-45]

1.1.4 MOFs as adsorbents

The high porosity of MOFs, combined with their flexible chemical composition, makes them well-suited as adsorbents, both in gas storage and separation. At moderate pressures (for use in household applications, automobiles or similar), gas tanks filled with MOF can accommodate far more methane than empty tanks.[29,46] Moreover, the adsorption affinity can be adjusted by introducing functional groups that interact with the adsorbate. For example, it has been shown that the heat of methane adsorption (Q_{St}) can be increased by adding large aromatic groups to the MOF linkers.[47,48] MOFs containing polar functional groups, like amines or open metal sites (coordinative unsaturated sites, present in a range of MOFs including e.g. HKUST-1 (Figure 9), and many others), increase adsorption affinity to e.g. CO_2.[14]

The ability to incorporate a variety of functional groups in MOFs has led to extensive research of MOFs as selective adsorbents for gas separation applications such as pre- or post-combustion CO_2 capture,[49] water adsorption,[50] capture of toxic gases[51] and natural gas purification.[52] Inclusion of functional groups and pore size manipulation have also been used to improve selectivity for a range of substrates.[52-54]

Zr-MOFs are intensely studied for adsorption applications, as many other MOFs are limited by stability issues, for example instability to moisture, sulfur containing impurities, acids, and so on.[55] Intrinsically, Zr-MOFs do not contain readily accessible open metal sites, but it has been suggested that such sites can be introduced through missing linker defects, creating a coordination vacancy on the Zr cluster (Figure 9).[56,57] Recent work has shown that highly defective Zr MOFs exhibit increased porosity and adsorption capacity towards e.g. CO_2, but thorough characterization of such sites has not been performed.[37]

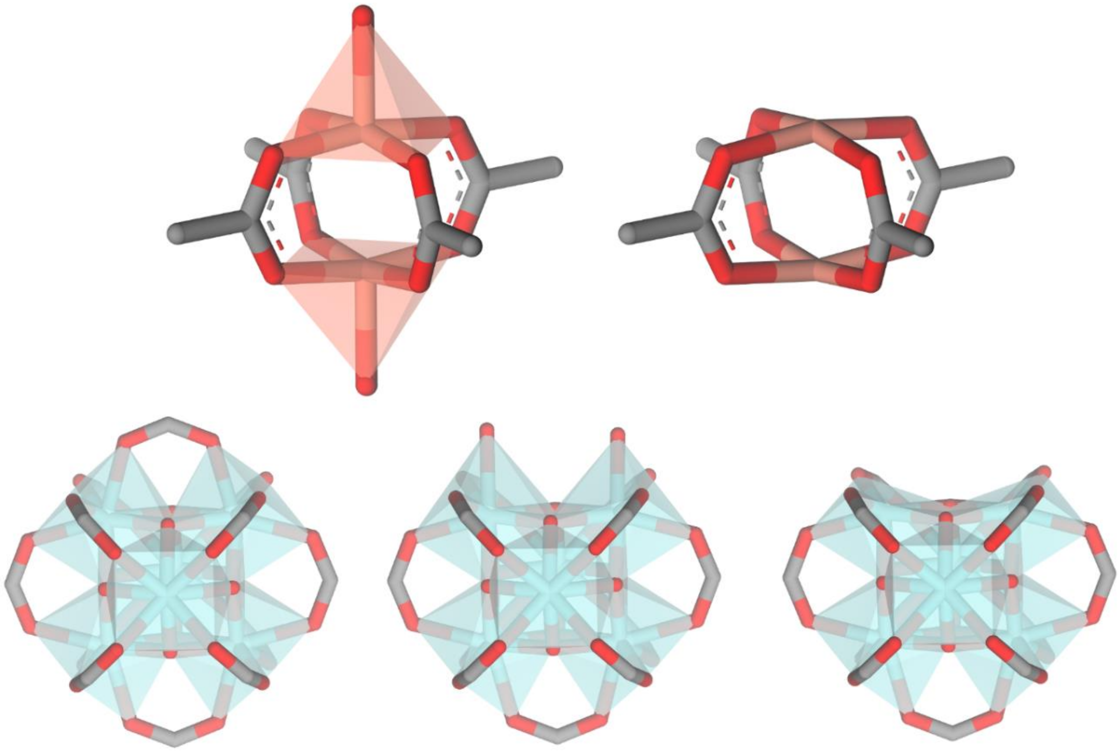

Figure 9. Stick models of the SBUs of HKUST-1, $Cu_2(COO)_4(L)_{0/2}$ (top left, Cu atoms shown as orange with transparent square pyramids to show coordination geometry)and UiO-66, $Zr_6O_4(OH)_4(COO)_{12}$. Vacant coordination sites are shown on the Cu cluster (top right). The Zr-cluster is shown in three conformations (bottom row): fully coordinated by carboxylate groups (left); containing one missing linker defect capped by an OH^-/H_2O pair (middle); hypothesized structure of a Zr-cluster with two vacant coordination sites (right).

1.1.5 MOFs as catalysts

One of the main areas of interest for MOFs is heterogeneous catalysis. Due to their diversity, ability to accommodate various functional groups and huge variations in pore size and topology, MOFs can in principle be designed to accommodate certain substrates, leading to improved selectivity.[58] There are several strategies to obtain catalytic sites in a MOF, e.g. open metal sites, inclusion of catalytically active linkers and immobilizing active catalysts in the MOF, such as nanoparticles (Figure 10b)[32,59,60] and enzymes.[61]

Open metal sites are found in several MOFs, and function as Lewis acid sites in catalytic reactions.[62] As already mentioned, Lewis acid sites can be introduced in Zr-MOFs through defects, and it has been demonstrated that catalytic activity of several reactions increases with increasing defect concentration.[57]

The inclusion of catalytically active linkers can be achieved by organic functional groups such as $-NH_2$ and $–SO_3H$ or, more commonly, metal linker complexes. For example, 2,2'-bipyridine-5,5'-dicarboxylic acid (H_2bpydc) has frequently been used as an anchoring point for catalytically active complexes. The popularity of this linker is due to its ability to form chelating coordination complexes with a wide range of transition metals, and its ability to form mixed linker MOFs together with the isostructural H_2bpdc (Figure 10a). MOFs prepared with a certain fraction of metalated H_2bpydc linkers have been used in a wide range of catalytic reactions such as water oxidation, CO_2 reduction, Suzuki-Miyaura cross-coupling and organic photocatalytic transformations by framework incorporated complexes of Pd, Ru, Re and Ir.[27,63,64]

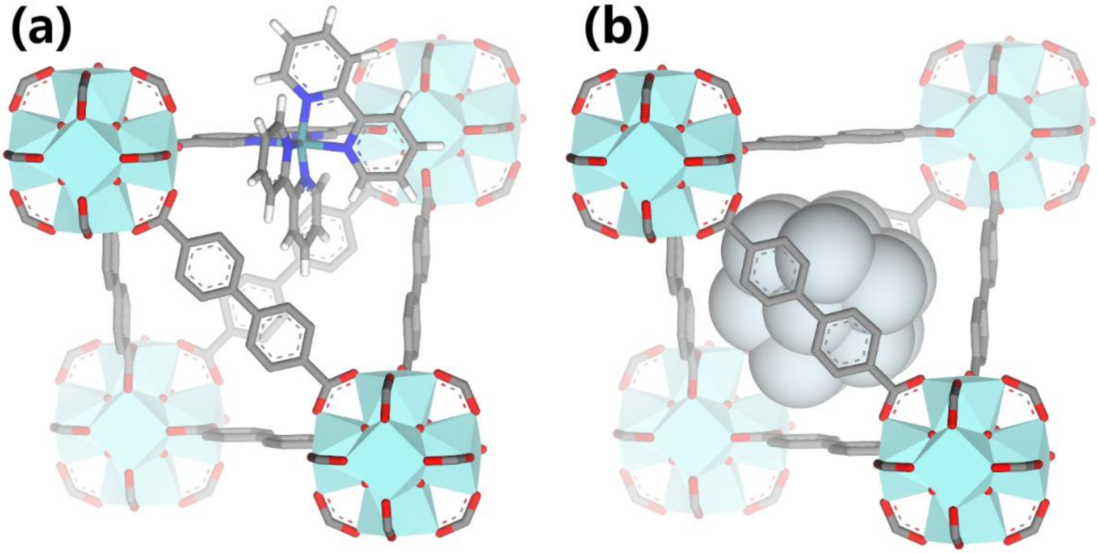

Figure 10. Two strategies for catalyst incorporation in UiO-67: **(a)** Incorporating a fraction of the linkers with a catalytically active complex, e.g. $Ru(bpy)_2(H_2bpydc)$. **(b)**: encapsulation of catalytically active metal nanoparticles inside the MOF.

2 Experimental methods

Several experimental methods have been of importance to this work. To highlight the author's contribution, MOF synthesis optimization and single crystal X-ray diffraction is presented in some detail. X-ray absorption spectroscopy (XAS) is a specialized technique, utilizing the brilliance of synchrotron X-rays, and a brief overview is presented.

2.1 Zr-MOF synthesis

Most of the synthesis optimization work performed as part of this Ph.D. thesis was focused on controlling the crystal size of Zr-MOFs in order to perform single crystal X-ray diffraction (SC-XRD) experiments. This section covers some aspects which were explored but not included in the published articles. Each parameter discussed in this chapter has been investigated in series of parallel one-parameter MOF syntheses. The results are summarized in section 3.1.1 on page 22. Specific synthesis procedures are reported in the supporting information of the respective articles, or in appendix A1 on page 86 for synthesis of samples only reported in the thesis.

Zr-MOF synthesis is normally performed in a solvothermal setup with dimethylformamide (DMF) as primary solvent, but other synthesis approaches for Zr-MOFs have also been reported, such as synthesis in water,[25,65] in continuous flow processes[66,67] and by mechanosynthesis.[68]

All Zr-MOF syntheses reported herein have been performed using DMF as solvent and $ZrCl_4$ as zirconium precursor. The idealized reaction equation for the synthesis of Zr-MOFs with 12-coordinated Zr_6 clusters and linear ditopic linkers is:

$$6\,ZrCl_4 + 8\,H_2O + 6\,H_2L \overset{\Delta}{\rightarrow} Zr_6O_4(OH)_4L_6 + 24\,HCl$$

Where H_2L is a dicarboxylic acid and L^{2-} is the corresponding dicarboxylate.

2.1.1 Reaction temperature

Crystallization temperatures from 70 to 180 °C were investigated. This was done with the aim of approximating the crystallization equilibrium point to allow for Ostwald ripening, i.e. the re-dissolving of nucleated particles. Investigations on UiO-66 has clearly shown that a higher synthesis temperature produced a less defective MOF,[35] but no systematic study has been conducted for UiO-67.

2.1.2 Modulators

Tsuruoka et al. were the first to report that MOF crystal growth can be altered by introducing a competing, single-coordinated ligand (called a "modulator").[8] Introducing a modulator to the synthesis was shown to slow crystal growth in those directions where the modulator and linker were competing for the same coordination sites at the SBU. When applied to MOFs where the SBU binds to different linkers in separate directions, modulation has been used to control the crystal morphology.

Modulation has been shown to be an important factor also in Zr-MOF synthesis. Larger crystals and highly crystalline MOF can be obtained under conditions where only amorphous phases are obtained otherwise.[8,69] It has later been shown that single crystals of Zr-MOFs can be obtained by modulated synthesis with formic acid,[23,70] acetic acid[30] and several amino acids.[71] Any monocarboxylic acid can be used as modulator, and its effect is determined by (among other factors) its relative affinity to Zr in respect to the linker at the synthesis conditions,[39] and its steric properties.

In this work, both modulator type and concentration have been investigated in the synthesis of UiO-66 and UiO-67. Benzoic acid has been the most frequently used due to its availability and solubility in various solvents. Formic acid, acetic acid, stearic acid, cyclohexanoic acid, phenylacetic acid, 4-nitrobenzoic acid and diphenylacetic acid were also used.

2.1.3 Crystallization vessel

During early attempts at benzoic acid modulated synthesis of UiO-67 in this work, it was noticed that the MOF crystallized as a film of intergrown crystallites on the glass walls and flask bottom. The film was also present at the inclining walls, but to a lesser extent than at the flask bottom. As the MOFs were mainly synthesized in glassware, different pretreatments were performed to alter the glass surfaces to decrease the density of nucleation sites. Among the treatments studied were prolonged soaking of the glassware in concentrated acidic or basic solutions. In other reports of Zr-MOF single crystal synthesis, anti-nucleation coatings has been used in attempts to obtain larger crystals.[23] The effect of a closed reaction vessel, i.e. a Teflon lined autoclave, was also investigated.

2.1.4 Other synthesis additives

Following a reported procedure for the synthesis of UiO-66 by Wiersum et al.[72], HCl was used as an additive, based on the assumption that the presence of HCl would shift the reaction equilibrium towards the reactant side and slow crystal growth. To investigate whether the increased acidity or the presence of additional chloride was the determining parameter, LiCl was investigated in parallel syntheses. LiCl was chosen as the chloride salt due to its superior solubility in DMF compared to other inorganic chlorides. Of course, another variable was introduced by the addition of Li^+ ions.

In an attempt to adjust the addition of water (which is required for the formation of Zr-MOFs), methanol was also tried as an additive instead of water. At the reaction conditions where modulator is present, methanol and the carboxylic acid react to form methyl carboxylate and water. It was investigated whether this could lead to increased crystal size due to water being formed in the reaction instead of an initially high concentration additive.

2.1.5 Other factors

MOF synthesis can be affected by many variables which are difficult to control. DMF is known to decompose at high temperatures in the presence of acids to form a wide range of byproducts.[73] Hereunder formic acid, which can act as a modulator in otherwise non-modulated syntheses.[74] The addition sequence of reagents will affect which partial reactions will be favored in the early stages of the synthesis, which may partly explain the sometimes unpredictable outcomes of MOF synthesis.

2.2 Single crystal X-ray diffraction

This section provides a short background on crystallography, considerations on how voids in a MOF crystal structure are treated during structure refinement, and crystal structure validation factors. Information about the execution of the specific experiments is found in the respective published articles or in the appendix A2 on page 89, along with a detailed overview of the different diffractometers used in this work.

2.2.1 Theoretical background

Single crystal X-ray diffraction (SC-XRD) is the principal method of determining crystal structures.

Crystallinity in solids is defined by the presence of three-dimensional order on the level of atomic dimensions. In a crystalline solid, a unit cell is defined as the smallest, regularly repeating material portion contained in a parallelepiped (with dimensions a, b and c, and angles α, β and γ) from which a crystal is formed by parallel displacements in three dimensions.[75] The contents of the unit cell are related by symmetry operations, mathematical operations that transform the crystal to a state that is indistinguishable from the starting state. The smallest set of atoms that can be used to describe the entire contents of the unit cell (in primitive stetting, using symmetry operations) is called the asymmetric unit. An example visualizing these concepts is shown in Figure 11, where the asymmetric unit is a molecule.

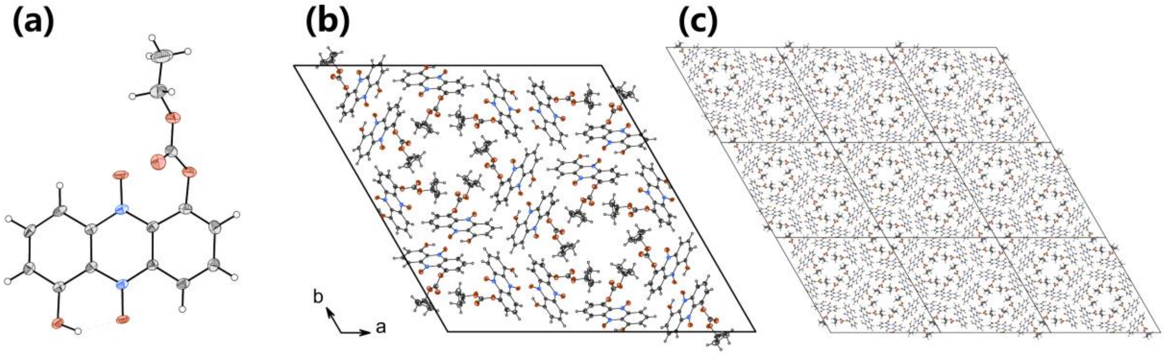

Figure 11. The crystal structure of a phenazine derivate. **(a)** The molecular structure of the asymmetric unit. **(b)** The unit cell viewed along the c-axis, which belong to the R-3 space group. The unit cell contains 18 molecules, generated from the three rhombohedral lattice nodes (0,0,0, 2/3,1/3,1/3 and 1/3,2/3,2/3) each intersected by a six-fold improper rotation (S6) axis. **(c)** A 3x3 array of unit cell, showing the translational symmetry in two dimensions.

From the perspective of X-ray crystallography, crystals are essentially a repeating pattern of electron density, which forms a one-dimensional density distribution pattern when projected onto an arbitrary vector in the unit cell. When this density distribution pattern coincides with a set of lattice planes that are expressed by the lattice parameters of the unit cell, and obey the same translational symmetry, diffraction of X-rays is observed at an angle given by Bragg's law; $n\lambda = 2d_{hkl} \, sin \, \theta$. It can be shown that this condition is met when the plane vector in real space is a node in the reciprocal unit cell lattice. The planes in real space are by convention named Miller planes, and the inter-planar distances in a real crystal is termed d_{hkl}. The nodes in the reciprocal lattice each correspond to a set of periodic, parallel Miller planes. They are indexed by the reciprocal lattice vectors **h**, **k** and **l**, termed Miller indices. Thus, each of the observed Bragg reflections can be assigned a unique index hkl, describing the Miller planes from which the reflection originated. A properly executed SC-XRD experiment provides a three-dimensional diffraction pattern consisting of the intensities (with standard deviations) of all the allowed Bragg reflections of the sample.

A number of corrections (including an orientation-dependent scale factor and corrections for absorption and X-ray polarization) are applied to the recorded reflection intensities to obtain the square amplitudes of the structure factors ($|F_{hkl}|^2$). The electron density of the unit cell in real space, ρ(xyz), is obtained by Fourier transform:

$$\rho(xyz) = \frac{1}{V} \sum_{\substack{-\infty \\ hkl}}^{+\infty} |F_{hkl}| \, e^{-2\pi i[hx+ky+lz-\phi(hkl)]}$$

where V is the unit cell volume and ϕ is the phase (relating the positions of electron density planes to the unit cell). For a thorough introduction, beyond the scope of this chapter, the reader is referred to texts describing the fundamentals of X-ray scattering.[76]

2.2.2 Structure solution and refinement

The crystal structure is obtained by assigning a phase to each reflection, and then assigning atoms at positions in the unit cell based on the position and magnitude of electron density obtained by Fourier transform of the structure factors. Iterative algorithms such as direct methods or charge flipping are commonly used for this.[77] Cycles of structure refinement are then performed (normally using least-squares minimization between the observed and calculated structure factors) until the refinement converges. The model is gradually improved by adjustment of atom positions or anisotropic displacement parameters (ADP).

The most frequently used structure refinement algorithm, SHELXL, uses spherical and/or ellipsoid shapes for the electron densities of the atoms in the structure, where the density distribution is given by the form factor of the element.[78] If an atom vibrates about a point instead of freely, the shape of the electron density will be bent, and may cause faulty estimates of bond lengths. This form of constrained vibration is called libration, and is present in most Zr MOF structures since the aromatic groups of the linkers display a rocking motion about its axis of connection.

2.2.3 Pore electrons

Crystallographic studies can provide useful information about pore contents in porous crystalline solids, mainly the location of adsorbents,[79-81] in addition to the crystal structure of the solid itself. MOF crystal structures typically contain large void volumes. Adsorbed species in these voids are not as strongly confined to specific sites as the strongly bonded atoms constituting the structure, and may thus appear as atoms with poorly defined position in structure refinement. This is because diffraction provides information about the average position of electrons in the unit cell, and the specific conformations of adsorbed species will vary throughout the sample.

The structure factors of many MOF crystal structures reported in the literature have been treated with the program SQUEEZE, used to “remove” the contribution of disordered solvent molecules (of a user defined volume of the unit cell) to the diffraction data.[82] This program also gives a rough estimate of the electron content of the disordered part of the unit cell, but relies on high completeness and accurately determined intensities for low angle reflections. When data sets are incomplete, or of poor quality, SQUEEZE becomes less useful, and estimates of electron number become less accurate. If the crystal structure is inaccurate when SQUEEZE is applied, the data is over-fitted and information is lost. The program was designed to mask volumes containing disordered solvent molecules in small-molecule structures, and should only be used when a restrained solvent model cannot be implemented.[82] The refinements reported in this work make use of dummy atoms to account for adsorbates.

2.2.4 Validation

There are several indicators used to assess the quality of SC-XRD data, and others to describe how well the refined crystal structure fits to the collected data. Unfortunately, it is not straightforward (nor is there any established convention in the crystallographic literature) to provide limits for which values are acceptable, as it depends on many factors such as crystal quality, signal-to-noise ratio and instrument calibration.

R_{int} (or R_{sym}) is a measure of the consistency of the integrated reflections by comparing the values of observed, equivalent structure factors (F_O). High R_{int} values may originate from Laue group misassignment (causing false equivalents), erroneous absorption correction, crystal mosaicity or inhomogeneity, twinning or errors related to the experimental setup.

$$R_{int} = \frac{\sum |F_o^2 - F_o^2(mean)|}{\sum F_o^2}$$

R_{sigma} is a measure of the signal to noise ratio. It is useful to compare R_{int} to R_{sigma} if the data seem poor. The ratio between them may reveal twinning or Laue group mis-assignment, if the data have a low signal to noise ratio, but high R_{int} (originating from false equivalents).

$$R_{sigma} = \frac{\sum \sigma(F_o^2)}{\sum F_o^2}$$

The confidence factors to consider for a final or published crystal structure, which are assessments of the discrepancy between the experimental observations and the ideal calculated values, are usually R_1 (for the observed reflections; $F_O^2 > 2\sigma(F_O^2)$), the weighted R-factor wR_2 for all data and the goodness of fit (S).

$$R_1 = \frac{\sum ||F_o| - |F_c||}{\sum |F_o|}$$

$$wR_2 = \sqrt{\frac{\sum w(F_o^2 - F_c^2)^2}{\sum w(F_o^2)^2}}$$

$$S = \sqrt{\frac{\sum w(F_o^2 - F_c^2)^2}{N_{ref.} - N_{par.}}}$$

where F_C denote the calculated structure factors based on the model, and w is a refined weighting coefficient (used to minimize the impact of statistical and systematic errors), and $N_{ref.}$ and $N_{par.}$ is the number of unique reflections and number of refined parameters, respectively. S is less dependent on noise, and more sensitive to data to parameter ratio. If good confidence factors could not be achieved in the reported structure refinements, the data were inspected with scrutiny to make sure there was no twinning or missed symmetry. High values of wR_2 and S may also be a result of the weighting scheme in SHELXL. Used as a rule of thumb in this work, a well-ordered crystal measured on a properly calibrated instrument should achieve R_{int}, R_{sigma} and $R_1 \leq 5$ %, $wR_2 \leq 15$ % and $1.0 \leq S \leq 1.2$).

2.3 X-ray absorption spectroscopy

2.3.1 Theoretical background

X-ray absorption spectroscopy (XAS) refers to the measurement of X-ray absorption across an energy range, chosen to cover an *absorption edge* of an element of interest.[83] It is used to probe the electronic (oxidation) state and local environment of the atoms of the same element in a sample. A common use of XAS is to probe the active center of a catalyst, where the electronic state and local coordination is the feature of interest, and not the long-range order. Thus, the sample under investigation may be solid or liquid, crystalline or amorphous.

The energy dependent absorption of X-rays through a sample of thickness *d* is described by the Beer-Lambert law: $I_1(E) = I_0(E)e^{-\mu(E)d}$ where μ(E) is the absorption coefficient and $I_0(E)$ and $I_1(E)$ are the intensities of the initial and transmitted beam (as a function of energy), respectively. We assume that energy can only be removed from the beam by absorption of quanta $\frac{hc}{\lambda}$ (where h is the Planck constant, c is the speed of light in vacuum and λ is the photon's wavelength) by atoms in the sample, which results in the ejection of a core electron into the continuum. The X-ray absorption cross-section of an element contains one or more sharp increases in the absorption coefficient, called absorption edges. They are observed whenever the photon energy reaches the well-defined energy levels of core electrons, and are named after the principal quantum number of the electron that is excited: K for n = 1, L for n = 2, M for n = 3, etc. As the orbital structure changes with increasing quantum number, the number of edges in close vicinity is 2n-1.[84]

The region of the XAS spectrum close to the edge is called X-ray absorption near edge structure (XANES), and contains information about the state of the element being probed, e.g. oxidation state. The extended X-ray absorption fine structure (EXAFS) region of a XAS spectrum starts at 20 -30 eV above the edge jump. At this energy, the excited electron will have a significant kinetic energy and a de Broglie wavelength comparable to interatomic distances. Simplified, the interaction between the excited photoelectron and the electrons of the neighboring atoms affects the absorption spectrum, which can be observed as an oscillation of the absorption coefficient as a function of energy. Through Fourier transformation, this oscillation (EXAFS signal) can be interpreted as a radial distribution of electron density from the probed atom. Since Fourier transformation is a complex function, both real and imaginary parts are obtained (which are used in structure refinement), but the chemical interpretation is more intuitive when considering the modulus.[85] EXAFS spectra of $CuCl_2 \cdot 2H_2O$ are shown in Figure 12 to illustrate the steps of EXAFS data acquisition and analysis. The absorption spectrum (Figure 12a) shows the edge jump at ~8997 eV and subsequent oscillations. The oscillating part of the raw spectrum is extracted by convolution and plotted as a function of the excited photoelectron's wave vector (Figure 12b). A Fourier transformation is performed to obtain information about the local surroundings (1 – 5 Å radial distance) of the probed element (Figure 12c).

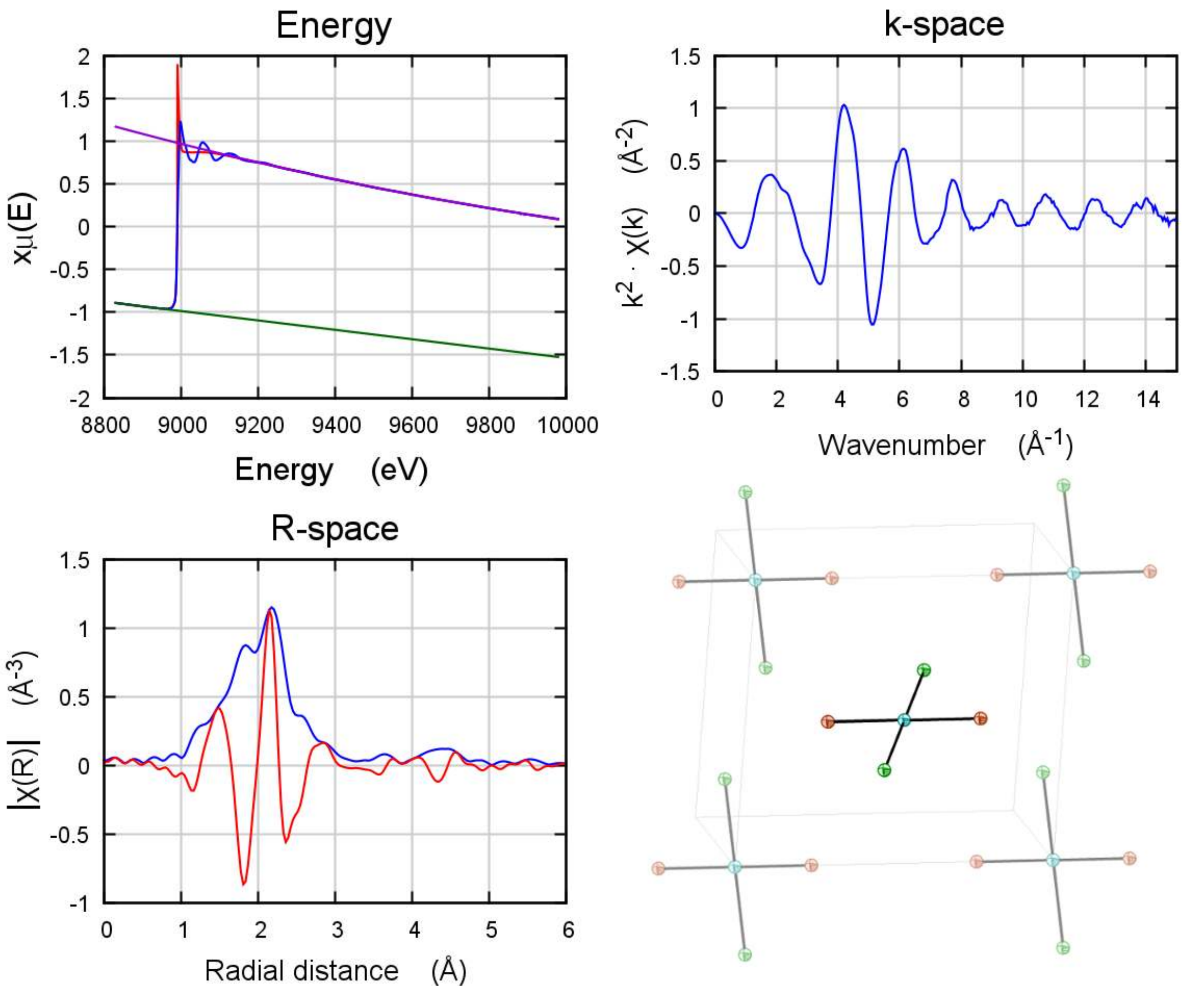

Figure 12. XAS spectrum of $CuCl_2$ x $2H_2O$. From top left: Absorption plot (blue) over the Cu K edge with baselines (green and purple) and background (red), k-plot (normalized, wheighted absorption coefficient as a function of the wave vector), R-plot (Fourier transformed, imaginary part (red) and modulus (blue), showing an approximate radial distribution function of electron density. The two overlapping peaks originate from the interactions of Cu with O and Cl, respectively). Bottom right: crystal structure of $CuCl_2 \cdot 2H_2O$, showing the local environment of Cu atoms in the compound.

EXAFS effectively complements diffraction techniques in the advanced characterization of porous solids. It can be used to probe the active site of a catalyst at reaction conditions, under which diffraction is rarely applicable.[86] It has also been used to provide detailed structural information on the inorganic units of MOFs, especially in cases where the SBU has a lower symmetry than that of the framework.[15,87]

2.3.2 Execution of XAS experiments

All XAS data acquisitions reported in this work were performed at the spectroscopy beamline I811 at the MAXLAB Max2 synchrotron in Lund, Sweden[88]. All samples were prepared as pellets (thickness optimized in order to obtain the best signal to noise ratio in transmission mode) using a pressure of up to 50 MPa. The samples were measured in transmission mode using a gas flow cell with temperature control.[89] To obtain parameters for the refinement of the MOF incorporated species, well-characterized analogous compounds (same coordination environment of the element of interest) were measured. The acquired spectra were analyzed with Athena.[90] All EXAFS spectra presented herein are phase uncorrected, and thus the distances in the radial plots are not directly comparable to the crystallographic bond lengths. Spectrometer operation at the synchrotron and the final EXAFS and XANES refinements were performed by Elisa Borfecchia, Luca Braglia, Giovanni Agostini, Kirill Lomachenko and Carlo Lamberti.

3 Results and discussion

As stated in the scope, this chapter is divided into three topics: (1) Synthesis optimization for large single crystals of UiO-66 and UiO-67, and their obtained crystal structures. (2) Adsorption and water stability studies on UiO-67 type MOFs. (3) Functionalization of UiO-67 by Pt and Cu species, their structure and reactivity.

3.1 Crystallization, structure and defects

This part covers the work published in **paper I:** "Detailed Structure Analysis of Atomic Positions and Defects in Zirconium Metal−Organic Frameworks",[91] and also features details of the preceding work and some additional elaboration on the synthesis conditions and crystallographic results that are not discussed in the article.

Crystal structures of UiO-66 and UiO-67 were well-known when this work was initiated. The structural details from previously published work are described in the introduction (section 1.1.1, page 3). A SC-XRD structure of UiO-67 had already been reported when **paper I** was published,[92] but this contained no additional information than was already available from previously reported structures determined by PXRD. The work presented in **paper I** is the first characterization of the different positions of the μ^3-O(H) groups in Zr-MOFs by diffraction, although these had previously been described using EXAFS with supporting DFT calculations.[22] More importantly, the article presents the first structural observation of missing linker defects.

3.1.1 Synthesis of UiO-66 and UiO-67 single crystals

SC-XRD has the ability to provide very detailed crystal structures, but requires a single crystal of a certain size (diffracting volume). This is usually around 50 μm for laboratory diffractometers, although size is only one of several factors (such as crystalline order or diffracting strength due to presence of heavy atoms). Until the introduction of modulators, obtaining Zr-MOF crystals of such size was not feasible. At dedicated diffraction beam lines at synchrotrons, the X-ray beam is so focused and intense that the crystal size limitation is more often what the researcher can practically handle rather than the diffracting volume of the crystal. Given that the maximum obtainable crystal size of UiO-66 was around 300 nm when this work was initiated,[69] larger crystals had to be obtained before SC-XRD experiments could be performed.

In the process of improving the crystal size of UiO-66, the following results were obtained from parallel one-parameter studies:

- Open flasks invariably produced larger crystals than closed Teflon liners in autoclaves, over a large range of temperatures (80 °C to 140 °C), regardless of modulator type or concentration.
- Using benzoic acid as modulator was found to consistently yield larger crystals than equivalent reactions with acetic acid as a modulator. This was found to be the case, at all concentrations up to 30 equivalents with respect to $ZrCl_4$. Higher concentrations were not investigated systematically, although several attempts at 50 – 80 equivalents (with respect to $ZrCl_4$) failed to produce a MOF at all.
- Addition of methanol, HCl or LiCl were not found to have any clear effect on the crystal size.
- In open flasks syntheses with 30 equivalents of benzoic acid with respect to $ZrCl_4$, a crystallization temperature range of 110 - 130 °C was found to consistently produce larger crystals than higher and lower temperatures. There was no significant difference within this range.

UiO-66 single crystals of 15 µm were obtained from synthesis in open flasks, utilizing 30 equivalents of benzoic acid (with respect to $ZrCl_4$) as modulator, crystallization temperature of 110 °C and a $ZrCl_4$:linker:DMF molar ratio of 1:1:100. A detailed synthesis description of the sample used for SC-XRD measurements can be found in the supporting information of **paper I**.

UiO-67 has been, by far, the most investigated MOF in this work, with over 300 syntheses performed in the pursuit of optimized single crystal synthesis conditions. In parallel, one-variable experiments, the following results were obtained:

- Consistently large crystals were obtained when 30-40 molar equivalents of benzoic acid (with respect to $ZrCl_4$) were used as a modulator. Additions of benzoic acid above this concentration resulted in precipitation of linker.

- Single crystals in the range of 50 – 70 µm could also be obtained by using 4-nitrobenzoic acid or phenylacetic acid as a modulator. These modulators were not used extensively due to high cost and no advantage over benzoic acid.

- Large crystals were most easily obtained when the concentration of reagents in DMF was high - close to the solubility limit of the H_2bpdc linker, which was found to be soluble in a 1:300 molar ratio with DMF at elevated temperatures (ca. 120 – 130 °C, which was applied to the synthesis solution before commencing the reaction period), but this is very temperature dependent.

- Addition of methanol, HCl or LiCl were not found to have any clear effect on the crystal size.

- Open flasks invariably produced larger crystals than closed Teflon liners in autoclaves, over a large range of temperatures (80 °C to 140 °C), regardless of modulator type or concentration.

- In open vessel synthesis, the initial results of temperature were inconsistent. It was believed for a time that lower synthesis temperatures produced larger crystals. Upon inspection of all results, synthesis temperature (in the range of 80 °C to 140 °C) does not appear to have any effect on crystal size.

- In a series of parallel syntheses where reaction solutions had been divided between 3 glass flasks (new, treated with 2M $HCl_{(aq)}$ or 2M $NaOH_{(aq)}$) and one Teflon lined autoclave, the largest, least intergrown crystals were formed in the base treated flasks. However, the experiments were not repeated enough times to establish a causal relationship.

The largest single crystals of UiO-67 (70 µm, see) were obtained by performing the synthesis in open flasks, utilizing 30 equivalents of benzoic acid (with respect to $ZrCl_4$) as modulator, and a $ZrCl_4$:linker:DMF molar ratio of 1:1:300. Photographs of a single crystal and a film of intergrown crystals are shown in Figure 13.

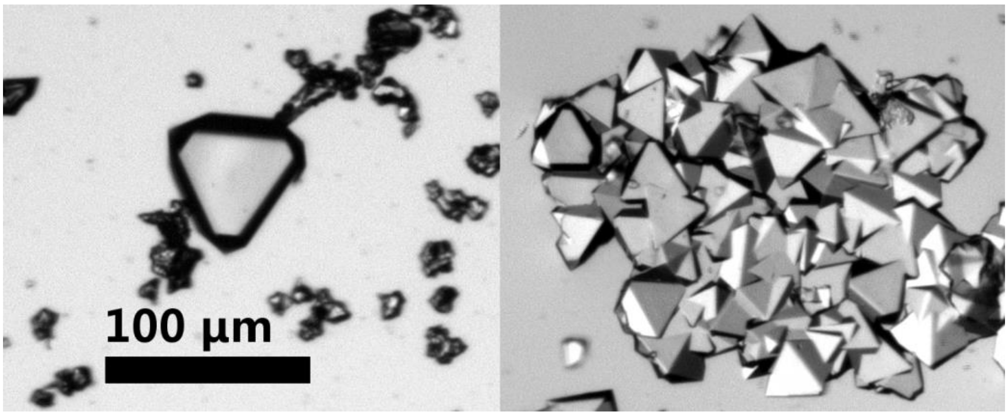

Figure 13. Photographs of typical single crystals (left) and intergrown crystal films (right) of UiO-67, both formed on the walls of reaction vessels.

In conclusion, similar strategies were found to yield single crystals of UiO-66 and UiO-67. In both MOFs, working close to the solubility limit of the linker, at crystallization temperatures around 110 - 120 °C, using 30 equivalents of benzoic acid (with respect to Zr) as modulator was successful. The only major difference was the concentration of reagents in DMF. Crystallization in sealed Teflon lined autoclaves consistently resulted in smaller crystals. This may be due to byproducts of the synthesis and DMF decomposition accumulating in the vessel. These volatile chemicals e.g. HCl, formic acid and dimethylamine are normally allowed to evaporate in open flasks. It is likely that their presences affect the reaction equilibria in the synthesis and disfavor large crystals. In addition, the Teflon surface in the liners used in these experiments is very coarse, possibly favoring nucleation.

The technical execution of the synthesis was also found to be an important factor. To minimize crystal nucleation, great care was taken to make sure a clear solution was obtained between each addition. The linkers were added after the modulator to avoid the formation of MOF before the addition of modulator, and after the solution had been heated to close to the reaction temperature (~ 120 – 130 °C) to facilitate dissolution. A crystalline film would often cover the entire glass synthesis vessel's interior after synthesis. By soaking the glassware in strong (2M) $NaOH_{(aq)}$ solution, it was possible to largely inhibit nucleation on the glass surfaces and obtain large single crystals from the inclining walls.

Recently, a new synthesis procedure for single crystals of UiO-66 was published by Trickett et al.[70] By crystallizing the MOFs in a 50/50 volumetric mixture of diethylformamide (DEF) and formic acid, and very low concentration of reagents, single crystals up to 300 μm could be obtained. Clearly, this solution disfavors nucleation even more than those used in this work, presumably due to the increased "competition" for Zr sites that the linkers can bind to (in the reported synthesis the molar ratio between the linker and formic acid is around 1:1600). This will disfavor both MOF nucleation and crystal growth. At the same time, the linker is poorly soluble in this mixture, as it is insoluble in formic acid. This could provide an energetic barrier for the dissociation of a linker molecule from a growing crystal. In that sense, the conclusion presented earlier that larger crystals were obtained when working close to the solubility limit of the linker, is also valid for this method.

We reproduced the method reported by Trickett with slight modifications (using DMF instead of DEF, and a higher concentration of $ZrCl_4$ and linker) and can confirm that the resulting crystals were larger than those obtained by benzoic acid modulation. However, the sample was found to be unstable to water, a rare occurrence for the usually highly stable UiO-66. This is likely due to the formation of a highly defective material, in accordance with recent reports on UiO-66 samples obtained from synthesis solutions containing excessive amounts of formic acid.[37,93]

3.1.2 Crystal structures of UiO-66 and UiO-67

The crystal structures of UiO-66 and UiO-67 reported herein have been determined using synchrotron SC-XRD. The high quality of the diffraction data allowed for a stepwise improvement of the crystal structures during refinement.

The crystal structure of UiO-66 was first solved to closely fit the originally reported structure, with an occupancy of 1 for all atoms. This initial structure refinement gave poor confidence factors, despite excellent data quality (Table 1). To improve the fit, the μ^3-O atom, which initially appeared as an elongated ellipsoid along the 1 1 1 axis, was split into two positions with a site occupancy of 0.5 each and a distance 0.6 Å apart (Figure 14). This configuration is in accordance with previous EXAFS measurements and DFT calculations, which suggested that the μ^3-O and μ^3-OH groups occupy different positions, with the μ^3-OH group being further away from the centroid of the cluster. In previously reported single crystal structures of Zr-MOFs, these had not been resolved.[69,92,94]

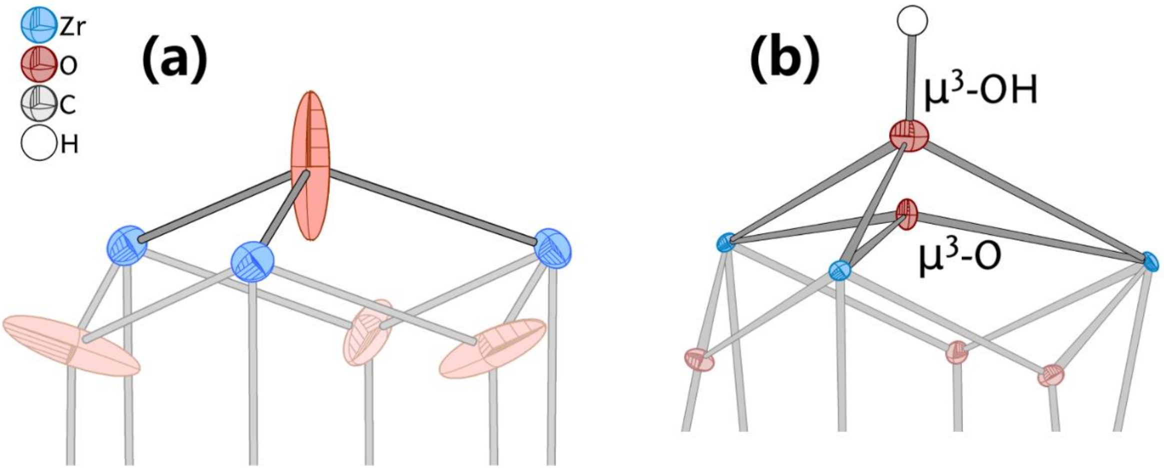

Figure 14. Representations of the shape and position of the the μ^3-O and μ^3-OH as they appeared in (a) the first Zr-MOF single crystal structures and (b) in this work.

The thermal ellipsoids of the linker C atoms were relatively large, and allowing the occupancy to refine (all constrained to the same occupancy coefficient: Z_{Linker}) improved the refinement and reduced the ellipsoid volumes to more reasonable levels, implying missing linker defects in the MOF crystal. Moreover, the carboxylate C – O bonds appeared longer than expected for this type of bond, at 1.31 Å instead of the expected 1.255 Å (the average C⎓O crystallographic bond length)[95] for aryl carboxylates. The model was then revised with two separate oxygen atoms to address this issue (shown in Figure 15); one at the expected position of a carboxylate O atom (called $O_{carboxylate}$) and one at the center of observed excess electron density right next to it (called O_{defect}). The occupancy factor of $O_{carboxylate}$ was constrained to that of the linker (Z_{Linker}), and the occupancy of O_{defect} to 1-$Z_{Linker.}$ These changes improved the refinement, and the carboxylate C ⎓O bond length refined to 1.261 Å, which is closer to its expected length. One should note that the Zr - $O_{carboxylate}$ and Zr - O_{defect} bond lengths are very similar (within each other's margin of error), which explains why the defect oxygen atoms have not been observed by EXAFS measurements. The bond lengths are presented in Table 1.

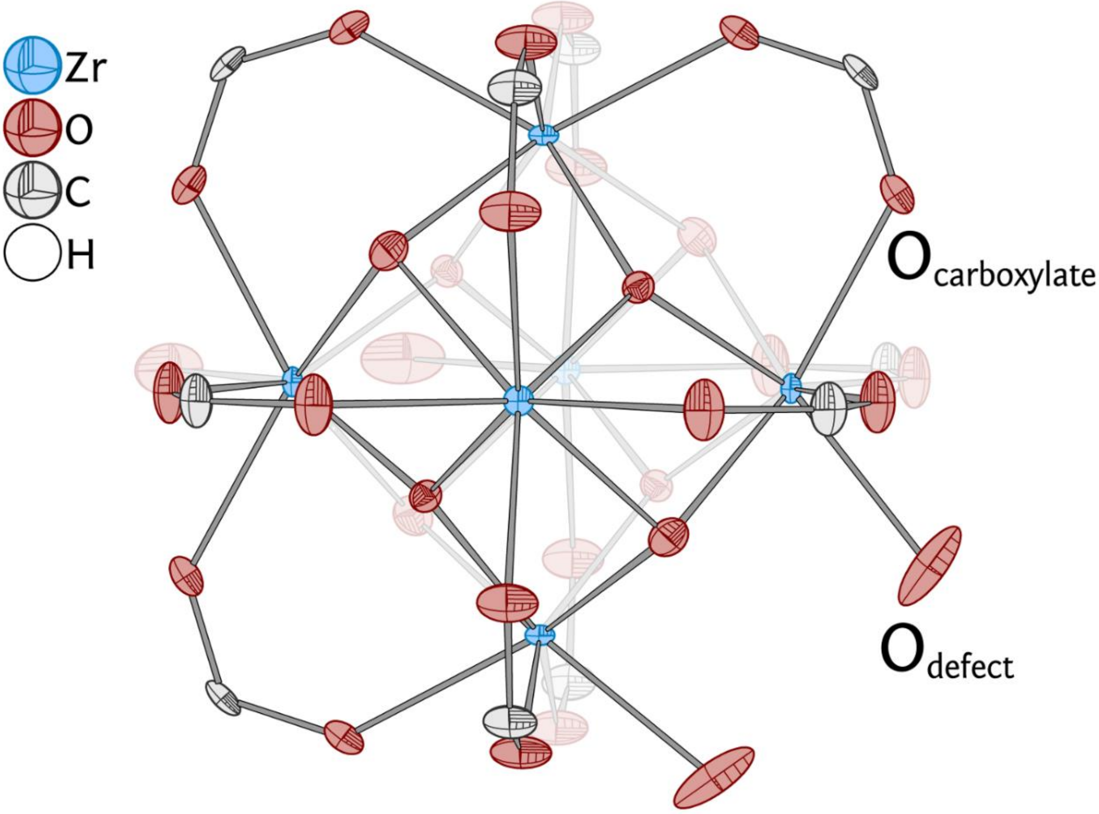

Figure 15. Cluster of UiO-66 showing both conformations of the cluster terminating O atoms (OH^-/H_2O capped missing linker defect assigned at a random site).

It was not possible to improve the model further with the range of molecules that may occupy the defect sites, and thus they were assumed to be a mixture of hydroxide, water and DMF. OH^- and H_2O seems to be the most likely candidates, as OH-groups are observed in FT-IR spectra of UiO-66 even at very high temperatures,[22] and is also supported by recent reports.[34,96] It is worth noting that the missing linker defects seem to be capped by OH^-/H_2O pairs rather than benzoate (or formate, which is created by decomposition of DMF during synthesis), even though the modulator outnumbered the linkers by 30 to 1 in the synthesis mixture. A benzoate capped defect would likely cause an OH^-/H_2O defect on the opposing cluster, so a firm conclusion cannot be made from diffraction alone. Benzoate may also have been removed during washing of the crystals.

Some additional explanation can be found by inspection of Zr_6 clusters in molecular (non-MOF) crystal structures. There are at least 13 Zr_6 clusters which are capped only by carboxylates (in addition to OH^-/H_2O) reported in the Cambridge structural database (CSD)[97], and all but two also contain one or more “open” defects.[20,98-105] However, the two structures in question are of so poor quality that they can hardly be considered. In 10 of the remaining 11 structures the μ³-O and μ³-OH positions are resolved and ordered in a tetrahedral conformation. In certain cases, the clusters are not capped by a H_2O/OH^- pair, but by carboxylates coordinated to only the Zr ion in a mono- or bidentate fashion (as shown in Figure 16b, from Kickelbick et al.[20]). This motif may also be present as a defect in Zr-MOFs, but has not been observed (to the best of the author's knowledge).

It could be hypothesized that a Zr cluster with 12 bridging carboxylate ligands is disfavored due to structural strain by the fact that it rarely occurs in reported structures. Open defects could relieve some of this strain, thus leaving a more relaxed energetically favored cluster. This claim is strengthened by the fact that a large excess of linker is needed to perform a synthesis of "defect-free" UiO-66.[35]

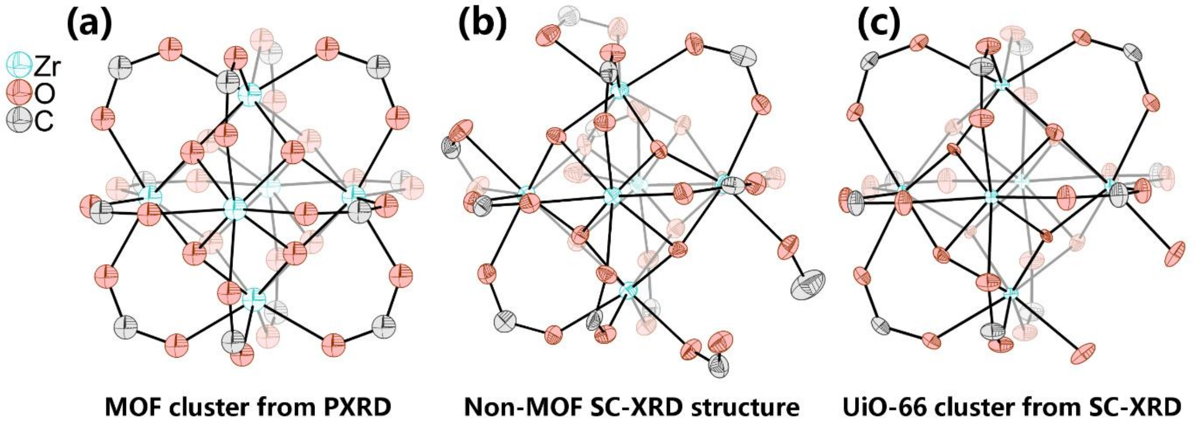

Figure 16. Structures of Zr-clusters as determined by (a) PXRD on UiO-66[15], by (b) SC-XRD of molecular crystals[20] and (c) by SC-XRD on UiO-66 (defect assigned to a random site).

The structure of UiO-67 was well known when this work was started, but the SC-XRD results reported herein are of extraordinary high quality and provided some insights in the orientation of the linker. In contrast to UiO-66, the phenyl groups of the linker in UiO-67 seem to be slightly tilted from its own plane of connectivity, by approximately 16° at the measurement temperature (100 K). The measured samples of UiO-67 contained a non-quantifiable concentration of missing linker defects, indicated by the presence of electron density peaks at the expected position of defect oxygen (shown in Figure 17). However, these peaks are very weak, comparable with the excess electron density originating from delocalized charge in C – C bonds.

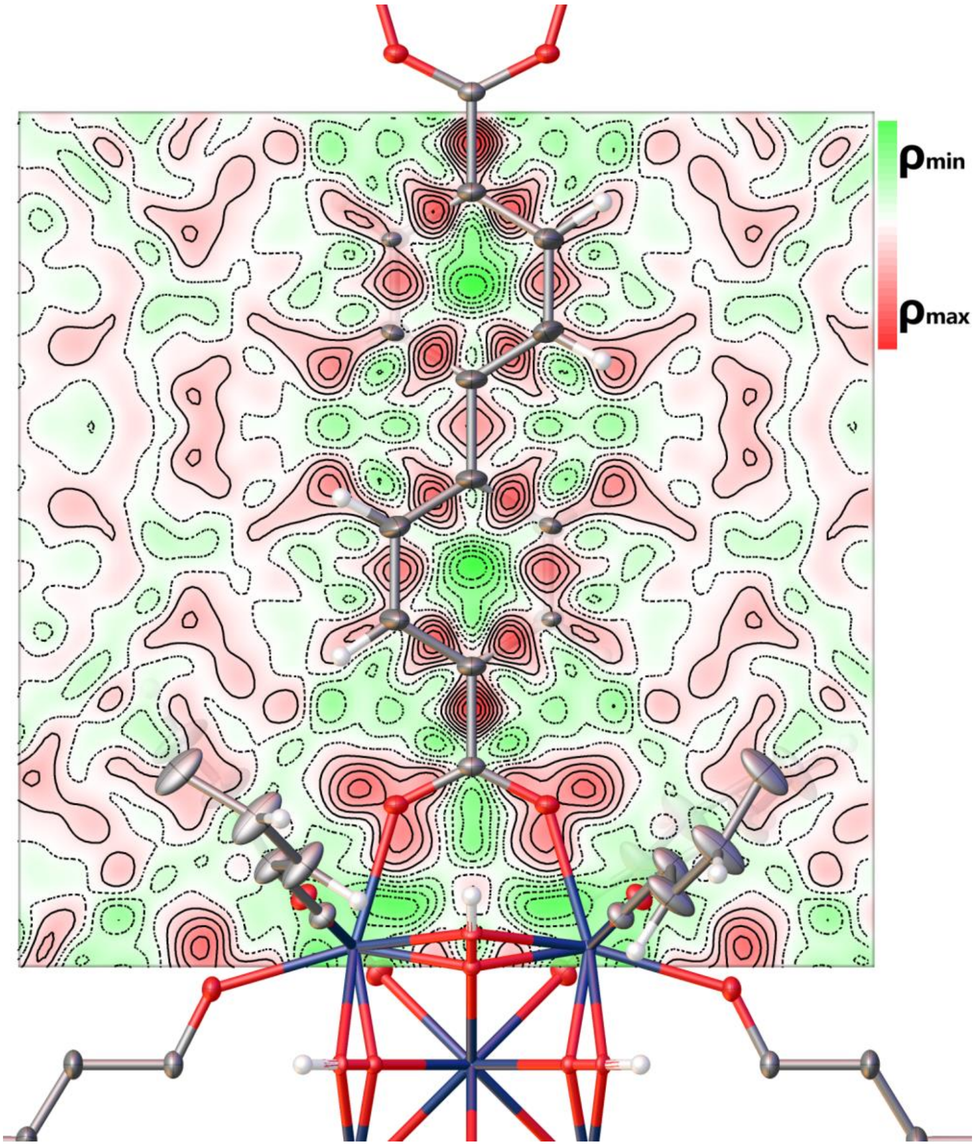

Figure 17. 2D Fourier difference map of the final structure of UiO-67, parallel to Miller plane 1 0 0. The plane shown is intersecting the centroid of the Zr6 cluster, the carboxylate oxygen atoms and the axis of connection of the linker. Excess electron density is shown as red regions, whereas electron deficiency is shown as greeen. The scale of the map is ±1.5 e^- $Å^{-3}$ (which in this refinement equals less than 0.1 C atom for the strongest peaks).

Apart from the different amounts of defects, the clusters of UiO-66 and UiO-67 are identical, as expected. From the diffraction data, no long-range order regarding the orientation of cluster μ^3-O/OH arrangement or defects can be observed, implying a random distribution. Table 1 shows a summary of the data collection and structure refinement details for UiO-66 and UiO-67, both before and after inclusion of structural details.

Table 1. Data collection and structure refinement details for UiO-66 and UiO-67. Two refinements were performed, one with a defect-free ideal model without distinguishing μ^3-O and OH (left column). For UiO-66, the structure was improved by inclusion of defects, partial occupancy of linkers, and separation of μ^3-O and OH. For UiO-67, the structure was improved by inclusion of tilted linkers and separation of μ^3-O and OH.

	Original UiO-66	**UiO-66 with defects**	**Original UiO-67**	**UiO-67 with details**
Crystal data				
Chemical formula	$C_{48}H_{24}O_{32}Zr_6 \cdot 8(C)$	$C_{37.9}H_{18.0}O_{32}Zr_6 \cdot 8(C)$	$C_{84}O_{32}Zr_6 \cdot 8(C_{0.15})$	$C_{84}O_{32}Zr_6 \cdot 8(C_{0.15})$
Linker occupancy	1.0	0.79	1.0	1.0
M_r	1758.08	1631.6	2134.98	2134.98
Crystal system, space group	Cubic, $Fm\bar{3}m$	Cubic, $Fm\bar{3}m$	Cubic, $Fm\bar{3}m$	Cubic, $Fm\bar{3}m$
Temperature (K)	100	100	100	100
a (Å)	20.7461 (3)	20.7461 (3)	26.8778 (8)	26.8778 (8)
V (Å^3)	8929.1 (4)	8929.1 (4)	19417.0 (17)	19417.0 (17)
Z	4	4	4	4
Radiation type	synchrotron, λ = 0.76000 Å	synchrotron, λ = 0.76000 Å	synchrotron, λ = 0.76000 Å	synchrotron, λ = 0.76000 Å
μ (mm^{-1})	0.89	0.89	0.42	0.42
Crystal size (mm)	0.01 × 0.01 × 0.01	0.01 × 0.01 × 0.01	0.06 × 0.06 × 0.04	0.06 × 0.06 × 0.04
Data collection				
Diffractometer	Bruker MD2 microdiffractometer		Bruker MD2 microdiffractometer	
Absorption correction	multi-scan	multi-scan	multi-scan	multi-scan
No. of measured, independent and observed [$I > 2\sigma(I)$] reflections	17300, 632, 613	17300, 632, 613	21309, 1305, 1242	21309, 1305, 1242
R_{int}	0.028	0.028	0.027	0.027
$(\sin \theta/\lambda)_{\max}$ (Å^{-1})	0.675	0.675	0.675	0.675
Refinement				
$R[F^2 > 2\sigma(F^2)]$, $wR(F^2)$, S	0.038, 0.104, 1.18	0.024, 0.074, 1.25	0.030, 0.071, 1.05	0.015, 0.039, 1.13
No. of reflections	632	632	1305	1305
No. of parameters	39	46	46	59
No. of restraints	0	0	0	1
H-atom treatment	H-atom parameters constrained	H-atom parameters constrained	All H-atom parameters refined	μ^3-O - H bond length restrained, all other parameters refined
$\Delta\rho_{\max}$, $\Delta\rho_{\min}$ (e Å^{-3})	0.97, −0.79	0.50, −0.32	1.00, −0.89	0.35, −0.24
Bond lengths (Å)				
O⎓C carboxylate	1.312(5)	1.261(5)	1.2682(17)	1.2682(9)
Zr - $O_{\text{carboxylate}}$	2.215(3)	2.220(5)	2.2186(12)	2.2181(7)
Zr - O_{defect}	-	2.223(19)	-	-
Zr - μ^3-O	2.144(3)	2.0694(14)	2.1389(16)	2.0589(5)
Zr - μ^3-OH	-	2.270(5)	-	2.2507(14)
Zr - Zr	3.5146(8)	3.5146(8)	3.5120(4)	3.5120(4)

3.1.3 Beyond paper I: Adsorption sites

As previously mentioned (section 2.2.3), diffraction experiments can be used to provide information about adsorption sites in MOFs in a qualitative manner by modelling the electron density of the pores (which originate from disordered guest molecules) with dummy atoms.[80] This way to treat the void regions of MOF crystal structures during structure refinement is an alternative to computational solvent masking. In this example, SC-XRD patterns were acquired from UiO-67 single crystals which had been stored in 2-propanol and water, respectively. Full experimental procedures and refinement data are found in appendix A2, Table 5 on page 95. The data obtained from the crystal filled with 2-propanol were used to refine the structure of solvent-filled UiO-67. The pore contents are modelled using atoms with freely refined position, size and occupancy coefficient. The resulting model is shown in Figure 18. It is not meant as a quantitative assessment of solvent content, but a qualitative description of the location of the strongest adsorption sites. They agree with previously reported calculations.[29] Although solvent masking programs such as SQUEEZE[82] or Olex2/mask[106] can be used to omit void regions from the structure refinement, the information about pore content is lost and no additional information is gained.

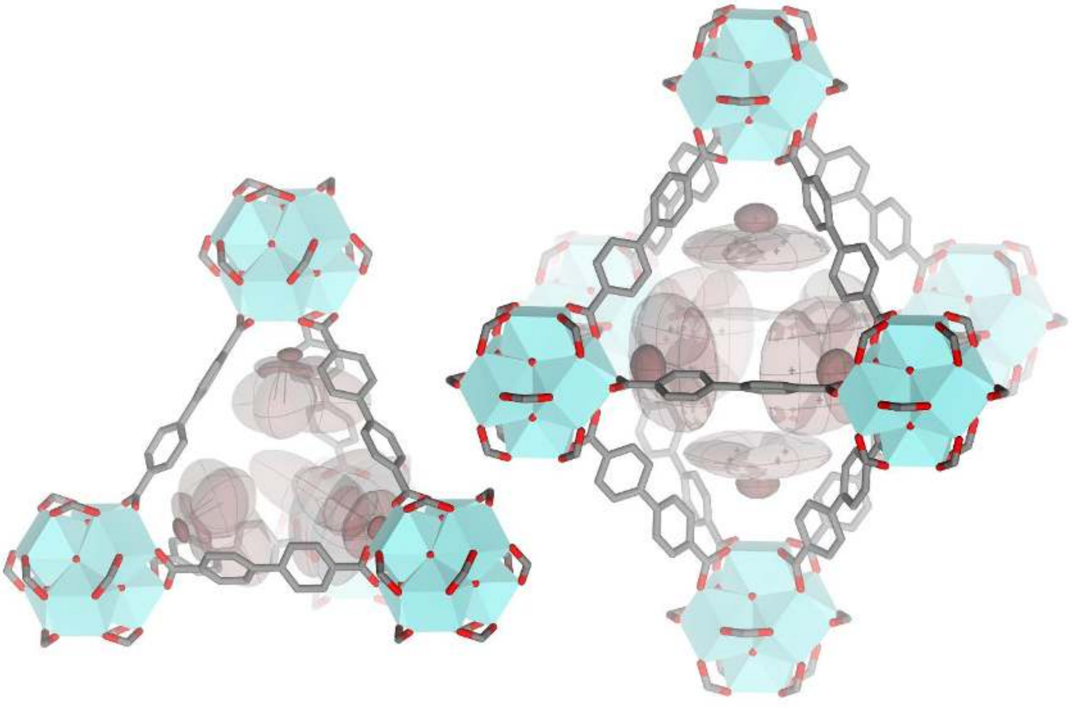

Figure 18. The location of strong adsorption sites in the tetrahedral cage (left) and octahedral cage (right) in UiO-67, shown as transparent dark red ellipsoids. The strength of the site corresponds to the density of the ellipsoid, the strongest site is well-defined in the corner of the tetrahedral cage, 2.72(5) Å from the O of μ^3-OH.

3.1.4 Summary

The crystal structures of Zr-MOFs UiO-66 and UiO-67 were determined by SC-XRD to an unprecedented degree of accuracy, and the work represents a significant step forward in terms of structural detail in Zr MOF crystal structures. The μ_3-O atom of the prismatic faces of the Zr_6 octahedron was split into two distinct μ_3-O and μ_3-OH, with occupancy of 0.5 each, and having Zr−O and Zr−OH distances in agreement with those obtained from EXAFS data and periodic DFT studies. The understanding of missing linker defects, a fundamental and important feature of Zr-MOFs, has also been improved. This level of detail, which previously required highly specialized multi-technique approaches to determine, can now be achieved in a short routine measurement.

The improved synthesis methods for Zr-MOF single crystals are likely to be general, and may thus be a valuable tool for determination of new Zr-MOF structures. The results concerning defects and the structure of the cluster have implications for Zr-MOFs based on such clusters, and may contribute to the general understanding of these materials.

3.2 Properties of UiO-67 type MOFs

This chapter covers the results obtained from investigations on Zr-MOFs with different organic linkers, most of which are published in **papers II** and **III**, which concerns linker syntheses and adsorption properties, respectively. The functionalization of UiO-67 with metal complexes is discussed separately from this, in chapter 3.3 on page 55.

In addition to the published results, this chapter contains details of additional, unpublished work preceding **paper III**. Specifically, the structure and stability of nitro functionalized UiO-67 is discussed to provide a frame of reference to the published MOFs.

As stated in the scope, one of the primary aims of this work has been to develop Zr-MOFs with a range of different linkers and to evaluate their properties. To achieve a large chemical diversity, several new linkers have been synthesized (see Figure 19), and further used in the synthesis of Zr-MOFs. The linkers described herein were chosen due to their expected affinity to CO_2 (in the case of H_2bpdc-$(NH_2)_2$ and H_2bpdc-$(NO_2)_2$, Figure 19d-e) or methane (for H_2bpdc-Me_2 and H_2bndc, Figure 19b-c), or because of their assumed ability to increase the porosity of the resulting MOFs (for H_2tpdc-Me_2 and H_2qpdc-Me_2 shown in Figure 19f-g). Syntheses and crystallographic characterization of most of the linkers discussed herein is also thoroughly described in **Paper II**: "Efficient, Scalable Syntheses of Linker Molecules for Metal-Organic Frameworks".[107] Linker synthesis was performed by Knut T. Hylland and Lianpao Wu.

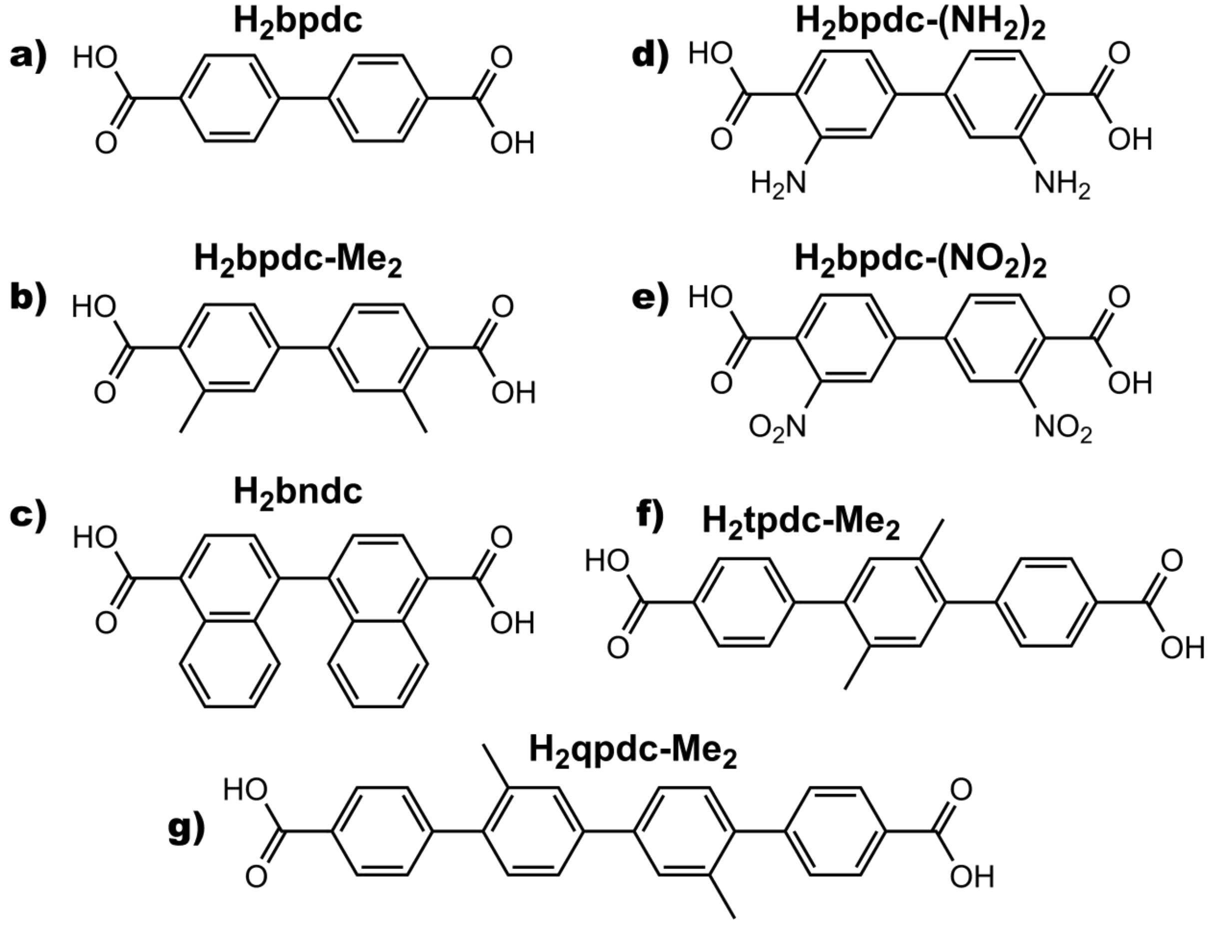

Figure 19. Linkers used in this work: **a)** biphenyl-4,4′-dicarboxylic acid (H$_2$bpdc), **b)** 3,3′-dimethylbiphenyl-4,4′-dicarboxylic acid (H$_2$bpdc-Me$_2$), **c)** 1,1′-binaphthyl-4,4′-dicarboxylic acid (H$_2$bndc), **d)** 3,3′-diaminobiphenyl-4,4′-dicarboxylic acid (H$_2$bpdc-(NH$_2$)$_2$), **e)** 3,3′-dinitrobiphenyl-4,4′-dicarboxylic acid (H$_2$bpdc-(NO$_2$)$_2$), **f)** 2′,5′-dimethyl-[1,1′:4′,1″-terphenyl]-4,4″-dicarboxylic acid (H$_2$tpdc-Me$_2$) and **g)** 2′,3″-dimethyl-[1,1′:4′,1″:4″,1‴-quaterphenyl]-4,4‴-dicarboxylic acid (H$_2$qpdc-Me$_2$).

Zr-MOFs were successfully synthesized with all of the linkers shown in Figure 19, using solvothermal synthesis from solutions of ZrCl$_4$, linker and benzoic acid. During the work, it became apparent that the newly synthesized MOFs intended for methane adsorption experiments (made from the linkers H$_2$bpdc-Me$_2$ and H$_2$bndc) were much more stable toward water than the other UiO-67 analogues. They are both isostructural to UiO-67, with nearly identical lattice parameters and PXRD patterns (Figure 20). Further investigations showed that UiO-67-binaphthyl (made with the linker H$_2$bndc) was also stable during repeated water adsorption/desorption cycles (Figure 26). There have been several accounts on the water stability of regular UiO-67, whose structure collapses when an aqueous suspension of the MOF is dried directly, leaving a dense amorphous phase.[108] Although adding hydrophobic groups to the linker has been demonstrated to increase the stability of UiO-66,[109,110] this had not yet been investigated for UiO-67.

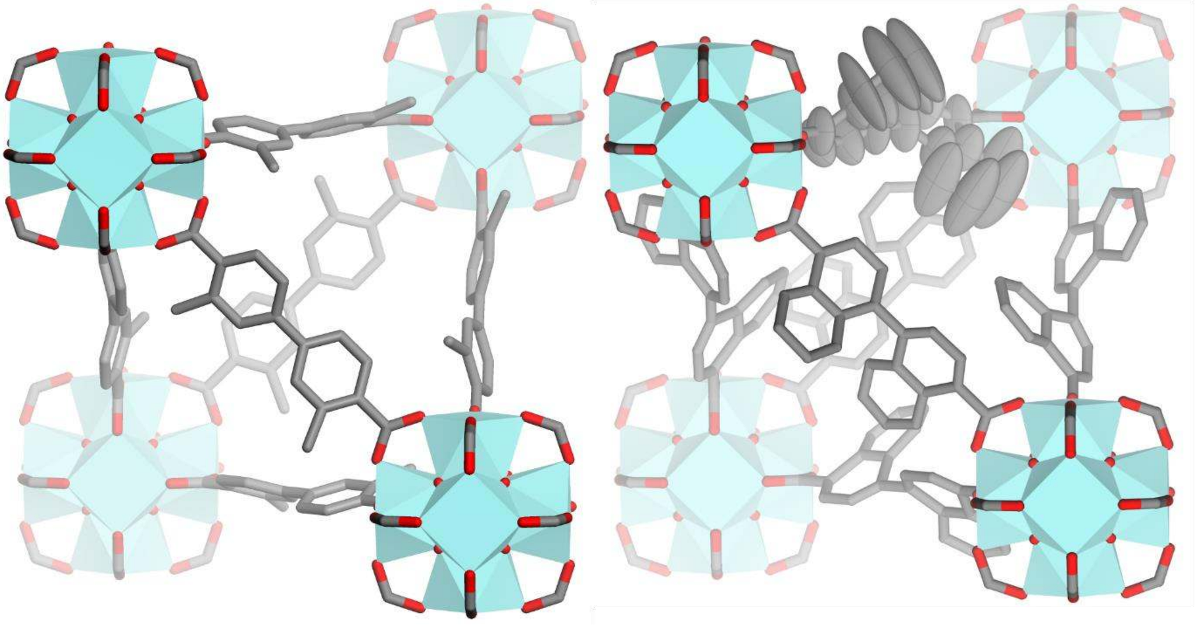

Figure 20. The crystal structures of UiO-67-dimethyl (left) and UiO-67-binaphthyl (right). Only the clusters and linkers surrounding one tetrahedral cage is shown. The confiomation of the linkers are chosen at random, as each C atom not on the (x,x,0) axis has 2 or 4 (in the case of methyl C) symmetrically equivalent positions. Vibrational ellipsoids are shown for one linker of UiO-67-binaphthyl at 50 % probability.

In **Paper III**: "UiO-67-type Metal−Organic Frameworks with Enhanced Water Stability and Methane Adsorption Capacity",[111] UiO-67-dimethyl and UiO-67-binaphthyl were thoroughly investigated for their N_2, CO_2, CH_4 and water adsorption properties, and their structures were examined in order to propose reasons for the increased stability. The main findings are described in the following chapters, along with some preliminary, as yet unpublished results from the continuation of this work.

3.2.1 Synthesis of dimethyl and binaphthyl UiO-67

Powder samples of UiO-67-dimethyl and UiO-67-binaphthyl were obtained using moderate amounts of benzoic acid (10 equivalents with respect to $ZrCl_4$) as modulator. Single crystals of UiO-67-dimethyl were synthesized using a high concentration synthesis solution (1:150 molar ratio of linker to DMF as opposed to 1:300 for regular UiO-67), as the linker is considerably more soluble in DMF than H_2bpdc. Using 30 equivalents of benzoic acid as modulator, single crystals of 100 µm and larger were easily obtained. Detailed synthesis descriptions are found in the supporting information for **paper III**.

Synthesis of large single crystals of UiO-67-binaphthyl was unsuccessful when using benzoic acid as modulator in concentrations of 5 – 36 molar equivalents with respect to $ZrCl_4$, reaching only a crystal size of only *ca.* 5 µm. Other modulators were therefore investigated, and 4-nitrobenzoic acid (NBA) was found to be ideal for single crystal synthesis – syntheses with 30 equivalents of NBA (in respect to $ZrCl_4$) afforded single crystals of 40 µm.

It is interesting to speculate on the reasons why NBA is a more effective modulator than benzoic acid when it comes to producing large crystals of UiO-67-binapthyl. From the success of the single crystal synthesis it is evident that NBA inhibits crystal nucleation under the reaction conditions to a larger degree than benzoic acid. One possible reason for this could be acidity effects – the aqueous pK_a values of NBA and benzoic acid are significantly different, with respective values of 3.44 and 4.20. Interestingly, the crystal size of MOFs seems to increase when the aqueous pK_a value of the modulator is close to that of the linker.[93] That said, it is important to note that the aqueous pK_a value and the "true acidity" of the modulator under MOF synthesis conditions (hot DMF solutions containing HCl) are not necessarily in perfect correlation. However, the pK_a value of a compound is closely connected to the stability of the deprotonated anion, and may thus provide some understanding as to why some modulators are more effective. Figure 21 shows pK_a values of several carboxylic acids, either used as modulators, or resembling the linkers used in this work.

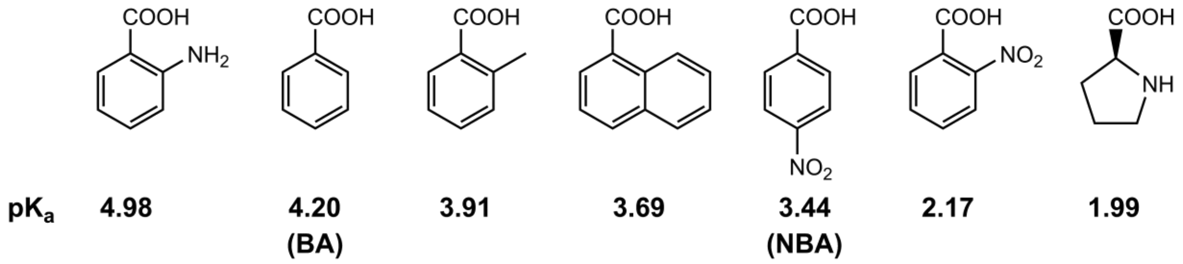

Figure 21. Molecular structures and pK_a values of the monocarboxylic acids discussed in this chapter. From left to right: 2-aminobenzoic acid, benzoic acid, 2-methylbenzoic acid, 1-naphthoic acid, 4-nitrobenzoic acid, 2nitrobenzoic acid and L-proline.

Although the 1st deprotonation pK_a values of the linkers will be lower than those of their monocarboxylic acid counterparts shown in the figure, they can be expected to follow the same trend. Thus, 4-nitrobenzoic acid, a more acidic modulator than benzoic acid, is more successful in assisting the growth of single crystals for naphthyl-functionalized linkers, which are more acidic than phenyl based linkers, e.g. H_2bpdc. Very recently, single crystal syntheses of several Zr-MOFs have been reported using L-proline (with pK_a 1.99) as modulator, indicating that the modulator can be considerably more acidic than the linker.

Synthesis of UiO-67 with H_2bpdc-$(NH_2)_2$, a less acidic linker, normally yield microcrystalline powder. Indeed, when attempting synthesis with that linker and NBA as modulator, no solid product is obtained at all. The more acidic linker may therefore be inhibiting the formation of a Zr-MOF with a “basic” linker. Although these observations form a pattern, further systematic experiments should be attempted before drawing definitive conclusions. Crystal growth of MOFs is a complex issue, likely depending on many factors including the steric properties and solubility of the modulator and linker, as well as their interaction with zirconium in the solution.

3.2.2 Structure of dimethyl and binaphthyl UiO-67

The crystal structures of UiO-67-dimethyl and UiO-67-binaphthyl both closely resemble that of regular UiO-67. The three MOFs form the same network topology and crystallize in the same space groups. However, the functional groups increase the linker volume, and the relative pore volume of UiO-67-binaphthyl is greatly reduced in respect to the other two MOFs.

The crystal structures provide insight into how the strong adsorption sites in proximity to the Zr clusters are influenced by the different linkers (schematically presented in Figure 22). In UiO-67-dimethyl, the methyl groups occupy the corners of the large octahedral cage. Its orientation deviates from the plane spanned by the carboxylate groups (Miller plane (100)) by an angle of 20.1°, thus barely affecting the corner of the tetrahedral cage where the strongest adsorption site is situated (Figure 22a). For UiO-67-binaphthyl, the effect is more pronounced: the naphthyl groups deviate by 41.1° from the (100) plane, which sterically affects the the adsorption site in the tetrahedral cage (situated above the μ^3-O(H) group, shown in Figure 22b). Indeed, the atom used to model the adsorbates in UiO-67-binaphthyl is situated 2.94(5) Å from the O of μ^3-OH, whereas the corresponding distance is only 2.72(5) Å in UiO-67.

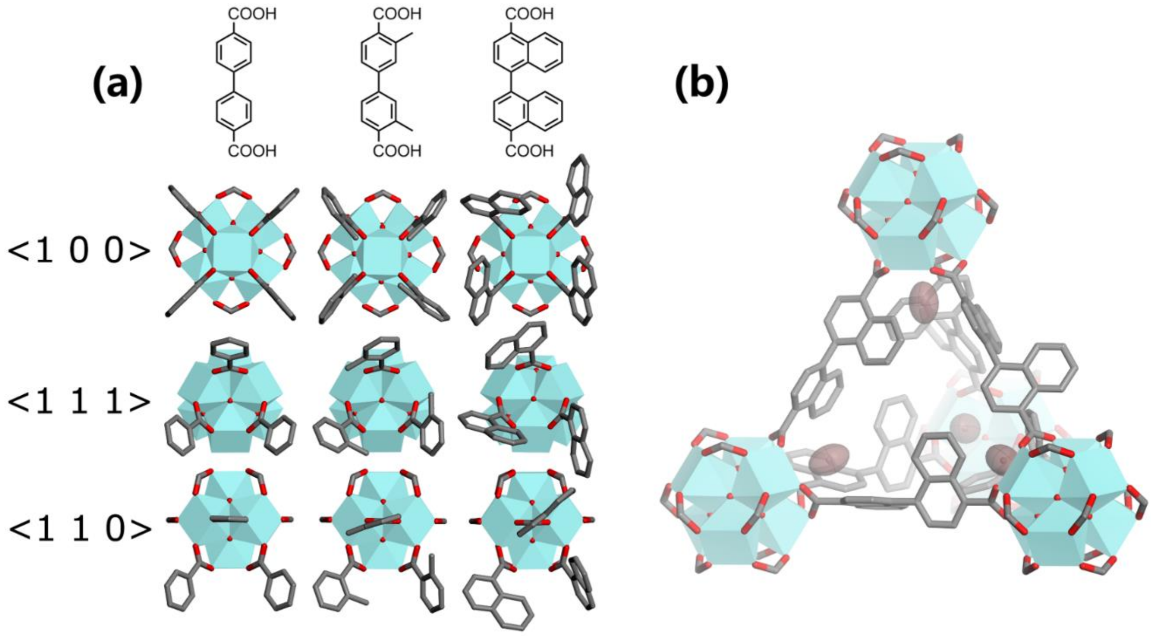

Figure 22.(a): Views of the Zr_6-cluster of UiO-67, and its dimethyl and binaphthyl analogues from the [100],[111], and [110] directions. (b): Locations of the strong adsorption sites (red transparent ellipsoids) in the tetrahedral cage of UiO-67-binaphthyl as determined from SC-XRD.

3.2.3 UiO-67-NO_2

A short discussion on the newly synthesized, as yet unpublished, UiO-67-NO_2 is included to provide a reference material for the discussion on water stability in the next section. The MOF was synthesized in a normal solvothermal synthesis using benzoic acid as modulator. The synthesis is described in detail in appendix A1 on page 86.

The crystal structure of this MOF was challenging to solve, as the linker is disordered over two configurations. The Zr cluster has 8 μ^3-O/OH sites, each of which constituting a corner of a tetrahedral cage. In UiO-67-NO_2, each of these cage corners are occupied by an O atom of a nitro group, at a distance 3.07 Å from the μ^3-OH oxygen atom (Figure 23b). Of course, the 12 linkers anchored to each cluster each harbor a nitro group, 8 of which interact with the μ^3-O(H) oxygen atom, while the remaining 4 display a similar configuration to that of the methyl group in UiO-67-dimethyl (Figure 23c, see Figure 22 for UiO-67-dimethyl), with a torsion angle between the carboxylate and aryl of 20.4°. This is close to what is observed in the crystal structure of the isolated linker, see Figure 23a. The occupancy ratio of the two linker conformations was freely refined, although the total occupancy is set to 1. The ratio converges to 0.67/0.33 for the perpendicular and aligned conformations, respectively, which is very chemically satisfying. In further work, this MOF would be a very interesting case for the study of correlated disorder (structures that contain non-periodic order);[112] the crystal structure refinement cannot provide information on local structure governed by interactions between the neighboring nitro groups. A summary of the data collection and structure refinement details can be found in appendix A2, Table 6 on page 96.

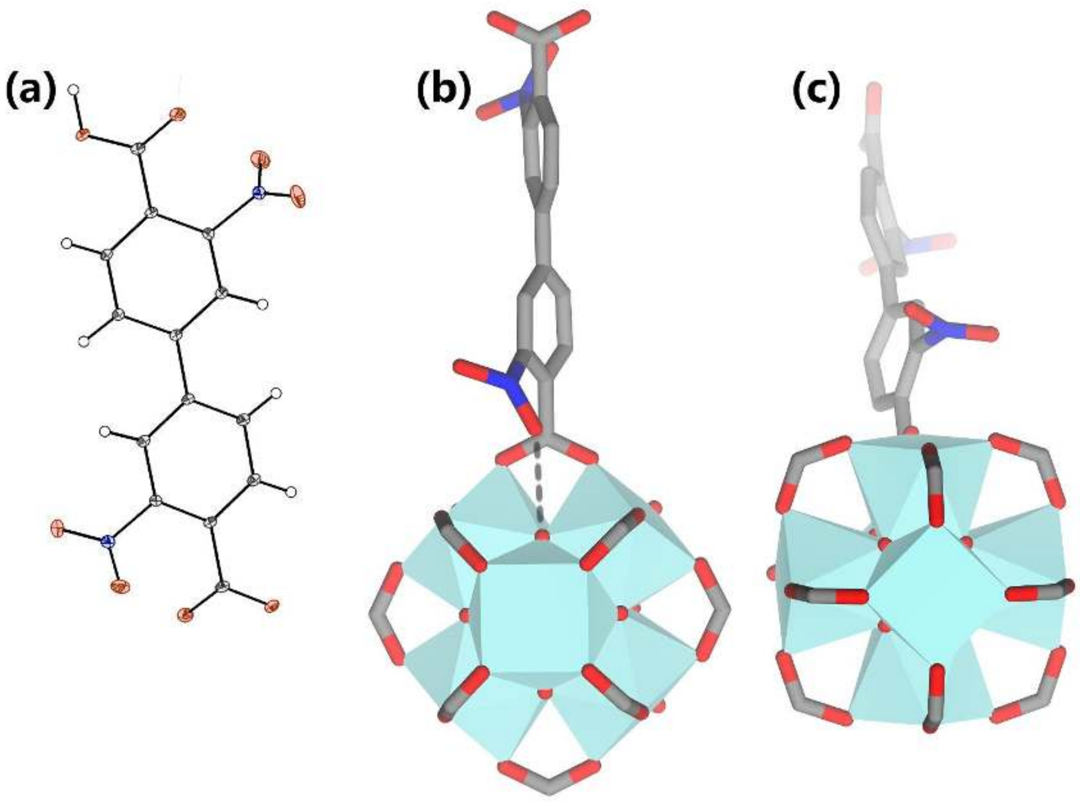

Figure 23. (a): The molecular structure of H$_2$bpdc-(NO$_2$)$_2$ showing the alignment of the nitro and carboxylate groups. (b): Predominant (67 %) conformation of the linker in UiO-67-NO$_2$, with the nitrophenyl perpendicular to the carboxylate group and (c) the minor (33 %) configuration with nitrophenyl aligned with the carboxylate.

3.2.4 Water stability

The water stability of UiO-67 has been the subject of several investigations. It was previously assumed that the MOF was unstable to water, as exposure to liquid water and subsequent drying invariably results in a dense amorphous phase. However, it was recently reported by Mondloch et al. that UiO-67 is indeed stable to liquid water (as is evident by PXRD patterns obtained by UiO-67-water slurries), and that the structure can be preserved after water exposure by exchanging the water with a less polar solvent before drying the MOF powder.[108] Thus, the hypothesis that the main pathway of UiO-67 decomposition in water is due to hydrolysis of the linker – Zr bonds was rejected. The authors make a strong case for a mechanical decomposition pathway, and suggest the main reason for decomposition is capillary-like forces acting on the framework during water removal.

Surprisingly, UiO-67-binaphthyl was found to be water stable when directly dried from a water suspension, and even from aqueous solutions of a wide pH range. To show this improvement, PXRD patterns and N_2 adsorption isotherms were acquired on UiO-67, UiO-67-dimethyl, and UiO-67-binapthyl at 3 different stages: 1) in the as-synthesized form, 2) after water suspension and solvent exchange, and 3) after drying directly from a water suspension. As can be seen from Figure 24, the PXRD pattern obtained on UiO-67-binaphthyl remains unchanged after the material is dried directly from a water suspension, whereas UiO-67 and UiO-67-dimethyl undergo structural degradation after this treatment. All 3 samples retain their crystallinity if a solvent exchange is performed before drying.

Remarkably, the N_2 adsorption isotherms (see Figure 25) show that the porosity of UiO-67-binaphthyl is nearly unaffected by drying directly from a water suspension. UiO-67 completely loses its porosity after the same treatment, while UiO-67-dimethyl loses roughly half of its adsorption capacity, indicating that the MOF is still porous even though the PXRD pattern shows an almost complete loss of structure.

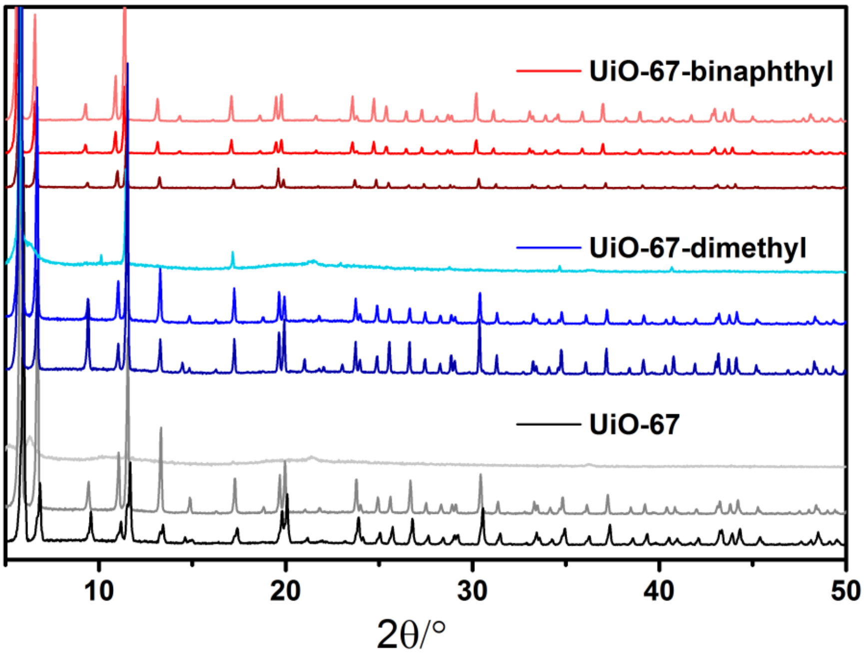

Figure 24. PXRD patterns of UiO-67, UiO-67-dimethyl and UiO-67-binaphthyl as-synthesized (dark); after water treatment at 150 °C followed by THF exchange (medium); after direct drying from water suspension (light).

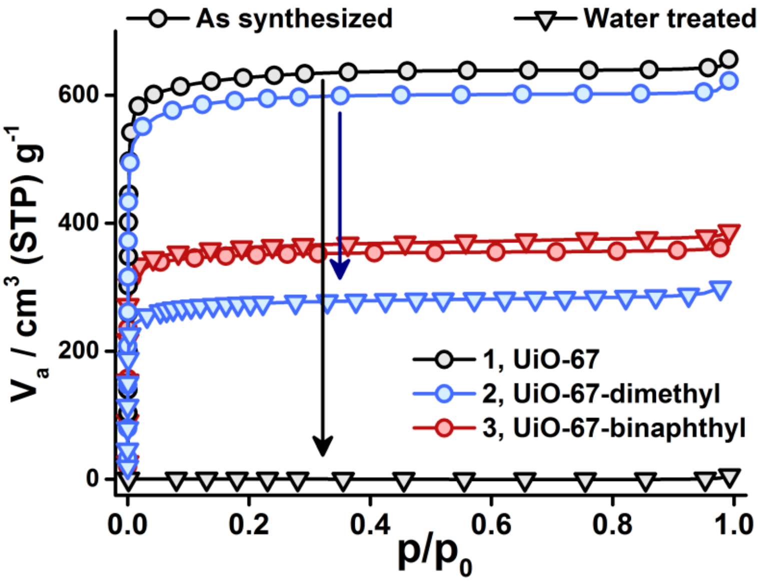

Figure 25. N_2 isotherms of UiO-67 (black), and its dimethyl (blue) and binaphthyl (red) analogues. The isotherms obtained from as-synthesized MOFs are shown as circles, while those acquired from MOF which has been dried directly from a water suspension are shown as triangles. The arrows are shown to highlight the decrease of adsorption capacity after water treatment.

At this point, it was still unclear which of the MOFs' structural features contributed most to the increased stability to water; the reduction in pore volume or the protection of the cluster by hydrophobic groups. While numerous UiO-67 derivatives with functional groups *ortho* to the carboxylate groups have been reported,[23,96] all of these will naturally provide some steric shielding of the cluster, but also reduce the MOF's pore volume. It has been observed that both hydrophilic (OH functionalized UiO-67, MOF-806)[23] and hydrophobic (UiO-67-binaphthyl, this work) groups give enhanced stability when compared to UiO-67. However, OH functionalized UiO-67 (MOF-806) shows a significant decrease in water adsorption capacity between each cycle, albeit a bit less instantaneous than UiO-67.[23] The steric coverage of the cluster from the nitro groups in UiO-67-NO_2 is similar to that of the alkyl methyl and aryl in the hydrophobic UiO-67 types, but only the naphthyl group is able to completely preserve the MOF structure in harsh water treatments.

3.2.5 Adsorption properties

The three MOFs were compared in cyclic water adsorption/desorption measurements. Both UiO-67 and UiO-67-dimethyl showed severe deterioration between each adsorption cycle, but UiO-67-binaphthyl displayed only minor degradation and showed a distinct type IV isotherm.

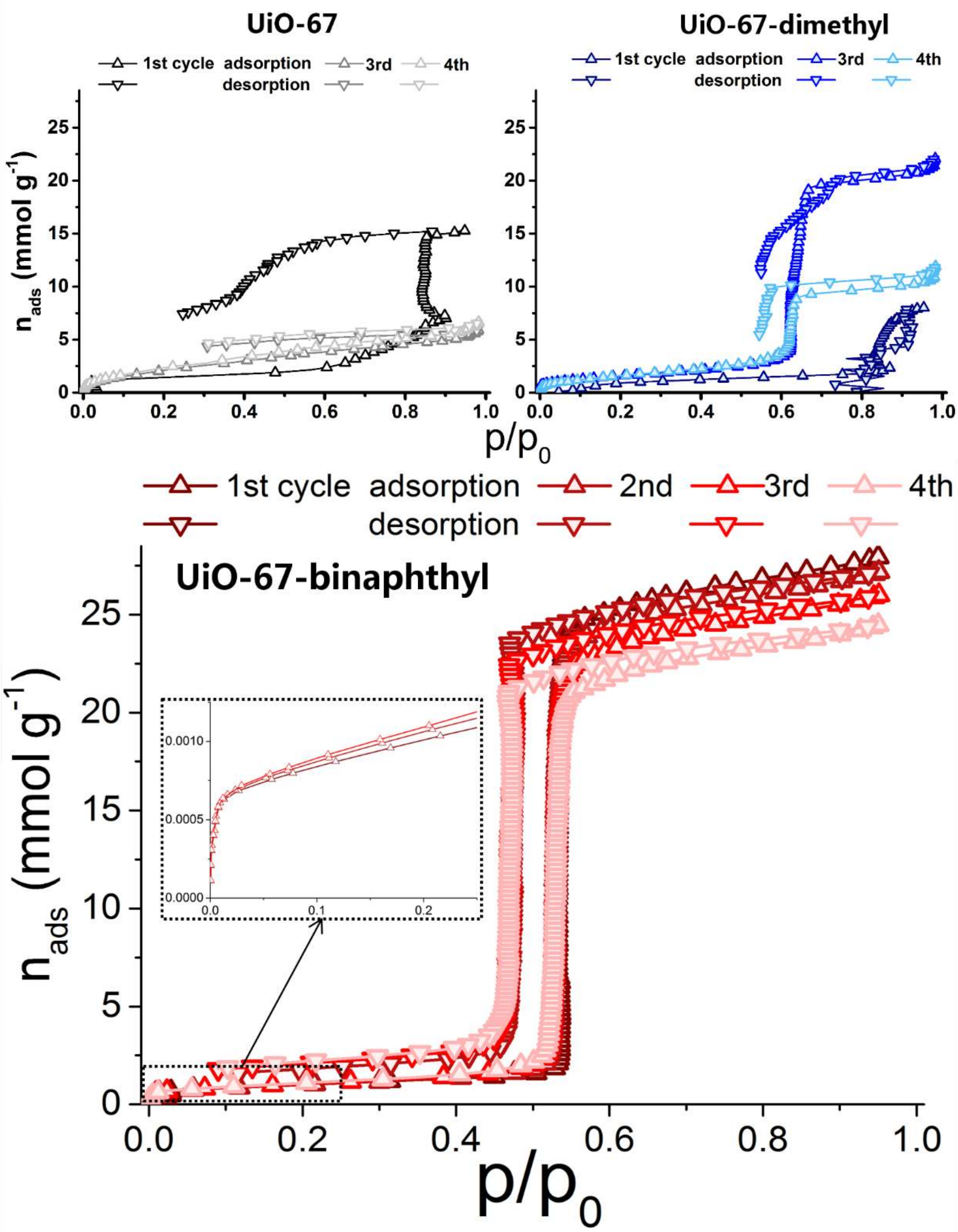

Figure 26. Water adsorption isotherms of UiO-67 (black), and its dimethyl (blue) and binaphthyl (red) analogues. For UiO-67 and UiO-67-dimethyl, the 2nd isotherms are not reported due to instrument failure.

The first water adsorption/desorption isotherms of both UiO-67 and UiO-67-dimethyl were ill defined, and few conclusions can be made with the existing data. For instance, it was not possible to determine the water adsorption capacity of the pristine materials. Whereas UiO-67 is completely decomposed after the first cycle, UiO-67-dimethyl undergoes partial decomposition during desorption, as can be seen by a critical loss in water capacity during cycling. Given that both MOFs are stable in liquid water, their behavior during the 1st adsorption cycle were surprising, and the reason for the strangely shaped isotherms is still unclear. In water adsorption experiments, very long equilibration time is used between each measuring point. One possibility is that the materials undergo partial degradation during this equilibration period.

All four cycles of water adsorption measured on UiO-67-binaphthyl at 30 °C exhibit remarkable type IV adsorption isotherms, featuring a well-defined hysteresis loop with two virtually vertical and nearly parallel branches (Figure 26). This is generally associated with porous materials having a narrow pore-size distribution. Although a small decrease of adsorption capacity between each cycle is observed, the relative stability is remarkable for a UiO-67-type MOF. While the cause of this decrease in capacity is unknown, it is likely connected to missing linker defects, as this has been shown to have a significant impact on Zr-MOF stability.[35-37,93] It may also be affected by the harsh regeneration conditions employed between each cycle, where the powder is heated at 250 °C overnight under vacuum.

The adsorption isotherm has three distinct parts; before, during, and after the water condensation. Initially ($p/p_0 = 0.0 - 0.4$), it exhibits a non-negligible rise in adsorption (for $p/p_0 = 0.0{-}0.02$), followed by a linear segment (for $p/p_0 = 0.02{-}0.4$). If we consider the crystal density of 0.937 for this material, the initial amount of water adsorbed at this stage (n_0) corresponds to 0.645 mmol cm^{-3}, or to about 7.5 water molecules per unit cell, which is in good agreement with the 8 water molecules (2 per Zr_6-cluster) expected to undergo chemisorption upon rehydroxylation of the cluster. According to the Langmuir equation, more than 90% of the rehydroxylation is completed at a relative partial pressure as low as $p/p_0 = 0.015$.

At $p/p_0 = 0.50$, just before the water condensation starts, the physisorbed water loadings range from 10 to 16 water molecules per unit cell between cycle 1 and cycle 4. At low pressure, the most favorable sites for water adsorption are at the corners of the tetrahedral cages where the capping μ^3-O(H) groups are pointing. This means that, before the steep uptake arises, there are no more than 1−2 water molecules per tetrahedral cage on average. Although this loading is relatively small, these molecules still could take part in the formation of water microclusters around primary adsorption sites, which is generally widely accepted as the prior step to micropore filling in hydrophobic porous materials.[113]

With the assumption that confined water has a density close to that of liquid, 90% of the pore volume (0.548 cm^3/g) of UiO-67-binaphthyl is filled at maximum uptake (total uptake of 0.495 cm^3 $H_2O_{(l)}$ per gram at $p/p_0 = 0.9$). Despite the expected larger hydrophobicity of the framework, the pore filling is much more efficient in this sample than in the other two MOFs. As already suggested by Cmarik et al. for the dimethoxy-functionalized UiO-66 (UiO-66-2,5-$(OMe)_2$),[114] the linker is in certain cases likely to be acting as a "directing agent", allowing a much more efficient packing of the water molecules.

To investigate the how the adsorption properties of the material is affected in a more general sense, methane and CO_2 adsorption isotherms were also measured for the three MOFs. The isotherms are reported with volumetric uptakes (rescaled using the crystal density of the materials) in addition to gravimetric, to more intuitively compare the effects of linker functionalization on the gas adsorption (Figure 27).

The volumetric CH_4 adsorption capacity (Table 2), derived from the isotherms obtained at 25 °C (Figure 27), is moderate for all three MOFs, and below the best performing MOFs.[46] Despite the steric shielding of the cluster corners (which are the preferred gas adsorption sites shown in Figure 18)[29] and above all the reduction of porosity (by 26%), the volumetric methane capacity is highest for UiO-67-binaphthyl. This observation seems to encourage the adopted strategy of functionalizing the linker with aryl groups to enhance the interaction with the framework and thus the methane adsorption capacity.

The isosteric heat of adsorption (at zero coverage) increases with the functionalization of the linker, being 15.2 kJ mol^{-1} for UiO-67 and 20.3 kJ mol^{-1} for UiO-67-binaphthyl. This leads to a high uptake at low pressure, thus rather limiting the working capacity. The improved adsorption efficiency compensates very elegantly for the loss of pore volume over this MOF series, and the working capacity at both 5 - 35 and 5 - 65 bar is surprisingly similar for the three MOFs investigated.

Table 2. Adsorption uptakes of CH_4 and working capacities (considering desorption at 5 bar) at 25 °C. Volumes are given in cm^3(STP) cm^{-3}.

	P = 35 bar		P = 65 bar	
	uptake	working capacity	uptake	working capacity
UiO-67	102	72	127	104
UiO-67-dimethyl	113	75	135	104
UiO-67-binaphthyl	124	72	147	104

The volumetric isotherms of CO_2 adsorption (Figure 27) show the expected significant decrease in uptake throughout the MOF series, in line with the reduction of the pore volume. By physical volume only, an even more pronounced decrease in adsorption capacity would have been expected for UiO-67-binaphthyl compared to the other MOFs in this study. On the contrary, it exhibits a behavior very similar to UiO-67-dimethyl at moderate and high pressures. Thus, the packing of CO_2 molecules is improved in this more confined space, as was the case for water adsorption.

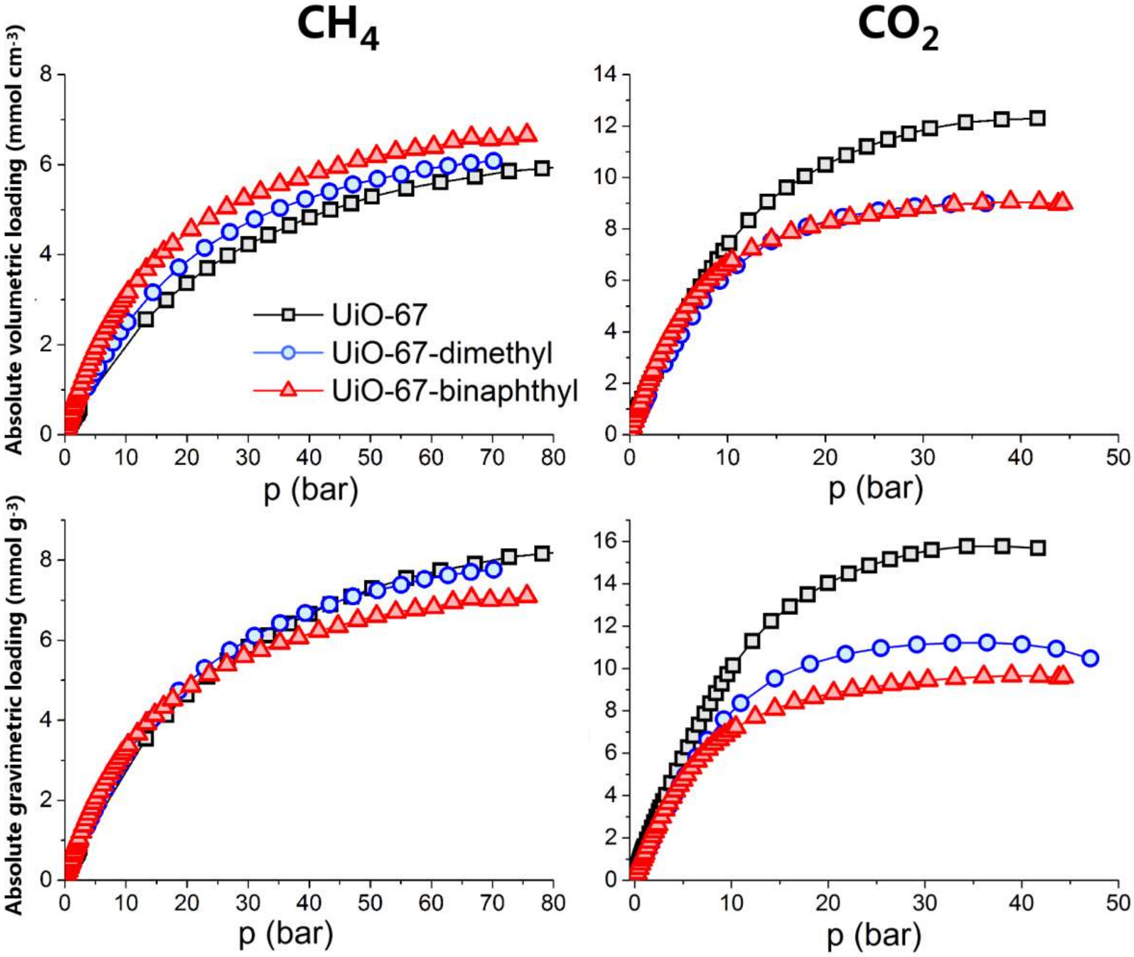

Figure 27. Adsorption isotherms acquired at 25 °C of methane (left) and CO_2 (right) showing both volumetric (top) and gravimetric (bottom) uptake.

3.2.6 Beyond paper III: Naphthyl functionalized UiO-68

The functionalized terphenyl-based linker H_2tpdc-Me_2 (Figure 28) was synthesized as part of the work described in **paper II**. The MOF UiO-68-dimethyl (or PCN-56) was obtained by solvothermal synthesis as previously reported by Jiang et al.[94] The PXRD pattern of the as synthesized material confirmed the formation of a face centered cubic crystal structure with the expected unit cell parameters of UiO-68. The crystal structure was solved by SC-XRD, and is matching the published PCN-56.

Following the successful synthesis of truly water stable UiO-67, a bis-naphthyl-functionalized linker was developed, 4,4'-(1,4-phenylene)bis(1-naphthoic acid) (H_2pbndc, Figure 28). Two UiO-68 analogues were synthesized: one using only the bis-naphthyl linker, and the other with a 0.50/0.50 mixture of the bis-naphthyl and dimethyl linker. Full synthesis descriptions are found in appendix A1 on page 86.

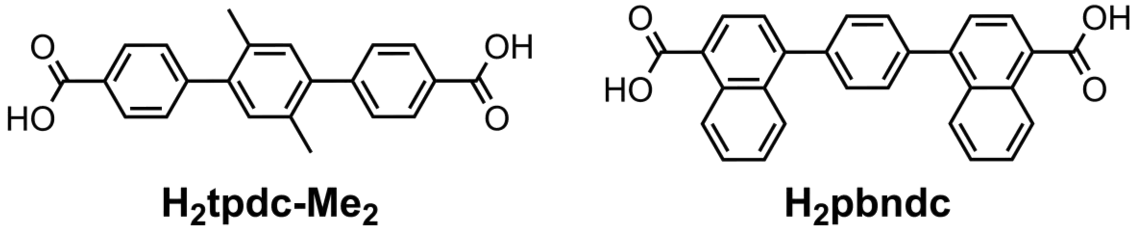

Figure 28. Linkers used in UiO-68 synthesis, 2',5'-dimethyl-[1,1':4',1''-terphenyl]-4,4''-dicarboxylic acid (H_2tpdc-Me_2) and 4,4'-(1,4-phenylene)bis(1-naphthoic acid) (H_2pbndc).

Single crystals suitable for SC-XRD of the mixed linker MOF were obtained using benzoic acid as modulator. Interestingly, single crystals of the pure bis-naphthyl UiO-68 were most easily obtained using NBA as modulator, thus showing similar behavior as the UiO-67 analogue.

The crystal structure of UiO-68-bis-naphthyl shows similar angles between the carboxylate group and the naphthyl groups as in UiO-67-binaphthyl (shown in Figure 29); at 36.4 ° (the corresponding angle in UiO-67-binaphthyl being 41.1°). This is somewhat interesting, since there is no intramolecular steric conflict between the naphthyl groups as there is in binaphthyl. In the structure of the linker in its molecular form, the angle is also much smaller, at only 18.5°. The orientations of the naphthyl groups are very similar in both MOFs, pointing to intermolecular interactions and interaction with the cluster as determining factors. A summary of the data collection and crystal structure refinement details are found in appendix A2, Table 7 on page 97.

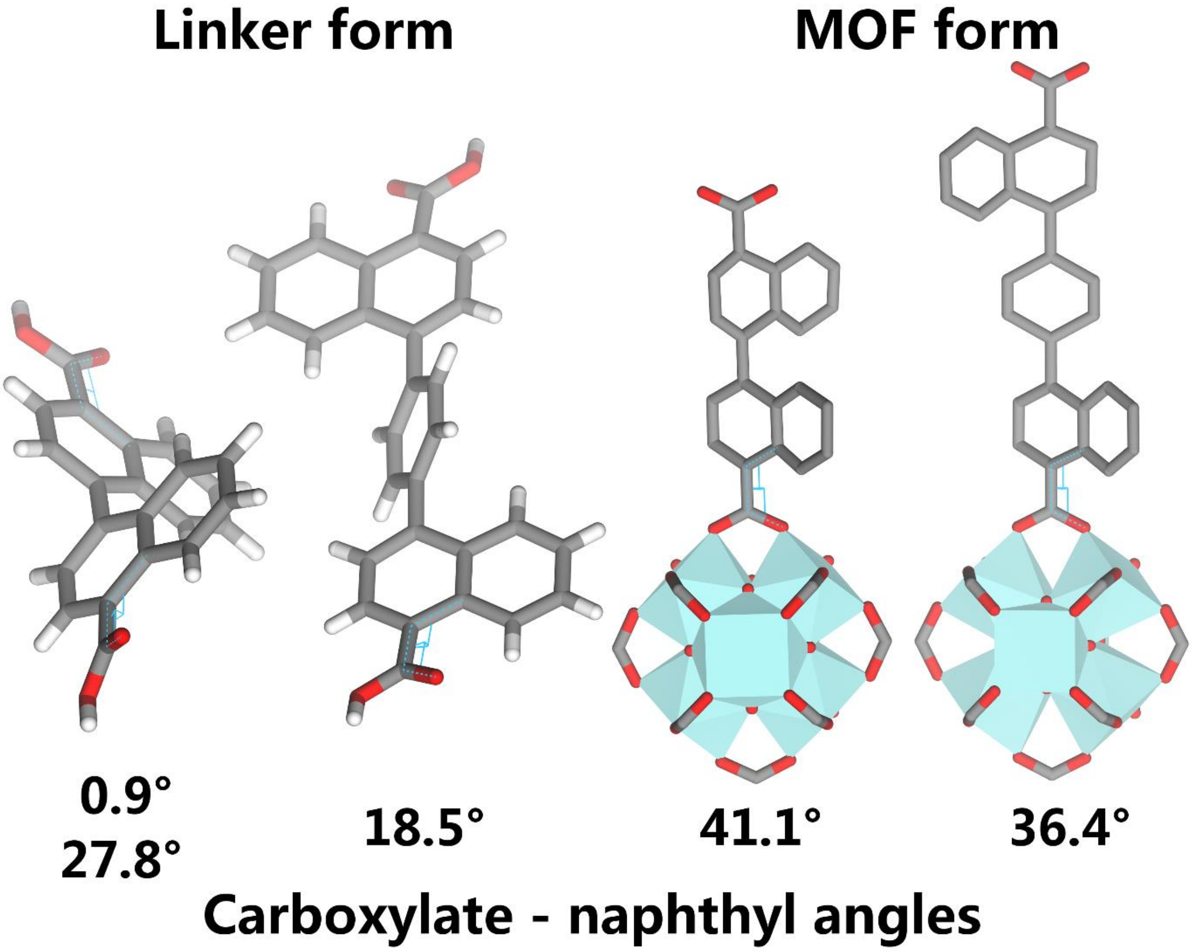

Figure 29. Carboxylate - naphthyl angles in binaphthyl linkers and MOFs. The measured angles are highlighted with blue lines.

The newly synthesized analogues showed very poor stability to water, decomposing both after drying directly from a water suspension, and after solvent exchange with acetone following water suspension. Jiang et al. found that PCN-56 was partially stable in water,[94] suggesting that the samples reported herein were more defective. However, after performing a postsynthetic linker insertion step (in some cases referred to as a "healing" step),[115,116] UiO-68-bisnaphthyl showed remarkable stability to water (as is evident by recorded PXRD patterns, shown in Figure 30). In the postsynthetic linker insertion step, 200 mg of UiO-68-bisnaphthyl was suspended in a solution of 100 mg H_2pbndc in 10 mL of DMF, and kept at 120 °C for 24 hours. This was followed by the same washing procedure as after synthesis. Both the as-synthesized MOF and the postsynthetically modified were subjected to the same water stability tests as those reported for the UiO-67 samples in section 3.2.4. Homogeneous aqueous suspensions of both samples were prepared. After soaking for 2 hours, the samples were recovered by filtration and divided into two portions each. One was directly dried at 160 °C whereas the other was solvent exchanged twice with acetone and then dried at 160 °C.

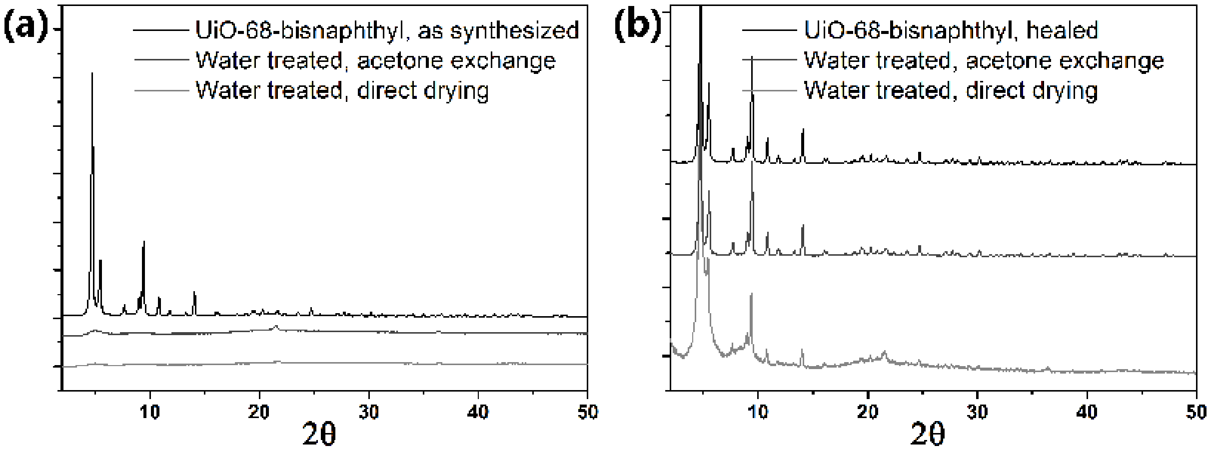

Figure 30. PXRD patterns of UiO-68-bisnaphtyl (a) before and (b) after postsynthetic linker insertion.

The preliminary results indicate that UiO-68-bisnaphthyl has greater stability to drying from aqueous suspension than other UiO-68 analogues. It is also shown that the as-synthesized MOF contains defects that can be removed (at least partially) by a postsynthetic step to increase the MOFs stability. The sample was synthesized using 4-nitrobenzoic acid as modulator, and it is reasonable to assume that this modulator contributes to high defect concentration in the MOF, given its low pK_a value (as discussed in section 3.2.1).

3.2.7 Beyond paper II: UiO-69-Me_2

UiO-69-Me_2 was successfully synthesized as single crystals using the linker (H_2qpdc-Me_2, Figure 28). Using 30 equivalents of benzoic acid with respect to $ZrCl_4$ as modulator, single crystals of 200 μm and larger could be obtained (examples shown in Figure 31). A detailed synthesis description can be found in appendix A1 on page 86. Surprisingly, the MOF showed remarkable chemical stability, comparable to that of UiO-67 (discussed in section 3.2.4). Upon microscope observation of one sample used for SC-XRD measurements, it was noted that the octahedral single crystals featured a distinct optically opaque pattern originating from the center of each crystal and out to each facet, shown in Figure 31.

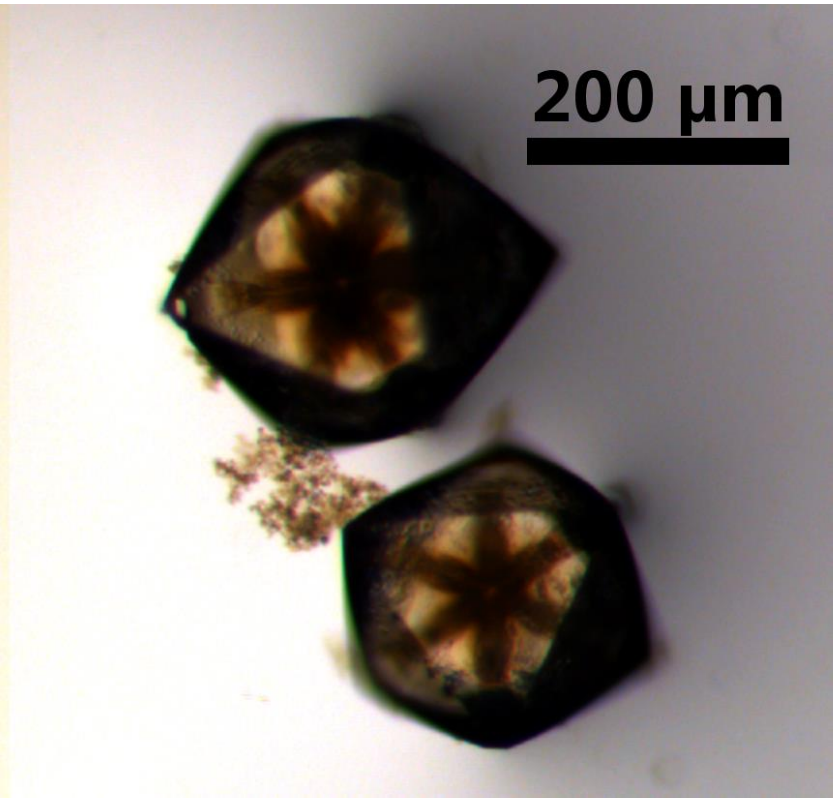

Figure 31. Single crystals of UiO-69-Me$_2$.

Quaterphenyl-based Zr-MOFs have been reported as isoreticular to UiO-66, 67 and 68.[117] Analysis of the reflection intensities obtained for this UiO-69-Me$_2$ suggested a centrosymmetric face centered cubic structure in the Laue group $m\bar{3}m$. However, structure solution in $Fm\bar{3}m$ (the space group of the other UiO MOFs) was unsuccessful. The newly developed structure solution program XT determines the space group based on input reflection data, and a solution in space group $Fd\bar{3}m$ was obtained. This structure solution suggested a MOF consisting of two identical, interpenetrated fcu-lattices, isoreticular to the PIZOFs.[31] However, the structure refinement gave very poor validation factors (R1 > 12 %) despite a well-defined model, which suggests space group mis-assignment.

When a structure appears centrosymmetric by analysis of reflection intensities, it could in reality be an inversion twin of two equally large domains.[118,119] Consequently, the structure was solved in Laue group $\bar{4}3m$ (a sub-group of $m\bar{3}m$), and the inversion matrix was applied in the structure refinement, resulting in a well-defined structure and good confidence factors. Rigid body restraints were used on a few C atoms to obtain physically meaningful ADP values.

By this strategy, additional information was obtained. Most interestingly, the two interpenetrated lattices are not identical. The structure consists of a primary lattice, and a secondary interpenetrated lattice with an occupancy factor of 0.63, indicating that about a third of the crystal consists of a very open non-interpenetrated lattice. This kind of partial interpenetration is unusual, but was also very recently reported by Ferguson et. al.[120] The reduction in symmetry is not just a result of the difference in occupancy between the two lattices. Neighboring clusters from the separate lattices have a clear tendency to orient opposite functionality towards each other (Figure 32). Interestingly, the clusters in the fully occupied lattice tend to orient their μ^3-O groups towards the μ^3-OH groups on the partially occupied neighboring cluster. Otherwise, the interpenetration mode is similar to that observed in the PIZOF series.[31] The stability of these MOFs with respect to UiO-68 analogues are probably due to the reduced pore volume resulting from interpenetration. The twinning in UiO-69-Me$_2$ can be visualized by displaying the two possible settings of the interpenetrating lattice (Figure 33a). Summary of the data collection and details obtained at different stages of structure refinement can be found in appendix A2, Table 8 on page 98. The synthesis and SC-XRD measurement of UiO-69-Me$_2$ has been reproduced, and the obtained structures are identical apart from different occupancy coefficients.

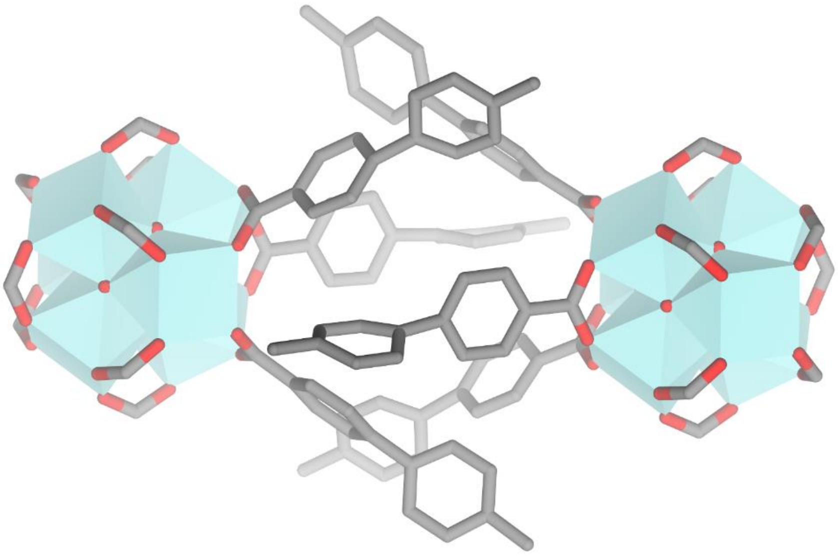

Figure 32. Neighboring clusters from each of the interpenetrated networks of UiO-69-Me$_2$. The interpenetrated lattices direct the μ^3-O groups and μ^3-OH groups towards each other, as determined by SC-XRD.

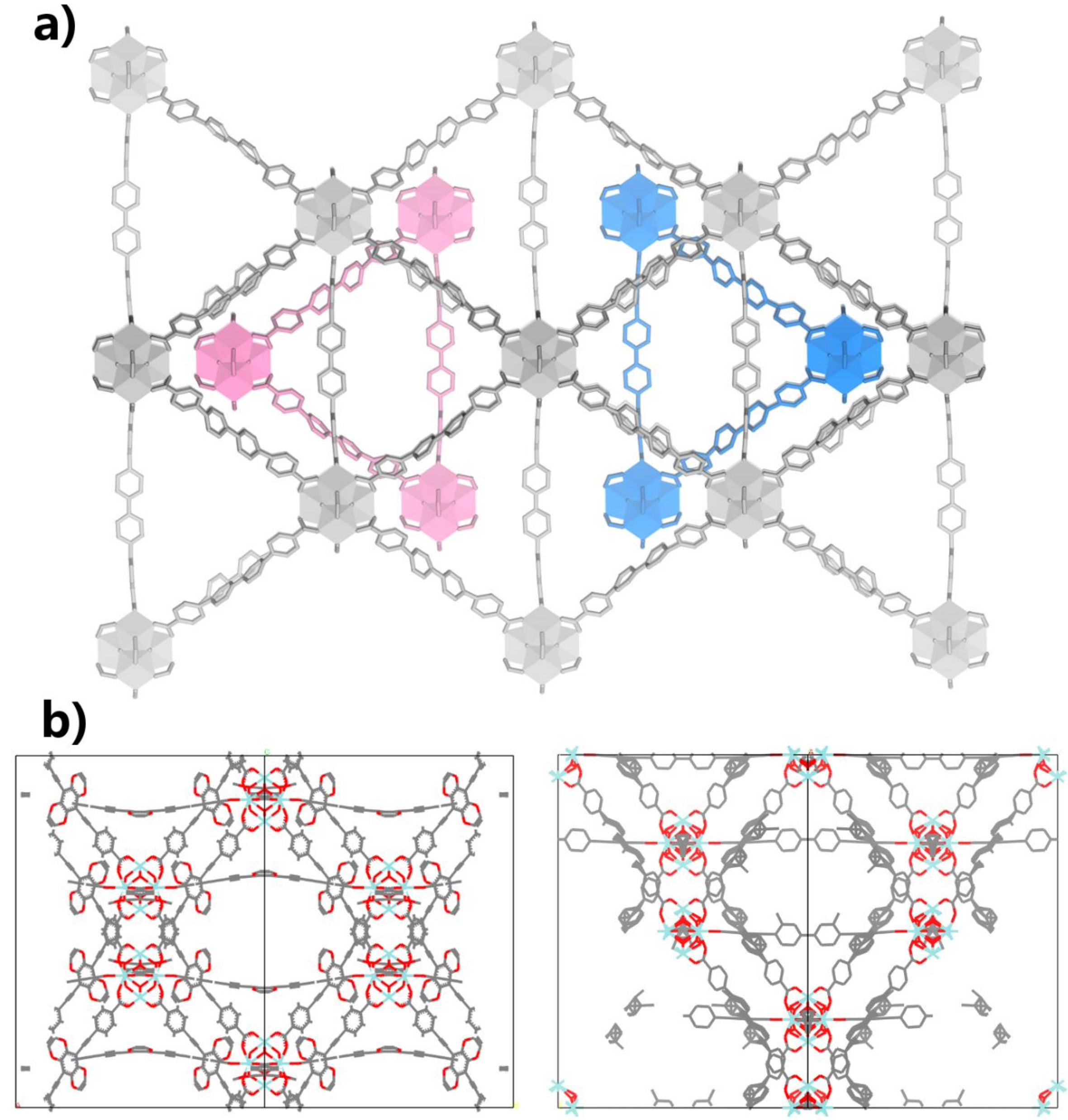

Figure 33. **a)** Relationship between the two conformations of the partially occupied lattice (blue and pink) inside the main lattice (grey). **b)** The similar topology of PIZOF-2 (left) and UiO-69-Me_2 (right) viewed along the [1 1 0] direction.

The opaque pattern in the crystals must originate from an un-even index of refraction, which is likely due to cracking of the crystal. Cracks could occur under mechanical stress, or as a result of partial collapse. Given the open structure, it is likely that non-interpenetrated regions of the UiO-69-Me_2 crystal have also partly degraded. This is supported by adsorption measurements: A crude geometric calculation shows that the N_2 accessible surface area for a fully interpenetrated UiO-69-Me_2 is 2400 m^2g^{-1}, but the experimentally obtained BET surface area of the sample was only 1950(50) m^2g^{-1}.

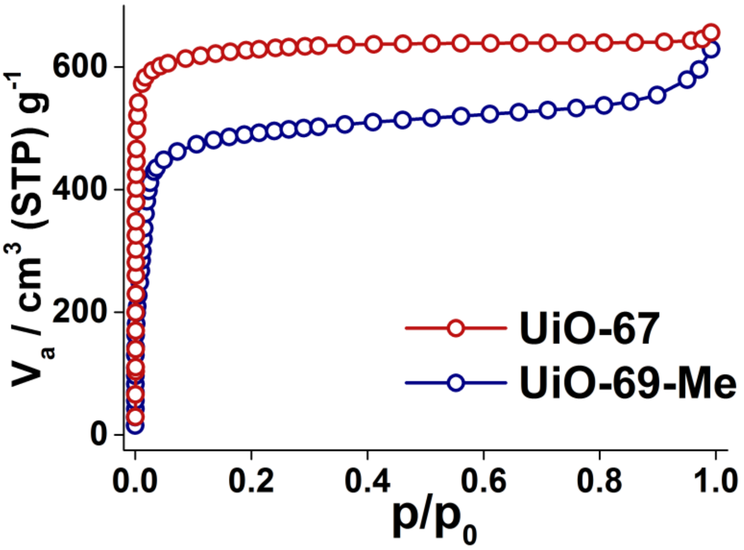

Figure 34. N_2 adsorption isotherms of UiO-69-Me_2 and UiO-67 (from **paper III**) for comparison.

These results clearly show that interpenetration needs to be considered in the structure determination of quaterphenyl based Zr-MOFs. It would also be interesting to examine several PIZOF structures to determine whether a partial interpenetration could occur in these structures. Considering the MOF reported in this section, it would be interesting to see if a fully interpenetrated MOF could be obtained through adjustment of synthesis parameters.

3.2.8 Summary

As hypothesized, UiO-67-binaphthyl showed higher affinity to methane than the other UiO-67 analogues. Sadly, this did not result in higher working capacity at low pressures, since a larger portion of methane was retained in the MOF at low pressures. Still, UiO-67-binaphthyl has a higher volumetric loading than UiO-67 over the whole pressure range, despite its greatly reduced pore volume.

In UiO-67-binaphthyl, the reason for the unexpected stability to water is still not fully understood. From single crystal structure determination, it has been observed that the linkers partially shield the strongest adsorption sites of the MOFs, which may account for the enhanced stability.

3.3 Reactivity of Pt and Cu sites in UiO-67

This chapter describes the work published in **paper IV** and **paper V**, along with some additional SC-XRD characterization of metal-functionalized UiO-67 samples. All EXAFS refinement and figures showing XAS data were provided by Elisa Borfecchia, Luca Braglia, Kirill Lomachenko, Giovanni Agostini and Carlo Lamberti. The results reported in the two articles are presented herein in separate sections.

Paper IV, “Probing Reactive Platinum Sites in UiO-67 Zirconium Metal−Organic Frameworks”, concerns the synthesis and characterization of platinum functionalized UiO-67, whether in the as-synthesized form, during activation/solvent removal, or in reaction with substrates in the liquid and gas phase.[121]

Paper V, “Exploring structure and reactivity of Cu sites in functionalized UiO-67 MOFs”, follows an analogous approach as in **paper IV**, but with copper functionalized UiO-67.[122]

UiO-67 with a fraction of 2,2’-bipyridine-5,5’-dicarboxylic acid (H_2bpydc) linkers is well-suited for postsynthetic metalation and subsequently as a heterogeneous catalyst, as has been frequently reported.[27,64,123] An example of such a structure is shown in the introduction (Figure 10a on page 10). H_2bpydc is isostructural to H_2bpdc, the linker in non-functionalized UiO-67. H_2bpydc readily forms chelating complexes with a wide range of metals. Figure 35 shows the linkers used in this work, along with a Cu compound used as reference for EXAFS refinement.

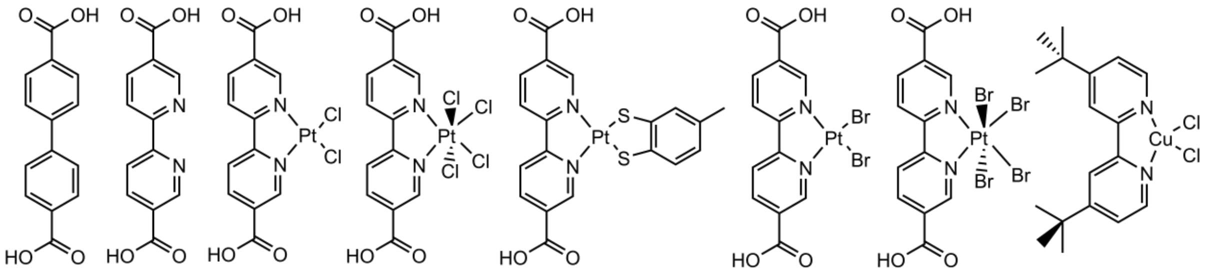

H_2bpdc H_2bpydc PtCl$_2$(H_2bpydc) PtCl$_4$(H_2bpydc) Pt(tdt)(H_2bpydc) PtBr$_2$(H_2bpydc) PtBr$_4$(H_2bpydc) CuCl$_2$(^{t}bu-bpydc)

Figure 35. Linkers used in this work, plus one Cu compound which was used as a reference for XAS spectra. All linkers have been characterized by SC-XRD and ^{1}H-NMR.

Detailed characterization of a MOF functionalized with a small fraction of metalated linkers is a serious challenge. Proper characterization is important to evaluate the effect of different functionalization methods and to provide the basis for our knowledge about the MOF’s properties and reactivity. Solution state NMR and mass spectrometry are not available since the complexes in question are part of an insoluble solid, and only limited information can be obtained by PXRD (only one refined PXRD structure of functionalized MOFs were available at the time of writing to the best of the author's knowledge).[124] Crystals of metalated UiO-67 suitable for SC-XRD had not yet been obtained when this work was published, but has since been reported in the literature and also studied as an extension of this work.[124]

3.3.1 Synthesis and structure of UiO-67-bpy($PtCl_{2/4}$)

UiO-67-bpy($PtCl_{2/4}$) was initially studied due to the linkers' similarity to complexes that are active C – H activation catalysts.[125-127] Three strategies, shown in Figure 36, were used to synthesize UiO-67-bpy$(PtCl_{2/4})_{0.1}$; MOF synthesis with pre-made linker (**PMLS**), one pot synthesis (**OPS**) in which $ZrCl_4$, linker and K_2PtCl_4 or M_2PtCl_6 (where M is Na or K) are combined in a one-step synthesis, and postsynthetic functionalization (**PSF**) where a MOF containing H_2bpydc linkers is submerged in a solution of K_2PtCl_4 or M_2PtCl_6 (in DMF), thereby forming the chelating complex directly on the lattice.

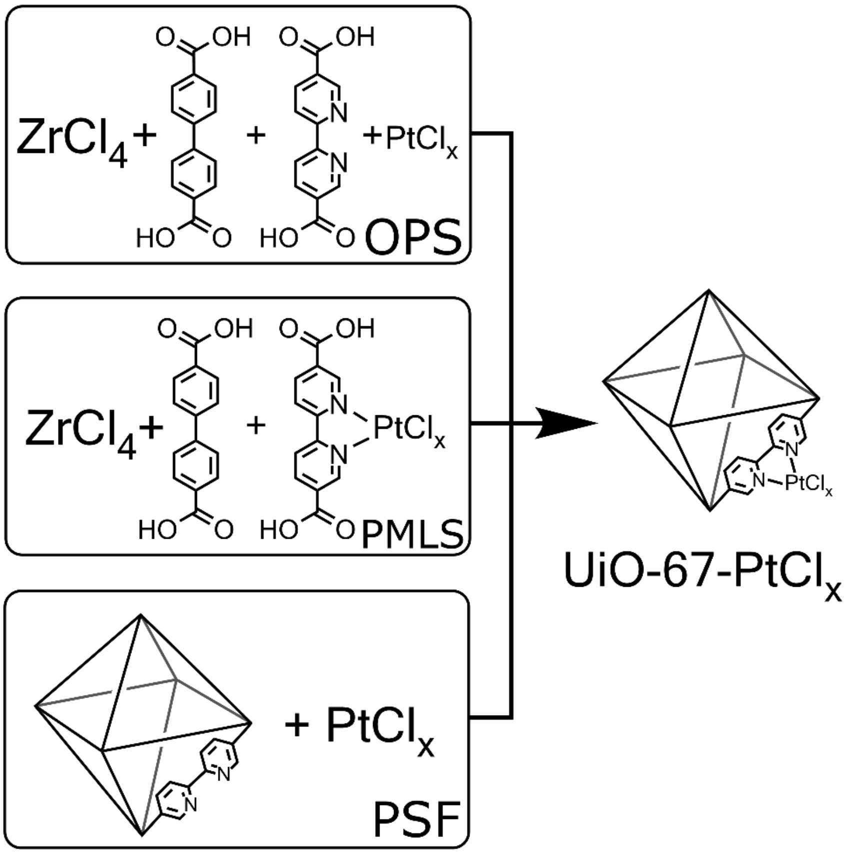

Figure 36. Schematic of the three functionalization methods used in this work to obtain UiO-67-bpy($PtCl_x$), one pot synthesis, pre-made linker synthesis and postsynthetic functionalization.

The yields of UiO-67-bpy($PtCl_{2/4}$) synthesized by a one pot method or pre-made linker method were consistently lower for these methods than UiO-67-bpy($PtCl_{2/4}$) samples obtained by PSF. Unfortunately, samples of UiO-67-bpy($PtCl_4$) made by postsynthetic metalation were not available at the time of XAS measurement. Although the highest BET surface area was obtained by using pre-made linker, the extra linker synthesis step was found to be time consuming, and gave poor yields (see Table 3 for yields and BET surface areas obtained for UiO-67-bpy($PtCl_2$)).

Table 3. Yields and BET surface areas of UiO-67-bpy($PtCl_2$) as reported in **paper IV**.

	Yield	**BET surface area**
Pre-made linker synthesis	52 % (only MOF synthesis)	2222 m^2 g^{-1}
One pot method	34 %	1504 m^2 g^{-1}
Postsynthetic metalation	80 % (including metalation step)	2083 m^2 g^{-1}

PSF proved to be efficient, with short reaction time (2 hours) in a DMF solution. Attempts to use other solvents than DMF for post synthetic metalation resulted in the formation of metallic platinum. Full procedures can be found in the supporting information of **paper IV**.

The EXAFS spectrum of $PtCl_2$(H_2bpydc) linker provided a reference for the Pt(II) functionalized MOFs, as the local environment op the Pt atoms is nearly identical. In the moduli of the spectra, the scattering contributions from Pt – N interaction and Pt – Cl interaction can be seen as two distinct peaks (Figure 37). For the samples of UiO-67-bpy($PtCl_4$), however, it was clear from the measurements that most of the Pt(IV), about 70 %, had been reduced to Pt(II) during functionalization. An in depth discussion on the EXAFS refinement can be found in **paper IV**.

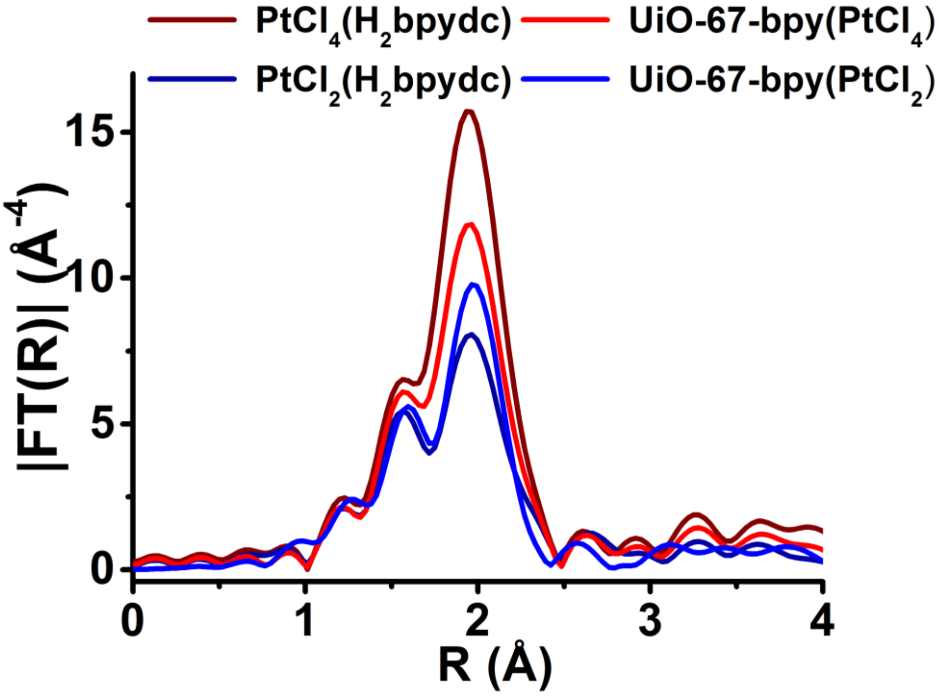

Figure 37. Moduli of the Fourier transformed EXAFS spectra obtained on the reference linkers and the MOFs (obtained by PMLS). The spectra of the MOFs obtained by PSF and OPS can be found in **paper IV**, except for UiO-67-bpy($PtCl_4$) obtained by PSF which was not available at the time of XAS measurement.

3.3.2 Beyond paper IV: Crystallographic characterization

Single crystals suitable for SC-XRD of UiO-67-bpy($PtCl_2$) were not available when **paper IV** was written. However, large single crystals of a Zr-MOF made from 90% H_2bpdc-Me_2 and H_2bpydc were synthesized shortly after. The crystals were functionalized with $KPtCl_4$ by postsynthetic metalation in the same manner as the powder sample used in the XAS measurements. The synthesis procedure can be found in appendix A1 on page 86.

The structure of UiO-67-Me_2/bpy($PtCl_2$) is similar to that of UiO-67-dimethyl in respect to the orientation of the linkers. The ADP values of all atoms in the model, including cluster atoms, were significantly larger than in the pure-linker frameworks, indicating a more disordered structure. Difference Fourier maps acquired at different stages in the refinement show the positions of Pt, Cl and methyl C atoms (Figure 38). The Pt and Cl atoms are displaced by severe libration, and had to be modelled by admitting positional disorder about two positions. The occupancy factors of Pt and Cl are not freely refined, but adjusted until the vibrational ellipsoid volumes were comparable to neighboring atoms, and the lowest R-factors were obtained. It clearly shows that bpy sites are available for functionalization, and that well-defined structures of MCl_2 functionalized MOFs can be determined when the data is of sufficient quality. Summary of the data collection and structure refinement details are found in appendix A2, Table 9 on page 99.

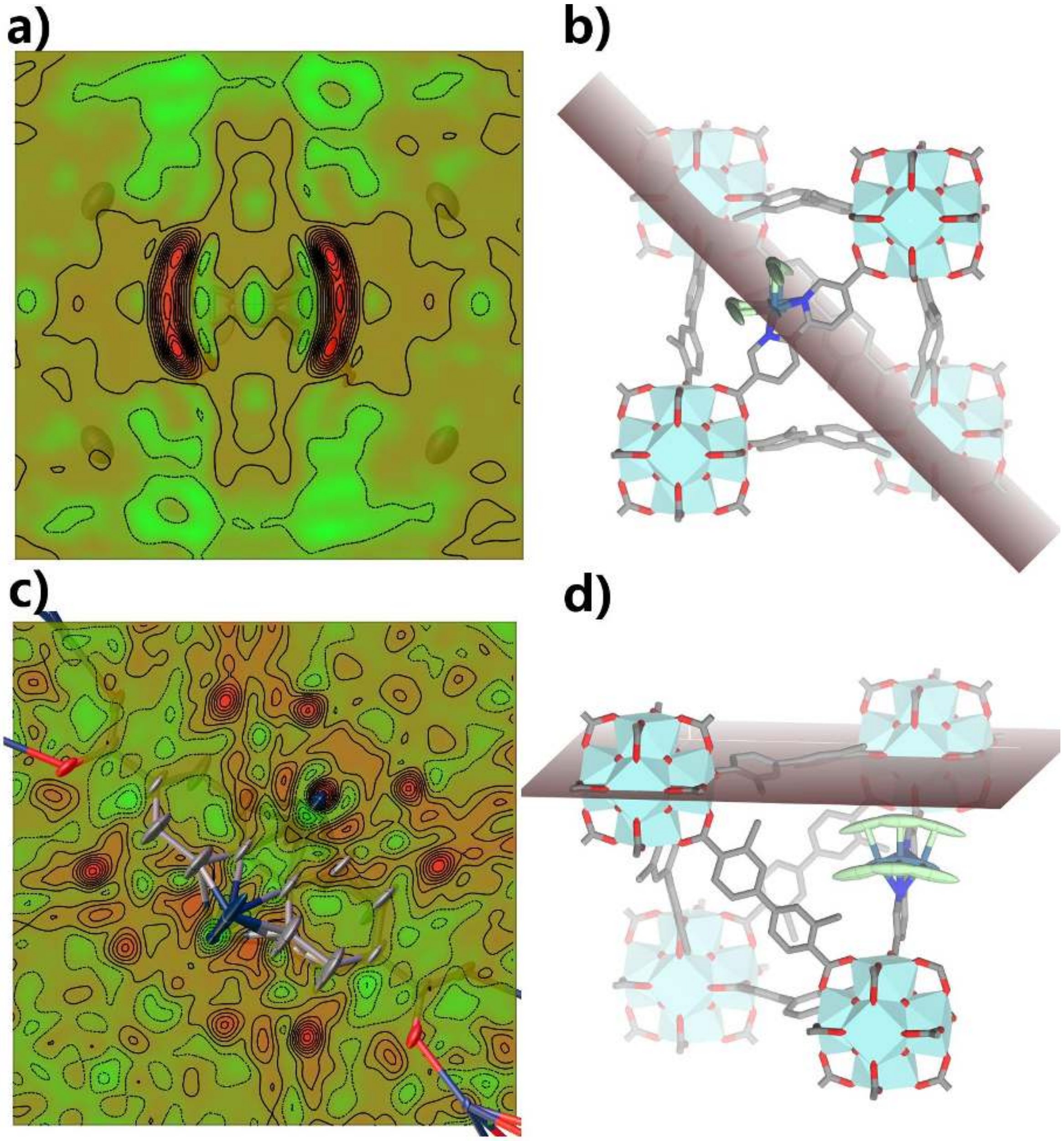

Figure 38. **(a)**: 2D Fourier difference map intersecting the expected position of Pt before including Pt, Cl and methyl ligands in the structure refinement. Pt is disordered over two symmetry equivalent positions on each side of the linker's axis of connectivity. **(b):** Representation of the plane used for the Fourier map in (a) on the structure of UiO-67-Me_2/bpy($PtCl_2$). **(c):** As (a), but the map is intersecting the expected positions of Cl and methyl ligands before they are included in the model. **(d)** Representation of the plane used for the Fourier map in (c) on the structure of UiO-67-Me_2/bpy($PtCl_2$).

3.3.3 Reactivity of Pt in UiO-67, Reduction

Temperature programmed H_2-reduction (TPR) was performed feeding the samples with a flow of 10 cm^3 min^{-1} of 3% H_2 in He, hosted inside an ad hoc conceived cell allowing temperature control and in situ XAS measurements in flux.[128] In all TPR experiments, PMLS functionalized MOFs were used. The main goal of the TPR experiment was to provide the temperature dependence of both N_N and N_{Cl} coordination numbers, and follow the expected formation of metallic Pt nanoparticles. The sample was heated at a rate of 3 °C per minute, and followed by repeated EXAFS measurements. The acquired spectra are displayed in Figure 39. In all cases, the contribution due to Pt−Cl scattering is clearly decreasing much faster than that of Pt−N, implying a reduction in the average number of Cl ligands per Pt.

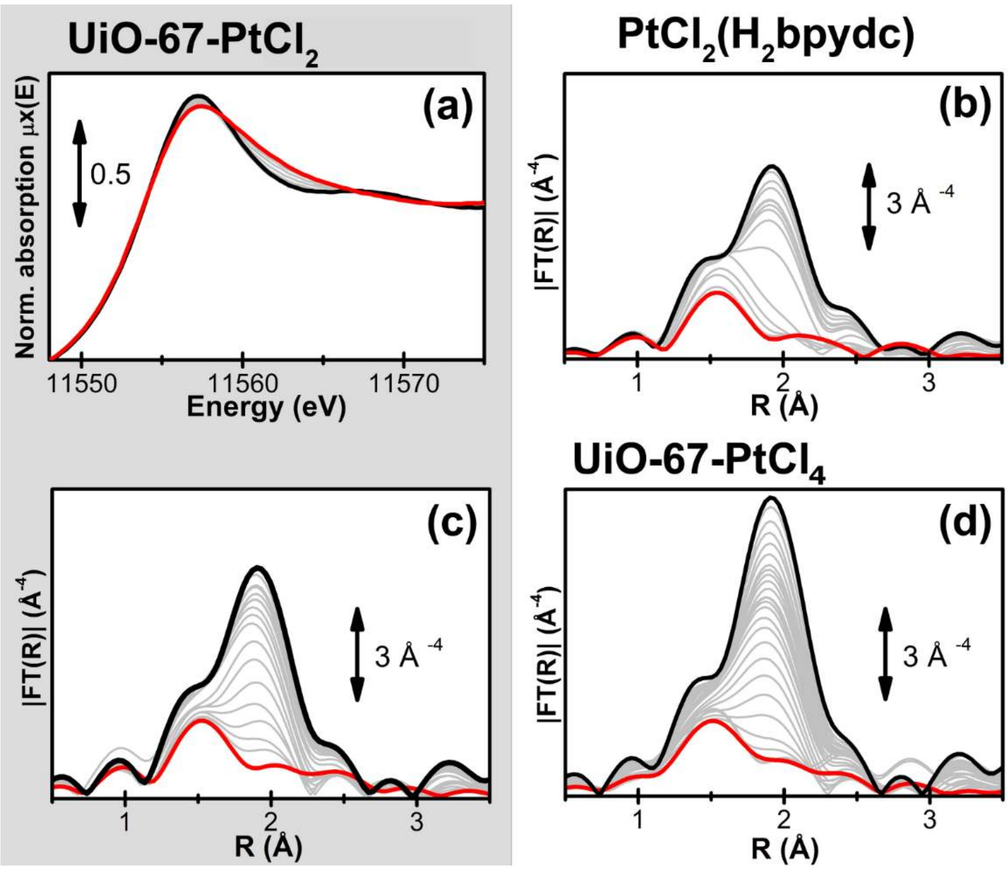

Figure 39. (a): Pt L_3-edge, XANES spectra collected during the operando TPR experiments on UiO-67-bpy($PtCl_2$). The black spectrum has been collected at RT, the red one at 470 °C, grey spectra refer to intermediate temperatures. Parts (b)-(d): k^3-weighted, phase uncorrected, FT of Pt L_3-edge EXAFS spectra collected during the operando TPR experiments on $PtCl_2(H_2bpydc)$ linker (b) and on UiO-67-bpy($PtCl_2$) (c), and UiO-67-bpy($PtCl_4$) (d) MOFs (same color code).

For the $PtCl_2(H_2bpydc)$ linker, both N_N and N_{Cl} coordination numbers are stable to the stoichiometric values of 2.0 up until 325 °C, within the experimental errors. At 345 °C, N_{Cl}

starts to rapidly decrease, approaching zero at about 450 °C. Conversely, N_N is stable until 385 °C and then starts to decrease with a much lower slope resulting in $N_N = 1.3$ at 475 °C. This means that in the 325−385 °C interval most of the Pt−Cl bonds break ($N_{Cl} = 0.4$ at 385 °C), removing the chlorine and keeping the Pt−N bonds intact.

The TPR-EXAFS experiment performed on UiO-67-bpy($PtCl_2$) yield to the same trends, with minimal differences in the temperature intervals of stability of the two bonds. Both N_N and N_{Cl} are stable to the stoichiometric values of 2.0 up to 300 °C, when they start to decrease together. However, while N_{Cl} decreases almost linearly to 0.4 at 475 °C, N_N undergoes a fast decrease to 1.6 at 335 °C and then remains relatively stable, reaching 1.4 at 475 °C. This means that a prolonged activation of UiO-67-bpy($PtCl_2$) slightly above 335 °C will result in minimal loss of Pt – N bonds, while the number of Pt – Cl bonds will decrease rapidly.

In UiO-67-bpy($PtCl_4$), the Pt−N bond exhibits the same stability interval (RT−300 °C) observed in UiO-67-bpy($PtCl_2$), after which N_N progressively decreases until it reaches 1.25 at 475 °C. The Pt−Cl bond in this MOF shows no stability plateau. N_{Cl} continuously decreases along the whole experiment exhibiting two different slopes in the RT−300 °C and 300−475 °C intervals. During the first heating step, from RT to 300 °C, all the Pt(IV) species lose two axial Cl ligands becoming square planar Pt(II) species with two nitrogen and two chlorine ligands. At that stage, they behave as in UiO-67-bpy($PtCl_2$).

The evolution of coordination numbers of N and Cl to Pt for all samples is shown in Figure 40.

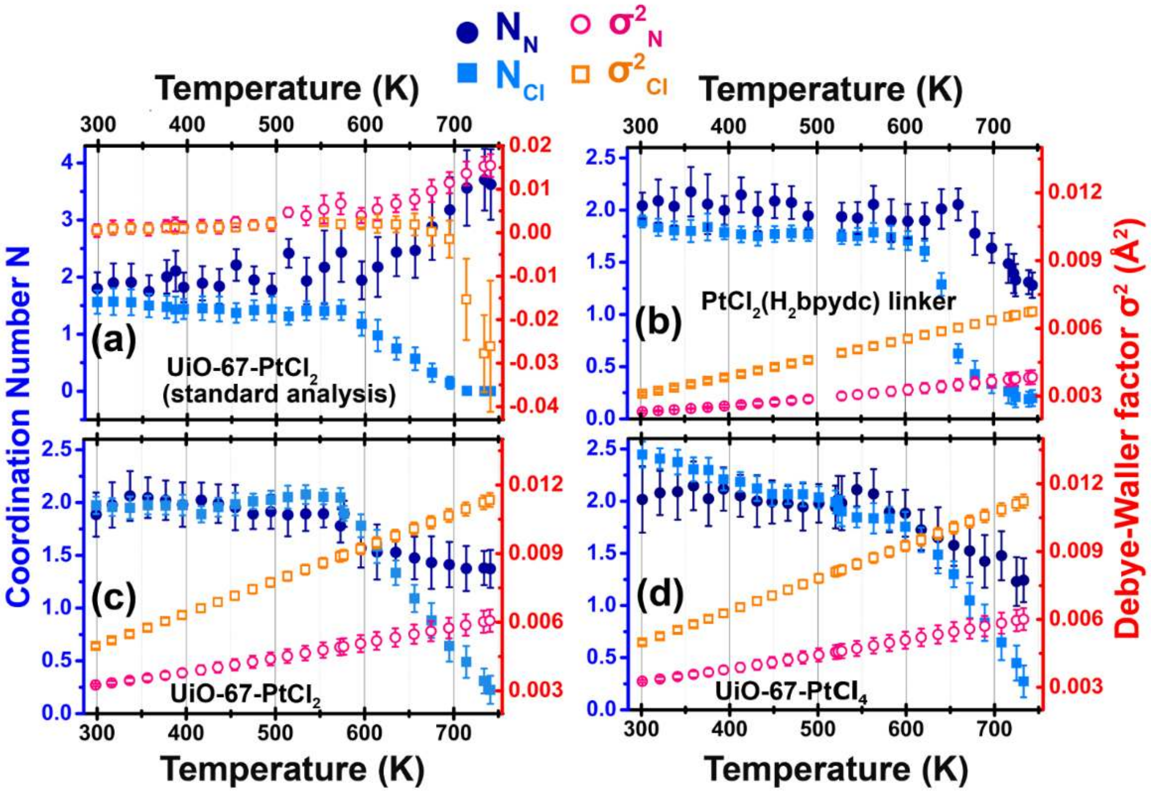

Figure 40. Part (a): standard analysis of the operando TPR-EXAFS series of spectra collected on UiO-67-bpy($PtCl_2$). Each EXAFS spectrum has been analyzed as single datum, independently from the other spectra. In the (25-325) °C range, albeit relatively high error bars and some non-physical oscillations, reported values are meaningful. In the 325-475 °C range, reported values correspond to good mathematical fits of the experimental data, but has no meaningful physical interpretation. Parts (b)-(d): final refinement of the operando TPR-EXAFS experiments on $PtCl_2(H_2bpydc)$ linker, UiO-67-bpy($PtCl_2$) and UiO-67-bpy($PtCl_4$), respectively. Data referring to the Pt–N and Pt–Cl bonds are reported as blue and cyan full-symbols and refer to the left ordinate axes. Corresponding Debye-Waller factors are reported as pink and orange open symbols and refer to the right ordinate axes.

These observations, reported in **paper IV**, were very surprising, since the expected formation of metallic Pt nanoparticles did not occur. Further efforts were initiated to examine what conditions were required to form Pt nanoparticles inside UiO-67-bpy($PtCl_2$). The experiment was reproduced, following UiO-67-bpy($PtCl_2$) by EXAFS in the same way as reported in **paper IV**, although a H_2 concentration of 10% was used. The acquired data, which are not yet published, show that Pt nanoparticles are indeed formed (Figure 41). It was also possible to determine the required temperature for the formation of the particles.

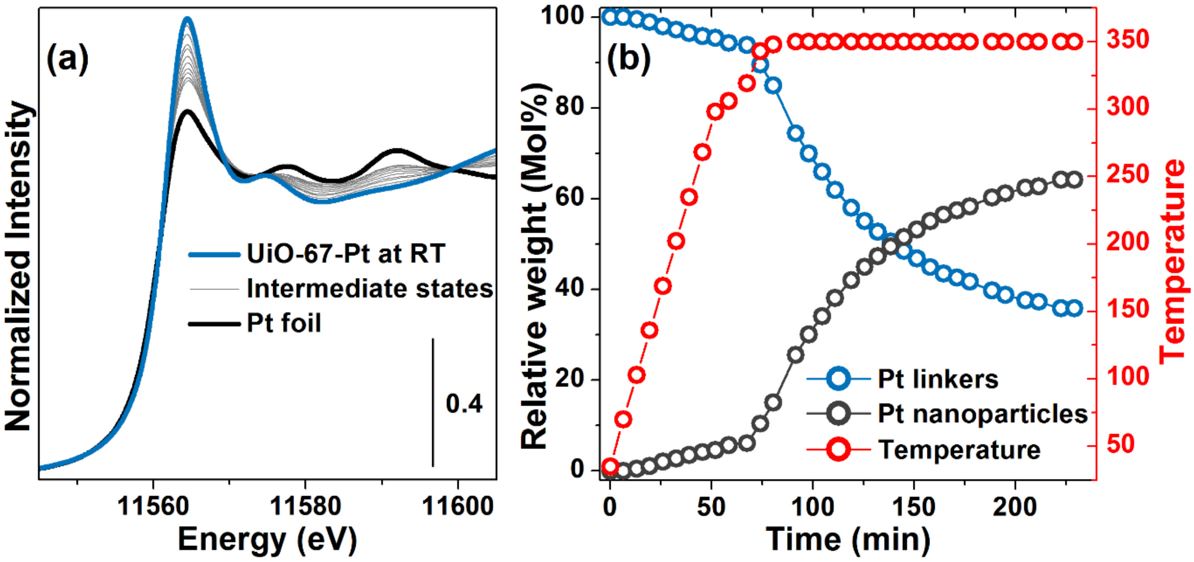

Figure 41. (a) Pt L_3-edge XANES spectra collected while heating UiO-67-bpy($PtCl_2$) to 350 °C in 10% H_2/He flux, together with the spectrum of Pt foil. (b) Linear combination analysis of the intermediate spectra from panel (a) performed using MOF and Pt foil spectra at RT as references.

The results indicate that H_2 was unavailable to Pt during the measurements reported in **paper IV**, at least not enough to cause reduction of Pt. There are several reasons why this could occur. The sample MOFs could have lost porosity due to the mechanical pressure when the sample pellet was prepared. Experimental errors are also a possibility, e.g. faulty gas mixture or errors arising from the experimental setup. The H_2 concentration might have been too low for nanoparticles to form during the time frame of the measurement. The crystallinity of the pellets that were measured could not be verified at the time of measurement due to lack of facilities, but in-house experiments indicate that UiO-67-bpy($PtCl_2$) decompose at mechanical pressure above 50 MPa. Given the high sensitivity of XAS to detect nanoparticle formation, it seems somewhat unlikely that a moderate mechanical pressure could lead to a completely dense phase.

Nevertheless, the thermally induced dissociation of Pt - Cl bonds pose an interesting opportunity to obtain Pt atoms with coordination vacancies, possibly available for further functionalization.

3.3.4 Reactivity of Pt in UiO-67: Ligand exchange

UiO-67-bpy($PtCl_2$) was also suspended as powder in solutions of toluene-3,4-dithiol (H_2tdt) in 2-propanol, and Br_2 in 2-propanol and octane (Figure 42a). The reactions were also performed on the linker $PtCl_2$(H_2bpydc) in DMSO solution (reaction with Br_2) and as reported for H_2tdt.[129]

SC-XRD and ^{1}H-NMR confirm that full conversion to the expected products, (H_2bpydc)PtBr$_4$ and (H_2bpydc)Pt(tdt), were achieved in the pure linker reactions. Full characterization data can be found in **paper IV**.

EXAFS analysis on the spectra acquired on the MOFs clearly show that Pt sites have reacted to form the same complexes in the MOFs (Figure 42b). In the brominated sample, both the amplitude and phase of the EXAFS signal had changed dramatically. In the thiol-exchanged sample, only a small phase shift was observed, presumably due to the similarity of the coordination environment around Pt: Cl and S atoms have similar X-ray scattering power, and their bond lengths with Pt are similar. It is also likely that full conversion was not achieved in the MOF sample, as the color was turquoise rather than the expected blue. EXAFS refinements including the imaginary part of the spectrum provide further evidence for Pt – S bond formation, as discussed in **paper IV**. The contribution from Pt – N interactions were unchanged in all experiments. These results clearly show that even molecules that approach the pore window size of UiO-67 (like H_2tdt) have the ability to diffuse throughout the crystal, albeit slowly.

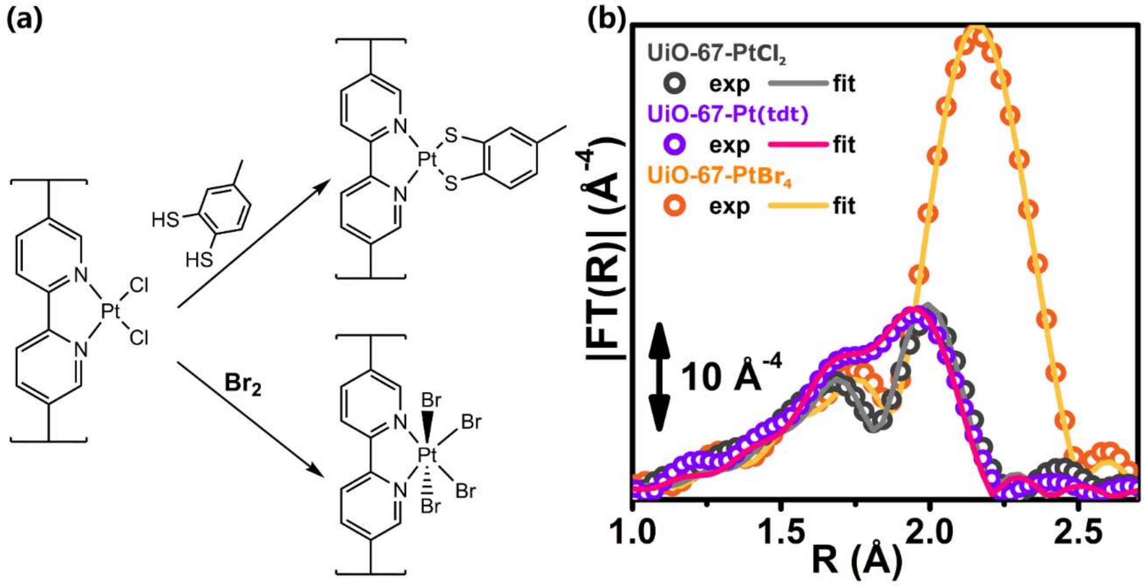

Figure 42. **(a)** The reactions discussed in this section, ligand exchange with H_2tdt and oxidative addition of Br_2 to Pt in UiO-67-bpy(PtCl$_2$). **(b)** Moduli of the Fourier transformed Pt L_3-edge spectra of UiO-67-bpy(PtCl$_2$) before (black) and after reaction with H_2tdt (violet) and Br_2 (orange). Experimental values are shown as open symbols, and corresponding best fit as solid lines of similar color.

3.3.5 Beyond paper IV: Postsynthetic linker exchange in UiO-67

Post synthetic linker exchange (PSE) has been used to obtain UiO-66 type MOFs with linkers which have not been reported to form MOFs by conventional synthesis.[41,130] In an attempt to obtain structural evidence for PSE by SC-XRD, single crystals of UiO-67 were submerged in a DMF solution of $PtCl_2(H_2bpydc)$. After 2 weeks the crystals had changed from colorless to weakly yellow, and a SC-XRD measurement was performed. The resulting structure refinement revealed a barely detectable amount of incorporated Pt at the same site as in UiO-67-bpy($PtCl_2$). However, the incorporation of Pt on the expected site could only be observed by inspection of the Fourier difference maps (Figure 43a-b). The crystals were therefore put back into the solution for another 6 months, after which another measurement was performed. At this point, the crystals had gained a more pronounced yellow color, and the structure refinement showed a substantial incorporation of Pt (Figure 43c), refined to about 4 % with respect to Zr. Although the experiments show incorporation of the PSE linker in the lattice, it is not determined if these have undergone exchange with already coordinated linkers or if they simply coordinate to vacant linker sites. A summary of the data collection and structure refinement details can be found in appendix A2, Table 10 on page 100.

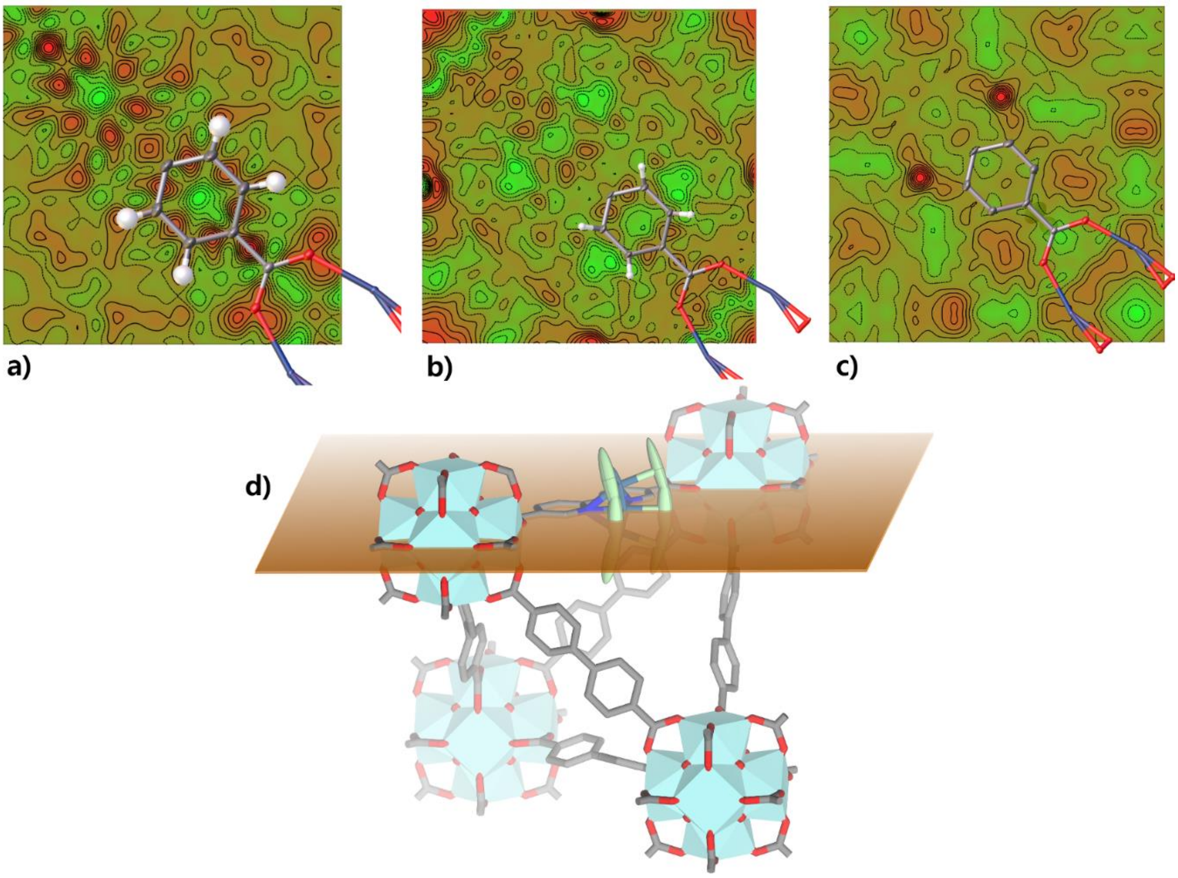

Figure 43. Difference Fourier electron density maps of a) UiO-67 before PSE. b) the sample measured after 2 weeks in PSE solution, and c) after 6 months. d) Crystal structure, showing the plane of intersection for the Fourier map. The magnitude curves of the difference map are not to scale, but relative for each sample.

3.3.6 Synthesis and structure of UiO-67-bpy(Cu)

UiO-67-bpy(Cu) was obtained by postsynthetic metalation of UiO-67 with 10 % H_2bpydc linkers with a solution of $CuCl_2·2H_2O$ in 2-propanol. The other synthesis strategies used in **paper II**, were also attempted, but the one pot synthesis gave too variable results and no suitable precursor was found for a pre-made linker synthesis. Reactions of $CuCl_2·2H_2O$ and H_2bpydc in DMF only gave a dimeric product.[131]

The comparison between UiO-67-bpy(Cu) MOFs and well-defined molecular Cu-bipyridine complexes is an important step to assess the success of the PSF process, and to gather information on the coordination environment and oxidation state of Cu-sites in the as-prepared samples. XAS spectra of the MOF and a crystalline reference compound (4,4'-di-tert-butyl-2,2'-bipyridine dichlorocopper(II), abbreviated $CuCl_2(^t$Bu-bpy)) were compared. This reference was chosen because of the difficulty to synthesize monomeric dichloride Cu complexes with 2,2'-bipyridine, dimethyl-2,2'-bipyridines, or H_2bpydc. A crystal structure was also obtained on $CuCl_2(^t$Bu-bpy), which provided excellent reference values for the EXAFS refinement (shown in Figure 44e).

The XAS experiments were carried out at RT in air, to verify the successful grafting of Cu in the UiO-67 framework and investigate the dominant local environment for Cu-sites in the as-prepared samples. Subsequently, XAS spectra were acquired while heating the sample from RT up to 250 °C in N_2 flow to monitor the evolution of the incorporated Cu species.

A first simple comparison of the XANES (Figure 44a) and EXAFS (Figure 44b) data collected on as-prepared UiO-67-bpy(Cu) in air (black) and on the $CuCl_2(^t$Bu-bpy) reference compound (green) clearly shows that the UiO-67-bpy(Cu) sample hosts a large majority of Cu(II) species (as the XANES spectra of Cu are sensitive to oxidation state). However, the local environment of Cu atoms in the two materials is significantly different. This case differs from what was observed for the functionalization of UiO-67 with Pt(II), where the local environment of Pt was the same in the $PtCl_2(H_2$bpydc) linker and in the functionalized MOF (section 3.3.1 on page 56). Indeed, the EXAFS data clearly shows reduced magnitude in the (1.5–2.1) Å region in UiO-67-bpy(Cu), suggesting the presence of only one Cl atom in the first coordination shell of the copper atoms (Figure 44c,d). Moreover, the loss of spectroscopic definition of the features of the XANES spectrum of UiO-67-bpy(Cu) (Figure 44a) suggest an increased heterogeneity of the Cu environment.

The XANES spectrum for the as-prepared MOF is characterized by the absence of any defined pre-edge/edge peaks, and by a rather intense white line feature at ~8996.6eV, typical of Cu(II) centres coordinated to water molecules and/or OH groups.[132] It was thus assumed that one Cl^- ligand had been substituted with an OH^- group in the first coordination shell of Cu, and the analysis was performed based on a DFT optimized [Cu(II)(bpydc)(OH)Cl] complex (Figure 44f). This new model takes into account the important differences observed in the EXAFS spectrum of the UiO-67-bpy(Cu) MOF with respect to that of the $CuCl_2(^tBu\text{-bpy})$ model compound. It is worth noting that it is almost impossible to distinguish coordination of $O(H_2O)$ and O(OH) ligands with EXAFS, due to the weak scattering amplitude of H. In the MOF, charge balance of the complex is not limited to 1st shell ligands of Cu, but can be achieved by non-coordinated anions in close proximity.

The [Cu(II)(bpydc)(OH)Cl] structure gave a satisfactorily fit to the EXAFS spectra for UiO-67-bpy(Cu), with good R-factor values and significantly more reliable Debye-Waller factors with respect to the configuration with two chlorine ligands.

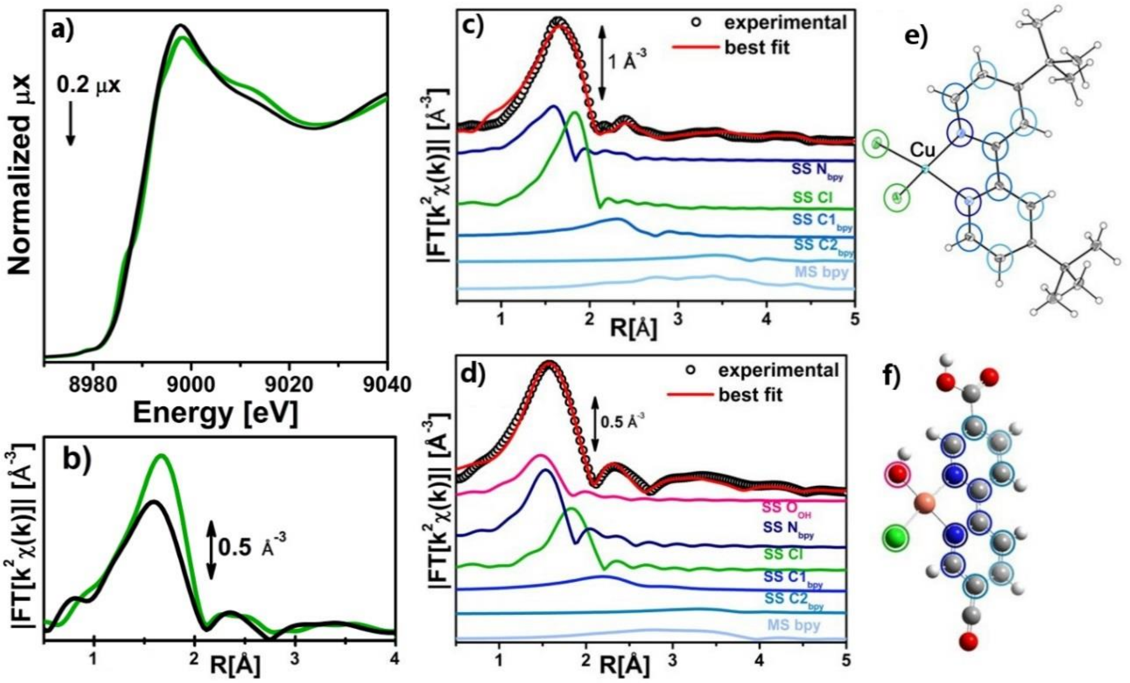

Figure 44. **a)** XANES and **b)** EXAFS modulus of $CuCl_2(^tBu\text{-bpy})$ (green) and UiO-67-bpy(Cu) (black). For $CuCl_2(^tBu\text{-bpy})$, **c)** and UiO-67-bpy(Cu) **d)**: Comparison between experimental (empty circles) and best fit (red line) of the EXAFS modulus, also showing the different paths. **e)** Crystal structure of $CuCl_2(^tBu\text{-bpy})$, the colored circles showing the different paths used in the EXAFS analysis. **f)** DFT optimized structure of the best fit for UiO-67-bpy(Cu).

3.3.7 Beyond paper V: Crystallographic characterization

Single crystals of UiO-67-bpy(Cu) were obtained by postsynthetic metalation, by suspending single crystals of UiO-67-bpy$_{0.2}$ in a solution of $CuCl_2 \cdot 2H_2O$ in 2-propanol for 24 hours at room temperature (see appendix A1, page 86 for a full description). In the refined crystal structure, Cu is clearly incorporated in the lattice. However, ligands of Cu could not be resolved. This excludes the presence of two Cl^- ligands in a well-defined conformation as observed in the platinum analogue, in agreement with the EXAFS results obtained on the powder sample of UiO-67-bpy(Cu). Although a well-defined diffraction pattern was obtained and good confidence factors were achieved during structure refinement, the ADP values of the structure were abnormally large. The distance between Cu and the linker was significantly shorter than expected (1.745(15) Å in the MOF compared to 2.011(2) Å and 2.032(2) Å in the isolated linker. Summary of the data collection and structure refinement details are found in appendix A2, Table 9 on page 99.

It has recently been shown that 100 % post synthetic incorporation of Cu in UiO-67-bpy causes a reduction of symmetry from $Fm\bar{3}m$ to $Pa\bar{3}$, due to the strain that is introduced when Cu causes the bpy ligand to bend out of its normally linear geometry.[124] In the partially functionalized UiO-67 reported herein, the bpydc ligand is bent in the same manner, causing a strain in the crystal. However, due to the low concentration of available bpy sites, no change in symmetry is observed. Instead, the structural change is observed as a random disorder compatible with the $Fm\bar{3}m$ space group, which explains the increased thermal factors. This can be visualized by superimposing the structures of the three possible ways a linker site can be occupied (Figure 45). The result is in agreement with EXAFS refinement in the previous chapter, concluding that at least one Cl ligand is lost during functionalization.

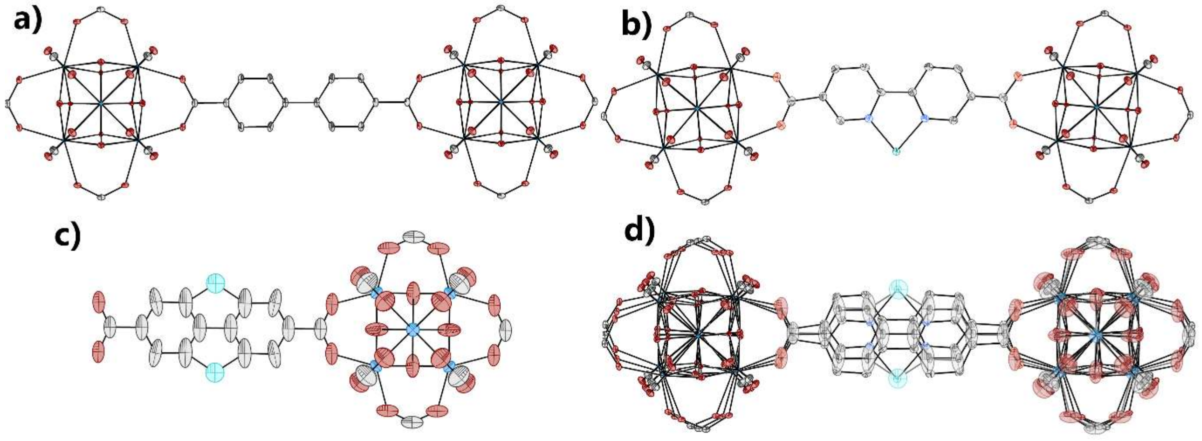

Figure 45. Vizualizing the disorder in the crystal structures of the mixed linker UiO-67-bpy(Cu) structure. **a)** Structure of UiO-67. **b)** Representations of two Zr$_6$ clusters bridged by a metalated H$_2$bpydc linker, inducing strain, **c)** Obtained structure of UiO-67-bpy(Cu). **d)** Superimposed images of a) b and c), explaining the apparently too short Cu – N bond lengths and the large ADP values

3.3.8 Reactivity of UiO-67-bpy(Cu)

Continuous heating of UiO-67-bpy(Cu) up to 250 °C was followed in situ with XAS. The spectral changes observed during thermal activation involve a clear decrease of the white line feature, accompanied by a significant shift of the absorption edge towards lower energies. At the end of the heating ramp, a shoulder starts to be distinguishable in the XANES edge-rising region at ca. 8983 eV, falling in an energy range typical for two or three-coordinated Cu(I) sites.[133] These evidences suggest a ligand loss process associated with the reduction of a significant percentage of the starting Cu(II) sites to Cu(I), as thermal treatment proceeds.[128]

The refined EXAFS spectra were consistent with the loss of a light atom ligand in the first coordination shell. The midrange region (R = 2.5 – 4.5 Å) arising mainly from scattering pathways of the linker remained unchanged, implying Cu was still chelated to the bpydc linkers. The obtained model strongly resembles previously reported Cu(I) sites in UiO-67-bpy characterized by SC-XRD by Gonzalez et. al.[124]

The material was exposed to a 40% CO in N$_2$ gas flow, at RT, while collecting XAS data. Intuitively, interaction of CO with [Cu(I)(bpydc)Cl] complexes is expected to result in [Cu(I)(bpydc)(CO)Cl], with the insertion of CO in the first coordination shell of Cu. A good EXAFS fit on a DFT optimized complex was obtained (Figure 46d-f). The chemisorption of CO was found to be reversible.

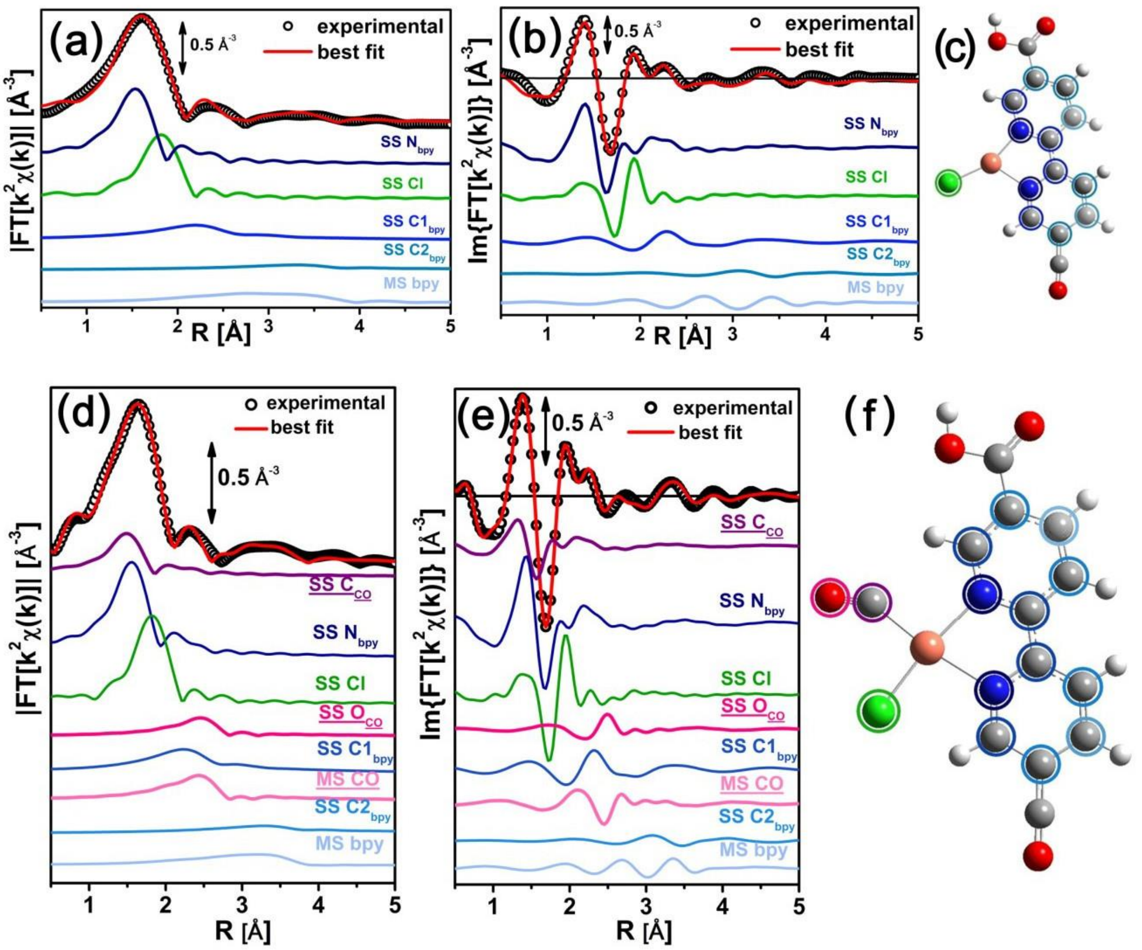

Figure 46. (a,b): k_2-weighted, phase uncorrected, modulus (a) and imaginary part (b) of the experimental and best fit FT EXAFS spectra for UiO-67-bpy(Cu) at RT after thermal treatment at 250 °C. The experimental data are shown as black dots and the best fit with a red solid line. The individual single scattering (SS) contributions and multiple scattering (MS) involving the atoms of the bpy unit are reported. Part (c): DFT-optimized structure used as starting point for the EXAFS fit. Atom color code: Cu: orange; O: red; N: blue; Cl: green, C: gray; H: white. Parts (d, e, f): as parts (a, b, c) for the thermally treated UiO-67-Cu after interaction with CO at RT.

The results herein show, with unprecedented accuracy, how Cu(II) species are incorporated in to bpy linkers in UiO-67 in a uniform manner. They are not, as previously assumed, forming the (N,N'-bpy)$CuCl_2$ species observed by Gonzalez et al.[124] However, they used anhydrous reagents in the metalation reaction, and could thus not obtain hydrated Cu species. The UiO-67-bpy(CuCl(OH/H_2O)) species reported herein readily auto-reduce to Cu(I) upon thermal activation, and are subsequently available for interaction with other substrates (e.g. CO). These insights into the formation and reactivity of bpy-Cu sites in MOFs represent important steps towards a MOF-based catalyst.

3.3.9 Summary

The results show the strength of EXAFS in determining the chemical state of elements incorporated in MOFs in small concentrations, as this information is difficult to obtain by other methods. Furthermore, the combination of EXAFS and diffraction experiments are able to determine the initial state of these MOFs to a high level of detail. This has allowed to verify and determine the effect of different functionalization procedures for metalated UiO-67 with Pt and Cu sites. It has been shown that these elements are grafted to framework-incorporated bipyridine linkers, and are available for reactions with gaseous and liquid-phase substrates. In the most investigated MOF, UiO-67-bpy($PtCl_2$), it was shown that Pt can undergo thermal reduction, ligand exchange with a dithiol and oxidative addition of bromine (Figure 47).

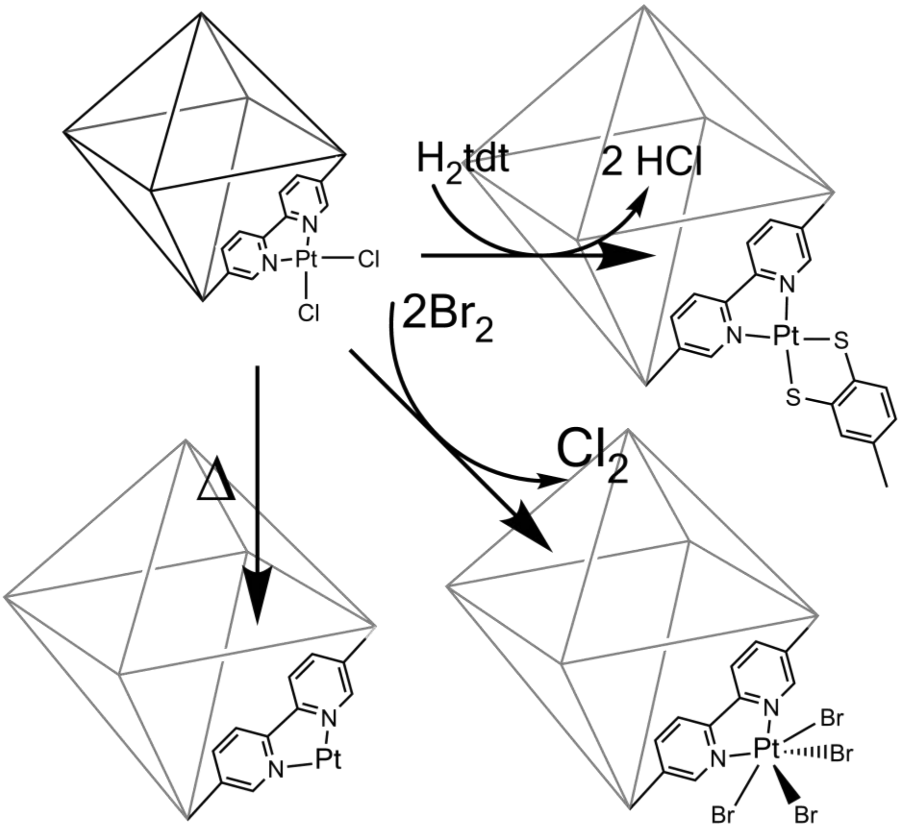

Figure 47. Schematic representation of the reactions performed on UiO-67-bpy($PtCl_2$): Ligand exchange, thermal reduction and oxidative addition.

For the Cu functionalized MOF, the initial sate was characterized, and the evolution of the Cu environment through thermal activation and interaction with CO was followed, without any evidence of metal clusters formation. In particular, XAS data for the as-prepared materials (collected at room temperature in air) are consistent with a majority of [Cu(II)(bpydc)(OH)Cl] species. Thermal activation under inert conditions promote a reduction effect of the original four-coordinated Cu(II) sites to three-coordinated Cu(I) species, [Cu(I)(bpydc)Cl], while preserving coordination to the UiO-67 framework by the chelating bpydc linkers.

These results lay the foundations for future operando studies aiming to characterize the reactivity of the grafted Pt and Cu-sites in more detail, in particular during catalytic reactions.

4 Conclusions and outlook

This work has involved many aspects of MOF chemistry; most importantly synthesis, structural studies, adsorption, and reactivity of framework-incorporated species. The main conclusions are grouped into method development and the three categories defined in the scope: structural studies, linker dependent properties and metal incorporation.

4.1 Method development

4.1.1 Synthesis

Several key variables in synthesis conditions of Zr-MOFs have been explored, with their effect on crystal size. The methods developed for single crystal synthesis of UiO-66 and UiO-67 were used to easily obtain single crystals of other Zr-MOFs. The key findings were:

- Using a modulator in high concentrations (up to 30 equivalents in respect to the linker) is necessary to obtain large single crystals. Modulators with pK_a values comparable to that of the linker provided best results.

- The concentration of precursors should be adjusted in order to approach the solubility limit of the linker.

- Before the onset of MOF crystallization, a clear solution must be obtained, and the reaction vessel needs to allow for evaporation of volatile byproducts and otherwise be free of nucleation sites on the surface.

4.2 Results

4.2.1 Crystallographic studies

- The crystal structures of several Zr-MOFs have been determined with an unprecedented degree of accuracy. Structural signatures of missing linker defects, have been identified, and seem to be universal in cluster based Zr-MOFs. Qualitative information was also obtained about the location and strength of adsorption sites.

- SC-XRD has been used to verify the efficiency of some postsynthetic metalation and postsynthetic linker exchange reactions in UiO-67.

4.2.2 Linker dependent properties of UiO-67 analogues

- Water stability of UiO-67 type MOFs can be increased by the inclusion of hydrophobic functional groups on the linker. There are strong indications that the same principle can be utilized to obtain water stable UiO-68 analogues.

- Incorporating aliphatic and aromatic functionality in UiO-67 was found to increase the heat of adsorption for methane at low pressures, and increase the volumetric uptake in respect to non-functionalized UiO-67 over a wide pressure range. However, due to this increased affinity, an increase of the working capacity could not be obtained.

- Cyclic water adsorption experiments have been performed on the newly developed UiO-67-binaphthyl, and the adsorption isotherms show a steep uptake at well-defined partial pressure, and hysteresis upon desorption.

4.2.3 Incorporation of Pt and Cu complexes

- Local structures of framework-incorporated Pt and Cu complexes in UiO-67 have been probed with EXAFS, on as-functionalized MOF and at activation and reaction conditions. The results show that such complexes can undergo reactions during functionalization, exemplified by reduction of $PtCl_4(H_2bpydc)$ and the loss of Cl^- ligands in UiO-67-bpy(Cu).

- Pt complexes in UiO-67 have been shown to be available for a range of reactions. Probing these reactions in situ has provided information on reaction conditions that promote the formation of potentially catalytically active sites such as Pt atoms with coordination vacancies or Pt nanoparticles.

- Results obtained from probing Cu complexes in situ lay the foundations for future studies aiming to characterize the redox behavior of the grafted Cu-sites, and subsequently catalytic reactions utilizing the rich redox chemistry of copper.

4.3 Outlook

First and foremost, the results obtained on the reactivity of lattice incorporated Pt and Cu should be used to further investigate their reactivity, and to develop working catalysts for suitable reactions such as e.g. C – H activation or CO_2 utilization. The nature of the unsaturated Pt sites discussed in **paper IV** should in particular be investigated in greater detail.

In both catalysis and adsorption, the use of mixed linker MOFs is largely unexplored. Co-functionality in catalytically functionalized MOFs such as pore size alterations or pore surface functionalization could potentially lead to heterogeneous catalysts of unprecedented degree of sophistication, and provide valuable mechanistic insight. Functional groups in vicinity of catalytic sites inside the MOF could play a role in tuning the catalytic activity and/or selectivity.

Adsorption on mixed linker MOFs could potentially lead to tailored materials for very specific applications in e.g. industrial separations. As an extension of the work presented in **paper III**, the water adsorption condensation threshold in UiO-67-BN could potentially be altered by a small percentage of hydrophilic linkers. In the development of new, mixed linker MOFs, development of dedicated computational tools would be very beneficial.

There are also further structural investigations to be performed. The termination of defects, as discussed in **paper I**, is not fully understood, as monoxarboxylates coordinated to the Zr cluster could be bonded to one or two Zr ions. It is also unclear whether the Zr_6 cluster is strained when not harboring defects. A combination of diffraction, composition analysis and computations could provide insight on this.

The mechanism of structural collapse induced by the removal of water from the MOFs' pores should be probed by computationally assisted EXAFS and diffuse scattering analysis.

Many of the structures reported herein contain linkers that are in steric conflict with each other. Although these conflicts will determine the local structure, no periodic order is observed. Such correlated disorder could be found in UiO-67-binaphthyl and maybe provide an explanation for the abrupt water uptake it displays.

References

(1) Batten, S. R.; Champness, N. R.; Chen, X.-M.; Garcia-Martinez, J.; Kitagawa, S.; Ohrstrom, L.; O'Keeffe, M.; Suh, M. P.; Reedijk, J., Terminology of metal-organic frameworks and coordination polymers (IUPAC recommendations 2013). *Pure Appl. Chem.* **2013**, *85*, 1715-1724.

(2) Lu, W.; Wei, Z.; Gu, Z.-Y.; Liu, T.-F.; Park, J.; Park, J.; Tian, J.; Zhang, M.; Zhang, Q.; Gentle III, T.; Bosch, M.; Zhou, H.-C., Tuning the structure and function of metal-organic frameworks via linker design. *Chem. Soc. Rev.* **2014**, *43*, 5561-5593.

(3) Furukawa, H.; Cordova, K. E.; O'Keeffe, M.; Yaghi, O. M., The Chemistry and Applications of Metal-Organic Frameworks. *Science* **2013**, *341*.

(4) Park, K. S.; Ni, Z.; Côté, A. P.; Choi, J. Y.; Huang, R.; Uribe-Romo, F. J.; Chae, H. K.; O'Keeffe, M.; Yaghi, O. M., Exceptional chemical and thermal stability of zeolitic imidazolate frameworks. *Proc. Natl. Acad. Sci. USA* **2006**, *103*, 10186-10191.

(5) Huang, X.-C.; Lin, Y.-Y.; Zhang, J.-P.; Chen, X.-M., Ligand-Directed Strategy for Zeolite-Type Metal–Organic Frameworks: Zinc(II) Imidazolates with Unusual Zeolitic Topologies. *Angew. Chem. Int. Ed.* **2006**, *45*, 1557-1559.

(6) Eddaoudi, M.; Sava, D. F.; Eubank, J. F.; Adil, K.; Guillerm, V., Zeolite-like metal-organic frameworks (ZMOFs): design, synthesis, and properties. *Chem. Soc. Rev.* **2015**, *44*, 228-249.

(7) Ma, L.; Abney, C.; Lin, W., Enantioselective catalysis with homochiral metal-organic frameworks. *Chem. Soc. Rev.* **2009**, *38*, 1248-1256.

(8) Tsuruoka, T.; Furukawa, S.; Takashima, Y.; Yoshida, K.; Isoda, S.; Kitagawa, S., Nanoporous nanorods fabricated by coordination modulation and oriented attachment growth. *Angew. Chem. Int. Ed.* **2009**, *48*, 4739-4743.

(9) O'Keeffe, M.; Yaghi, O. M., Deconstructing the crystal structures of metal-organic frameworks and related materials into their underlying nets. *Chem. rev.* **2012**, *112*, 675-702.

(10) Yaghi, O. M.; O'Keeffe, M.; Ockwig, N. W.; Chae, H. K.; Eddaoudi, M.; Kim, J., Reticular synthesis and the design of new materials. *Nature* **2003**, *423*, 705-714.

(11) Cavka, J. H.; Jakobsen, S.; Olsbye, U.; Guillou, N.; Lamberti, C.; Bordiga, S.; Lillerud, K. P., A new zirconium inorganic building brick forming metal organic frameworks with exceptional stability. *J Am Chem Soc* **2008**, *130*, 13850-13851.

(12) Kandiah, M.; Nilsen, M. H.; Usseglio, S.; Jakobsen, S.; Olsbye, U.; Tilset, M.; Larabi, C.; Quadrelli, E. A.; Bonino, F.; Lillerud, K. P., Synthesis and Stability of Tagged UiO-66 Zr-MOFs. *Chem. Mater.* **2010**, *22*, 6632-6640.

(13) Liu, J.; Thallapally, P. K.; McGrail, B. P.; Brown, D. R.; Liu, J., Progress in adsorption-based CO2 capture by metal-organic frameworks. *Chem. Soc. Rev.* **2012**, *41*, 2308-2322.

(14) Sumida, K.; Rogow, D. L.; Mason, J. A.; McDonald, T. M.; Bloch, E. D.; Herm, Z. R.; Bae, T.-H.; Long, J. R., Carbon Dioxide Capture in Metal-Organic Frameworks. *Chem. Rev.* **2012**, *112*, 724-781.

(15) Cavka, J. H.; Jakobsen, S.; Olsbye, U.; Guillou, N.; Lamberti, C.; Bordiga, S.; Lillerud, K. P., A New Zirconium Inorganic Building Brick Forming Metal Organic Frameworks with Exceptional Stability. *J. Am. Chem. Soc.* **2008**, *130*, 13850-13851.

(16) Tan, K.; Nijem, N.; Canepa, P.; Gong, Q.; Li, J.; Thonhauser, T.; Chabal, Y. J., Stability and Hydrolyzation of Metal Organic Frameworks with Paddle-Wheel SBUs upon Hydration. *Chem. Mater.* **2012**, *24*, 3153-3167.

(17) DeCoste, J. B.; Peterson, G. W.; Jasuja, H.; Glover, T. G.; Huang, Y.-g.; Walton, K. S., Stability and degradation mechanisms of metal-organic frameworks containing the Zr6O4(OH)4 secondary building unit. *J. Mater. Chem. A* **2013**, *1*, 5642-5650.

(18) Bai, Y.; Dou, Y.; Xie, L.-H.; Rutledge, W.; Li, J.-R.; Zhou, H.-C., Zr-based metal-organic frameworks: design, synthesis, structure, and applications. *Chem. Soc. Rev.* **2016**.

(19) Kim, M.; Cohen, S. M., Discovery, Development, and Functionalization of Zr(IV)-Based Metal-Organic Frameworks. *CrystEngComm* **2012**, *14*, 4096-4104.

(20) Kickelbick, G.; Schubert, U., Oxozirconium methacrylate clusters. Zr6(OH)4O4(OMc)12 and Zr4O2(OMc)12 (OMc = methacrylate). *Chem. Ber./Recl.* **1997**, *130*, 473-477.

(21) Shearer, G. C.; Forselv, S.; Chavan, S.; Bordiga, S.; Mathisen, K.; Bjorgen, M.; Svelle, S.; Lillerud, K. P., In Situ Infrared Spectroscopic and Gravimetric Characterisation of the Solvent Removal and Dehydroxylation of the Metal Organic Frameworks UiO-66 and UiO-67. *Top. Catal.* **2013**, *56*, 770-782.

(22) Valenzano, L.; Civalleri, B.; Chavan, S.; Bordiga, S.; Nilsen, M. H.; Jakobsen, S.; Lillerud, K. P.; Lamberti, C., Disclosing the Complex Structure of UiO-66 Metal Organic Framework: A Synergic Combination of Experiment and Theory. *Chem. Mat.* **2011**, *23*, 1700-1718.

(23) Furukawa, H.; Gandara, F.; Zhang, Y.-B.; Jiang, J.; Queen, W. L.; Hudson, M. R.; Yaghi, O. M., Water Adsorption in Porous Metal-Organic Frameworks and Related Materials. *J. Am. Chem. Soc.* **2014**, *136*, 4369-4381.

(24) Liang, W.; Chevreau, H.; Ragon, F.; Southon, P. D.; Peterson, V. K.; D'Alessandro, D. M., Tuning pore size in a zirconium-tricarboxylate metal-organic framework. *CrystEngComm* **2014**, *16*, 6530-6533.

(25) Reinsch, H.; Bueken, B.; Vermoortele, F.; Stassen, I.; Lieb, A.; Lillerud, K.-P.; De Vos, D., Green synthesis of zirconium-MOFs. *CrystEngComm* **2015**, *17*, 4070-4074.

(26) Reinsch, H.; Stassen, I.; Bueken, B.; Lieb, A.; Ameloot, R.; De Vos, D., First examples of aliphatic zirconium MOFs and the influence of inorganic anions on their crystal structures. *CrystEngComm* **2015**, *17*, 331-337.

(27) Wang, C.; Xie, Z.; deKrafft, K. E.; Lin, W., Doping Metal-Organic Frameworks for Water Oxidation, Carbon Dioxide Reduction, and Organic Photocatalysis. *J. Am. Chem. Soc.* **2011**, *133*, 13445-13454.

(28) Feng, D.; Gu, Z.-Y.; Li, J.-R.; Jiang, H.-L.; Wei, Z.; Zhou, H.-C., Zirconium-Metalloporphyrin PCN-222: Mesoporous Metal–Organic Frameworks with Ultrahigh Stability as Biomimetic Catalysts. *Angew. Chem. Int. Ed.* **2012**, *51*, 10307-10310.

(29) Gomez-Gualdron, D. A.; Gutov, O. V.; Krungleviciute, V.; Borah, B.; Mondloch, J. E.; Hupp, J. T.; Yildirim, T.; Farha, O. K.; Snurr, R. Q., Computational Design of Metal–Organic Frameworks Based on Stable Zirconium Building Units for Storage and Delivery of Methane. *Chem. Mater.* **2014**, *26*, 5632-5639.

(30) Morris, W.; Volosskiy, B.; Demir, S.; Gándara, F.; McGrier, P. L.; Furukawa, H.; Cascio, D.; Stoddart, J. F.; Yaghi, O. M., Synthesis, Structure, and Metalation of Two New Highly Porous Zirconium Metal–Organic Frameworks. *Inorg. Chem.* **2012**, *51*, 6443-6445.

(31) Schaate, A.; Roy, P.; Preuße, T.; Lohmeier, S. J.; Godt, A.; Behrens, P., Porous Interpenetrated Zirconium–Organic Frameworks (PIZOFs): A Chemically Versatile Family of Metal–Organic Frameworks. *Chem.-Eur. J.* **2011**, *17*, 9320-9325.

(32) Wang, C.; deKrafft, K. E.; Lin, W., Pt Nanoparticles@Photoactive Metal-Organic Frameworks: Efficient Hydrogen Evolution via Synergistic Photoexcitation and Electron Injection. *J. Am. Chem. Soc.* **2012**, *134*, 7211-7214.

(33) Guillerm, V.; Ragon, F.; Dan-Hardi, M.; Devic, T.; Vishnuvarthan, M.; Campo, B.; Vimont, A.; Clet, G.; Yang, Q.; Maurin, G.; Férey, G.; Vittadini, A.; Gross, S.; Serre, C., A Series of Isoreticular, Highly Stable, Porous Zirconium Oxide Based Metal–Organic Frameworks. *Angew. Chem. Int. Ed.* **2012**, *51*, 9267-9271.

(34) Ling, S.; Slater, B., Dynamic Acidity in Defective UiO-66. *arXiv preprint arXiv:1512.04085* **2015**.

(35) Shearer, G. C.; Chavan, S.; Ethiraj, J.; Vitillo, J. G.; Svelle, S.; Olsbye, U.; Lamberti, C.; Bordiga, S.; Lillerud, K. P., Tuned to Perfection: Ironing Out the Defects in Metal-Organic Framework UiO-66. *Chem. Mater.* **2014**, *26*, 4068-4071.

(36) Ghosh, P.; Colon, Y. J.; Snurr, R. Q., Water adsorption in UiO-66: the importance of defects. *Chem. Commun.* **2014**, *50*, 11329-11331.

(37) Wu, H.; Chua, Y. S.; Krungleviciute, V.; Tyagi, M.; Chen, P.; Yildirim, T.; Zhou, W., Unusual and Highly Tunable Missing-Linker Defects in Zirconium Metal-Organic Framework UiO-66 and Their Important Effects on Gas Adsorption. *J. Am. Chem. Soc.* **2013**, *135*, 10525-10532.

(38) Cliffe, M. J.; Funnell, N. P.; Goodwin, A. L.; Wan, W.; Zou, X.; Chater, P. A.; Kleppe, A. K.; Wilhelm, H.; Tucker, M. G.; Coudert, F.-X., Correlated defect nanoregions in a metal-organic framework. *Nat. Commun.* **2014**, *5*, 4176.

(39) Shearer, G. C. On the Defect Chemistry of the Metal-Organic Framework Compound UiO-66. Ph.D. Thesis, University of Oslo, 2016.

(40) Deng, H.; Doonan, C. J.; Furukawa, H.; Ferreira, R. B.; Towne, J.; Knobler, C. B.; Wang, B.; Yaghi, O. M., Multiple Functional Groups of Varying Ratios in Metal-Organic Frameworks. *Science* **2010**, *327*, 846-850.

(41) Kim, M.; Cahill, J. F.; Su, Y.; Prather, K. A.; Cohen, S. M., Postsynthetic ligand exchange as a route to functionalization of 'inert' metal–organic frameworks. *Chem. Sci.* **2012**, *3*, 126.

(42) Cohen, S. M., Postsynthetic methods for the functionalization of metal-organic frameworks. *Chem. rev.* **2012**, *112*, 970-1000.

(43) Ethiraj, J.; Albanese, E.; Civalleri, B.; Vitillo, J. G.; Bonino, F.; Chavan, S.; Shearer, G. C.; Lillerud, K. P.; Bordiga, S., Carbon Dioxide Adsorption in Amine-Functionalized Mixed-Ligand Metal–Organic Frameworks of UiO-66 Topology. *ChemSusChem* **2014**, *7*, 3382-3388.

(44) Kleist, W.; Jutz, F.; Maciejewski, M.; Baiker, A., Mixed-Linker Metal-Organic Frameworks as Catalysts for the Synthesis of Propylene Carbonate from Propylene Oxide and CO2. *Eur. J. Inorg. Chem.* **2009**, *2009*, 3552-3561.

(45) Chavan, S. M.; Shearer, G. C.; Svelle, S.; Olsbye, U.; Bonino, F.; Ethiraj, J.; Lillerud, K. P.; Bordiga, S., Synthesis and Characterization of Amine-Functionalized Mixed-Ligand Metal–Organic Frameworks of UiO-66 Topology. *Inorg. Chem.* **2014**, *53*, 9509-9515.

(46) He, Y.; Zhou, W.; Qian, G.; Chen, B., Methane storage in metal-organic frameworks. *Chem. Soc. Rev.* **2014**, *43*, 5657-5678.

(47) Ma, S.; Sun, D.; Simmons, J. M.; Collier, C. D.; Yuan, D.; Zhou, H.-C., Metal-Organic Framework from an Anthracene Derivative Containing Nanoscopic Cages Exhibiting High Methane Uptake. *J. Am. Chem. Soc.* **2008**, *130*, 1012-1016.

(48) Düren, T.; Sarkisov, L.; Yaghi, O. M.; Snurr, R. Q., Design of New Materials for Methane Storage. *Langmuir* **2004**, *20*, 2683-2689.

(49) Sumida, K.; Rogow, D. L.; Mason, J. A.; McDonald, T. M.; Bloch, E. D.; Herm, Z. R.; Bae, T. H.; Long, J. R., Carbon dioxide capture in metal-organic frameworks. *Chem. rev.* **2012**, *112*, 724-781.

(50) Burtch, N. C.; Jasuja, H.; Walton, K. S., Water Stability and Adsorption in Metal–Organic Frameworks. *Chem. Rev.* **2014**, *114*, 10575-10612.

(51) Barea, E.; Montoro, C.; Navarro, J. A. R., Toxic gas removal - metal-organic frameworks for the capture and degradation of toxic gases and vapours. *Chem. Soc. Rev.* **2014**, *43*, 5419-5430.

(52) Li, J. R.; Sculley, J.; Zhou, H. C., Metal-organic frameworks for separations. *Chem. rev.* **2012**, *112*, 869-932.

(53) Li, J.-R.; Kuppler, R. J.; Zhou, H.-C., Selective gas adsorption and separation in metal-organic frameworks. *Chem. Soc. Rev.* **2009**, *38*, 1477-1504.

(54) Silva, P.; Vilela, S. M. F.; Tome, J. P. C.; Almeida Paz, F. A., Multifunctional metal-organic frameworks: from academia to industrial applications. *Chem. Soc. Rev.* **2015**, *44*, 6774-6803.

(55) Gascon, J.; Corma, A.; Kapteijn, F.; Llabrés i Xamena, F. X., Metal Organic Framework Catalysis: Quo vadis? *ACS Catal.* **2014**, *4*, 361-378.

(56) Vermoortele, F.; Bueken, B.; Le Bars, G.; Van de Voorde, B.; Vandichel, M.; Houthoofd, K.; Vimont, A.; Daturi, M.; Waroquier, M.; Van Speybroeck, V.; Kirschhock, C.; De Vos, D. E., Synthesis Modulation as a Tool To Increase the Catalytic Activity of Metal-Organic Frameworks: The Unique Case of UiO-66(Zr). *J. Am. Chem. Soc.* **2013**, *135*, 11465-11468.

(57) Vermoortele, F.; Vandichel, M.; Van de Voorde, B.; Ameloot, R.; Waroquier, M.; Van Speybroeck, V.; De Vos, D. E., Electronic Effects of Linker Substitution on Lewis Acid Catalysis with Metal–Organic Frameworks. *Angew. Chem. Int. Ed.* **2012**, *51*, 4887-4890.

(58) Liu, J.; Chen, L.; Cui, H.; Zhang, J.; Zhang, L.; Su, C.-Y., Applications of metal-organic frameworks in heterogeneous supramolecular catalysis. *Chem. Soc. Rev.* **2014**, *43*, 6011-6061.

(59) Lu, G.; Li, S.; Guo, Z.; Farha, O. K.; Hauser, B. G.; Qi, X.; Wang, Y.; Wang, X.; Han, S.; Liu, X.; DuChene, J. S.; Zhang, H.; Zhang, Q.; Chen, X.; Ma, J.; Loo, S. C. J.; Wei, W. D.; Yang, Y.; Hupp, J. T.; Huo, F., Imparting functionality to a metal–organic framework material by controlled nanoparticle encapsulation. *Nat Chem* **2012**, *4*, 310-316.

(60) Liu, H.; Liu, Y.; Li, Y.; Tang, Z.; Jiang, H., Metal−Organic Framework Supported Gold Nanoparticles as a Highly Active Heterogeneous Catalyst for Aerobic Oxidation of Alcohols. *J. Phys. Chem. C* **2010**, *114*, 13362-13369.

(61) Lykourinou, V.; Chen, Y.; Wang, X.-S.; Meng, L.; Hoang, T.; Ming, L.-J.; Musselman, R. L.; Ma, S., Immobilization of MP-11 into a Mesoporous Metal–Organic Framework, MP-11@mesoMOF: A New Platform for Enzymatic Catalysis. *J. Am. Chem. Soc.* **2011**, *133*, 10382-10385.

(62) Lee, J. Y.; Farha, O. K.; Roberts, J.; Scheidt, K. A.; Nguyen, S. B. T.; Hupp, J. T., Metal-organic framework materials as catalysts. *Chem. Soc. Rev.* **2009**, *38*, 1450-1459.

(63) Wang, C.; Wang, J.-L.; Lin, W., Elucidating Molecular Iridium Water Oxidation Catalysts Using Metal-Organic Frameworks: A Comprehensive Structural, Catalytic, Spectroscopic, and Kinetic Study. *J. Am. Chem. Soc.* **2012**, *134*, 19895-19908.

(64) Fei, H.; Cohen, S. M., A robust, catalytic metal-organic framework with open 2,2'-bipyridine sites. *Chem. Commun.* **2014**, *50*, 4810-4812.

(65) Hu, Z.; Peng, Y.; Kang, Z.; Qian, Y.; Zhao, D., A Modulated Hydrothermal (MHT) Approach for the Facile Synthesis of UiO-66-Type MOFs. *Inorg. Chem.* **2015**, *54*, 4862-4868.

(66) Taddei, M.; Steitz, D. A.; van Bokhoven, J. A.; Ranocchiari, M., Continuous-Flow Microwave Synthesis of Metal–Organic Frameworks: A Highly Efficient Method for Large-Scale Production. *Chem.-Eur. J.* **2016**, *22*, 3245-3249.

(67) Rubio-Martinez, M.; Batten, M. P.; Polyzos, A.; Carey, K.-C.; Mardel, J. I.; Lim, K.-S.; Hill, M. R., Versatile, High Quality and Scalable Continuous Flow Production of Metal-Organic Frameworks. *Sci. Rep.* **2014**, *4*, 5443.

(68) Uzarevic, K.; Wang, T. C.; Moon, S.-Y.; Fidelli, A. M.; Hupp, J. T.; Farha, O. K.; Friscic, T., Mechanochemical and solvent-free assembly of zirconium-based metal-organic frameworks. *Chem. Commun.* **2016**, *52*, 2133-2136.

(69) Schaate, A.; Roy, P.; Godt, A.; Lippke, J.; Waltz, F.; Wiebcke, M.; Behrens, P., Modulated synthesis of Zr-based metal-organic frameworks: from nano to single crystals. *Chem.-Eur. J.* **2011**, *17*, 6643-6651.

(70) Trickett, C. A.; Gagnon, K. J.; Lee, S.; Gándara, F.; Bürgi, H.-B.; Yaghi, O. M., Definitive Molecular Level Characterization of Defects in UiO-66 Crystals. *Angew. Chem. Int. Ed.* **2015**, *54*, 11162-11167.

(71) Marshall, R. J.; Hobday, C. L.; Murphie, C. F.; Griffin, S. L.; Morrison, C. A.; Moggach, S. A.; Forgan, R. S., Amino acids as highly efficient modulators for single crystals of zirconium and hafnium metal-organic frameworks. *J. Mater. Chem. A* **2016**.

(72) Wiersum, A. D.; Soubeyrand-Lenoir, E.; Yang, Q.; Moulin, B.; Guillerm, V.; Yahia, M. B.; Bourrelly, S.; Vimont, A.; Miller, S.; Vagner, C.; Daturi, M.; Clet, G.; Serre, C.; Maurin, G.; Llewellyn, P. L., An Evaluation of UiO-66 for Gas-Based Applications. *Chem. Asian J.* **2011**, *6*, 3270-3280.

(73) Muzart, J., N,N-Dimethylformamide: much more than a solvent. *Tetrahedron* **2009**, *65*, 8313-8323.

(74) Wißmann, G.; Schaate, A.; Lilienthal, S.; Bremer, I.; Schneider, A. M.; Behrens, P., Modulated synthesis of Zr-fumarate MOF. *Microporous Mesoporous Mater.* **2012**, *152*, 64-70.

(75) IUPAC *Compendium of Chemical Terminology, 2nd ed. (the "Gold Book")*; 2nd ed.; Blackwell Scientific Publications: Oxford, 1997.

(76) Als-Nielsen, J.; McMorrow, D. In *Elements of Modern X-ray Physics*; John Wiley & Sons, Inc.: 2011, pp 147-205.

(77) Sheldrick, G. M., A short history of SHELX. *Acta Crystallogr. Sect. A* **2008**, *64*, 112-122.

(78) Sheldrick, G., Crystal structure refinement with SHELXL. *Acta Crystallogr. Sect. C* **2015**, *71*, 3-8.

(79) Carrington, E. J.; Vitorica-Yrezabal, I. J.; Brammer, L., Crystallographic studies of gas sorption in metal-organic frameworks. *Acta Crystallogr. Sect. B* **2014**, *70*, 404-422.

(80) Gandara, F.; Bennett, T. D., Crystallography of metal-organic frameworks. *IUCrJ* **2014**, *1*, 563-570.

(81) Zhang, J.-P.; Liao, P.-Q.; Zhou, H.-L.; Lin, R.-B.; Chen, X.-M., Single-crystal X-ray diffraction studies on structural transformations of porous coordination polymers. *Chem. Soc. Rev.* **2014**, *43*, 5789-5814.

(82) Spek, A., PLATON SQUEEZE: a tool for the calculation of the disordered solvent contribution to the calculated structure factors. *Acta Crystallogr. Sect. C* **2015**, *71*, 9-18.

(83) Penner-Hahn, J. E. In *Comprehensive Coordination Chemistry II*; Meyer, J. A. M. J., Ed.; Pergamon: Oxford, 2003, pp 159-186.

(84) Borfecchia, E.; Gianolio, D.; Agostini, G.; Bordiga, S.; Lamberti, C. In *Metal Organic Frameworks as Heterogeneous Catalysts*; The Royal Society of Chemistry: 2013, pp 143-208.

(85) Koningsberger, D. C.; Mojet, B. L.; van Dorssen, G. E.; Ramaker, D. E., XAFS spectroscopy; fundamental principles and data analysis. *Top. Catal.*, *10*, 143-155.

(86) Bordiga, S.; Groppo, E.; Agostini, G.; van Bokhoven, J. A.; Lamberti, C., Reactivity of Surface Species in Heterogeneous Catalysts Probed by In Situ X-ray Absorption Techniques. *Chem. Rev.* **2013**, *113*, 1736-1850.

(87) Prestipino, C.; Regli, L.; Vitillo, J. G.; Bonino, F.; Damin, A.; Lamberti, C.; Zecchina, A.; Solari, P. L.; Kongshaug, K. O.; Bordiga, S., Local Structure of Framework Cu(II) in HKUST-1 Metallorganic Framework: Spectroscopic Characterization upon Activation and Interaction with Adsorbates. *Chem. Mater.* **2006**, *18*, 1337-1346.

(88) Carlson, S.; Clausen, M.; Gridneva, L.; Sommarin, B.; Svensson, C., XAFS experiments at beamline I811, MAX-lab synchrotron source, Sweden. *J. Synchrotron Rad.* **2006**, *13*, 359-364.

(89) Hannemann, S.; Casapu, M.; Grunwaldt, J.-D.; Haider, P.; Trussel, P.; Baiker, A.; Welter, E., A versatile in situ spectroscopic cell for fluorescence/transmission EXAFS and X-ray diffraction of heterogeneous catalysts in gas and liquid phase. *J. Synchrotron Rad.* **2007**, *14*, 345-354.

(90) Ravel, B.; Newville, M., ATHENA, ARTEMIS, HEPHAESTUS: data analysis for X-ray absorption spectroscopy using IFEFFIT. *J. Synchrotron Rad.* **2005**, *12*, 537-541.

(91) Øien, S.; Wragg, D.; Reinsch, H.; Svelle, S.; Bordiga, S.; Lamberti, C.; Lillerud, K. P., Detailed Structure Analysis of Atomic Positions and Defects in Zirconium Metal–Organic Frameworks. *Cryst. Growth Des.* **2014**, *14*, 5370-5372.

(92) Nickerl, G.; Leistner, M.; Helten, S.; Bon, V.; Senkovska, I.; Kaskel, S., Integration of accessible secondary metal sites into MOFs for H2S removal. *Inorg. Chem. Front.* **2014**, *1*, 325-330.

(93) Shearer, G. C.; Chavan, S.; Bordiga, S.; Svelle, S.; Olsbye, U.; Lillerud, K. P., Defect Engineering: Tuning the Porosity and Composition of the Metal–Organic Framework UiO-66 via Modulated Synthesis. *Chem. Mater.* **2016**, *28*, 3749-3761.

(94) Jiang, H.-L.; Feng, D.; Liu, T.-F.; Li, J.-R.; Zhou, H.-C., Pore Surface Engineering with Controlled Loadings of Functional Groups via Click Chemistry in Highly Stable Metal–Organic Frameworks. *J. Am. Chem. Soc.* **2012**, *134*, 14690-14693.

(95) Allen, F. H.; Kennard, O.; Watson, D. G.; Brammer, L.; Orpen, A. G.; Taylor, R., Tables of bond lengths determined by X-ray and neutron diffraction. Part 1. Bond lengths in organic compounds. *Journal of the Chemical Society, Perkin Transactions 2* **1987**, S1-S19.

(96) Katz, M. J.; Brown, Z. J.; Colon, Y. J.; Siu, P. W.; Scheidt, K. A.; Snurr, R. Q.; Hupp, J. T.; Farha, O. K., A facile synthesis of UiO-66, UiO-67 and their derivatives. *Chem. Commun.* **2013**, *49*, 9449-9451.

(97) Groom, C. R.; Bruno, I. J.; Lightfoot, M. P.; Ward, S. C., The Cambridge Structural Database. *Acta Crystallogr. Sect. B* **2016**, *72*, 171-179.

(98) Yeamin, R. M.; Hideaki, M.; Masayuki, K.; Michio, N.; Tadashi, T., Synthesis and Crystal Structure of a Novel Hexanuclear Zr(IV) Complex with Hydroxo and Carboxylato Bridging. *Bulletin of the Chemical Society of Japan* **1998**, *71*, 155-160.

(99) Piszczek, P.; Radtke, A.; Grodzicki, A.; Wojtczak, A.; Chojnacki, J., The new type of [Zr6(μ3-O)4(μ3-OH)4] cluster core: Crystal structure and spectral characterization of [Zr6O4(OH)4(OOCR)12] (R = But, C(CH3)2Et). *Polyhedron* **2007**, *26*, 679-685.

(100) Gao, Y.; Kogler, F. R.; Peterlik, H.; Schubert, U., Ring-opening metathesis polymerizations with norbornene carboxylate-substituted metal oxo clusters. *J. Mater. Chem.* **2006**, *16*, 3268-3276.

(101) Pan, L.; Heddy, R.; Li, J.; Zheng, C.; Huang, X.-Y.; Tang, X.; Kilpatrick, L., Synthesis and Structural Determination of a Hexanuclear Zirconium Glycine Compound Formed in Aqueous Solution. *Inorg. Chem.* **2008**, *47*, 5537-5539.

(102) Otero, A.; Fernández-Baeza, J.; Antiñolo, A.; Tejeda, J.; Lara-Sánchez, A.; Sánchez-Barba, L.; Fernández-López, M.; López-Solera, I., New Complexes of Zirconium(IV) and Hafnium(IV) with Heteroscorpionate Ligands and the Hydrolysis of Such Complexes To Give a Zirconium Cluster. *Inorg. Chem.* **2004**, *43*, 1350-1358.

(103) Kickelbick, G.; Wiede, P.; Schubert, U., Variations in capping the Zr6O4(OH)4 cluster core: X-ray structure analyses of [Zr6(OH)4O4(OOC–CH・CH2)10]2(μ-OOC–CH・CH2)4 and Zr6(OH)4O4(OOCR)12(PrOH) (R = Ph, CMe = CH2). *Inorganica Chimica Acta* **1999**, *284*, 1-7.

(104) Kogler, F. R.; Jupa, M.; Puchberger, M.; Schubert, U., Control of the ratio of functional and non-functional ligands in clusters of the type Zr6O4(OH)4(carboxylate)12 for their use as building blocks for inorganic-organic hybrid polymers. *J. Mater. Chem.* **2004**, *14*, 3133-3138.

(105) Pappas, I.; Fitzgerald, M.; Huang, X.-Y.; Li, J.; Pan, L., Thermally Resolved in Situ Dynamic Light Scattering Studies of Zirconium(IV) Complex Formation. *Cryst. Growth Des.* **2009**, *9*, 5213-5219.

(106) Dolomanov, O. V.; Bourhis, L. J.; Gildea, R. J.; Howard, J. A. K.; Puschmann, H., OLEX2: a complete structure solution, refinement and analysis program. *J. Appl. Crystallogr.* **2009**, *42*, 339-341.

(107) Hylland, K. T.; Øien-Ødegaard, S.; Lillerud, K. P.; Tilset, M., Efficient, Scalable Syntheses of Linker Molecules for Metal-Organic Frameworks. *Synlett* **2015**, *26*, 1480-1485.

(108) Mondloch, J. E.; Katz, M. J.; Planas, N.; Semrouni, D.; Gagliardi, L.; Hupp, J. T.; Farha, O. K., Are Zr6-based MOFs water stable? Linker hydrolysis vs. capillary-force-driven channel collapse. *Chem. Commun.* **2014**, *50*, 8944-8946.

(109) Huang, Y.; Qin, W.; Li, Z.; Li, Y., Enhanced stability and CO2 affinity of a UiO-66 type metal-organic framework decorated with dimethyl groups. *Dalton Trans.* **2012**, *41*, 9283-9285.

(110) Garibay, S. J.; Cohen, S. M., Isoreticular synthesis and modification of frameworks with the UiO-66 topology. *Chem. Commun.* **2010**, *46*, 7700-7702.

(111) Øien-Ødegaard, S.; Bouchevreau, B.; Hylland, K.; Wu, L.; Blom, R.; Grande, C.; Olsbye, U.; Tilset, M.; Lillerud, K. P., UiO-67-type Metal–Organic Frameworks with Enhanced Water Stability and Methane Adsorption Capacity. *Inorg. Chem.* **2016**, *55*, 1986-1991.

(112) Keen, D. A.; Goodwin, A. L., The crystallography of correlated disorder. *Nature* **2015**, *521*, 303-309.

(113) Brennan, J. K.; Bandosz, T. J.; Thomson, K. T.; Gubbins, K. E., Water in porous carbons. *Colloids Surf. A* **2001**, *187–188*, 539-568.

(114) Cmarik, G. E.; Kim, M.; Cohen, S. M.; Walton, K. S., Tuning the Adsorption Properties of UiO-66 via Ligand Functionalization. *Langmuir* **2012**, *28*, 15606-15613.

(115) Gutov, O. V.; Hevia, M. G.; Escudero-Adán, E. C.; Shafir, A., Metal–Organic Framework (MOF) Defects under Control: Insights into the Missing Linker Sites and Their Implication in the Reactivity of Zirconium-Based Frameworks. *Inorg. Chem.* **2015**, *54*, 8396-8400.

(116) Chen, Z.; Wang, G.; Xu, Z.; Li, H.; Dhôtel, A.; Zeng, X. C.; Chen, B.; Saiter, J.-M.; Tan, L., Metal–Organic Frameworks Capable of Healing at Low Temperatures. *Adv. Mater.* **2013**, *25*, 6106-6111.

(117) Manna, K.; Zhang, T.; Greene, F. X.; Lin, W., Bipyridine- and Phenanthroline-Based Metal–Organic Frameworks for Highly Efficient and Tandem Catalytic Organic Transformations via Directed C–H Activation. *J. Am. Chem. Soc.* **2015**, *137*, 2665-2673.

(118) Parsons, S., Introduction to twinning. *Acta Crystallogr. Sect. D* **2003**, *59*, 1995-2003.

(119) Catti, M.; Ferraris, G., Twinning by merohedry and X-ray crystal structure determination. *Acta Crystallogr. Sect. A* **1976**, *32*, 163-165.

(120) Ferguson, A.; Liu, L.; Tapperwijn, S. J.; Perl, D.; Coudert, F.-X.; Van Cleuvenbergen, S.; Verbiest, T.; van der Veen, M. A.; Telfer, S. G., Controlled partial interpenetration in metal–organic frameworks. *Nat Chem* **2016**, *8*, 250-257.

(121) Øien, S.; Agostini, G.; Svelle, S.; Borfecchia, E.; Lomachenko, K. A.; Mino, L.; Gallo, E.; Bordiga, S.; Olsbye, U.; Lillerud, K. P.; Lamberti, C., Probing Reactive Platinum Sites in UiO-67 Zirconium Metal–Organic Frameworks. *Chem. Mater.* **2015**, *27*, 1042-1056.

(122) Braglia, L.; Borfecchia, E.; Maddalena, L.; Øien, S.; Lomachenko, K. A.; Bugaev, A. L.; Bordiga, S.; Soldatov, A. V.; Lillerud, K. P.; Lamberti, C., Exploring structure and reactivity of Cu sites in functionalized UiO-67 MOFs. *Catal. Today* **2016**.

(123) Li, X.; Van Zeeland, R.; Maligal-Ganesh, R. V.; Pei, Y.; Power, G.; Stanley, L.; Huang, W., Impact of Linker Engineering on the Catalytic Activity of Metal–Organic Frameworks Containing Pd(II)–Bipyridine Complexes. *ACS Catal.* **2016**, *6*, 6324-6328.

(124) Gonzalez, M. I.; Bloch, E. D.; Mason, J. A.; Teat, S. J.; Long, J. R., Single-Crystal-to-Single-Crystal Metalation of a Metal–Organic Framework: A Route toward Structurally Well-Defined Catalysts. *Inorg. Chem.* **2015**, *54*, 2995-3005.

(125) Palkovits, R.; Antonietti, M.; Kuhn, P.; Thomas, A.; Schüth, F., Solid Catalysts for the Selective Low-Temperature Oxidation of Methane to Methanol. *Angew. Chem. Int. Ed.* **2009**, *48*, 6909-6912.

(126) Periana, R. A.; Taube, D. J.; Gamble, S.; Taube, H.; Satoh, T.; Fujii, H., Platinum Catalysts for the High-Yield Oxidation of Methane to a Methanol Derivative. *Science* **1998**, *280*, 560-564.

(127) Lersch, M.; Tilset, M., Mechanistic Aspects of C-H Activation by Pt Complexes. *Chem. Rev.* **2005**, *105*, 2471-2526.

(128) Lamberti, C.; Prestipino, C.; Bonino, F.; Capello, L.; Bordiga, S.; Spoto, G.; Zecchina, A.; Diaz Moreno, S.; Cremaschi, B.; Garilli, M.; Marsella, A.; Carmello, D.; Vidotto, S.; Leofanti, G., The Chemistry of the Oxychlorination Catalyst: an In Situ, Time-Resolved XANES Study. *Angew. Chem. Int. Ed.* **2002**, *41*, 2341-2344.

(129) Geary, E. A. M.; Hirata, N.; Clifford, J.; Durrant, J. R.; Parsons, S.; Dawson, A.; Yellowlees, L. J.; Robertson, N., Synthesis, structure and properties of [Pt(2,2?-bipyridyl-5,5?-dicarboxylic acid)(3,4-toluenedithiolate)]: tuning molecular properties for application in dye-sensitised solar cells. *Dalton Trans.* **2003**, *32*, 3757.

(130) Cohen, S. M., Postsynthetic Methods for the Functionalization of Metal–Organic Frameworks. *Chem. Rev.* **2012**, *112*, 970-1000.

(131) Øien, S.; Wragg, D. S.; Lillerud, K. P.; Tilset, M., Di-[mu]-chlorido-bis[(2,2'-bipyridine-5,5'-dicarboxylic acid-[kappa]2N,N')chloridocopper(II)] dimethylformamide tetrasolvate. *Acta Crystallogr. Sect. E* **2013**, *69*, m73-m74.

(132) Palomino, G. T.; Fisicaro, P.; Bordiga, S.; Zecchina, A.; Giamello, E.; Lamberti, C., Oxidation States of Copper Ions in ZSM-5 Zeolites. A Multitechnique Investigation. *J. Phys. Chem. B* **2000**, *104*, 4064-4073.

(133) Groothaert, M. H.; van Bokhoven, J. A.; Battiston, A. A.; Weckhuysen, B. M.; Schoonheydt, R. A., Bis(μ-oxo)dicopper in Cu-ZSM-5 and Its Role in the Decomposition of NO: A Combined in Situ XAFS, UV−Vis−Near-IR, and Kinetic Study. *J. Am. Chem. Soc.* **2003**, *125*, 7629-7640.

(134) Ursby, T.; Unge, J.; Appio, R.; Logan, D. T.; Fredslund, F.; Svensson, C.; Larsson, K.; Labrador, A.; Thunnissen, M. M. G. M., The macromolecular crystallography beamline I911-3 at the MAX IV laboratory. *J. Synchrotron Radiat.* **2013**, *20*, 648-653.

(135) Vaughan, G.; Wright, J.; Bytchkov, A.; Curfs, C.; Gundlach, C.; Orlova, M.; Erra, L.; Gleyzolle, H.; Buslaps, T.; Götz, A., The extension of ID11 for nanoscale and hierarchical characterization. *31st Risø International Symposium on Materials Science: Challenges in materials science and possibilities in 3D and 4D characterization techniques* **2010**, 457-476.

(136) inc., B. A. Bruker APEX3, SAINT, SADABS, XPREP Ver. 2016.5-0 Bruker AXS inc.: Madison, Wisconsin, USA, **2016**

(137) Sheldrick, G., SHELXT - Integrated space-group and crystal-structure determination. *Acta Crystallogr. Sect. A* **2015**, *71*, 3-8.

(138) Allen, F. H.; Johnson, O.; Shields, G. P.; Smith, B. R.; Towler, M., CIF applications. XV. enCIFer: a program for viewing, editing and visualizing CIFs. *J. Appl. Crystallogr.* **2004**, *37*, 335-338.

(139) Westrip, S., publCIF: software for editing, validating and formatting crystallographic information files. *J. Appl. Crystallogr.* **2010**, *43*, 920-925.

(140) Putz, H.; Brandenburg, K. Diamond - Crystal and Molecular Structure Visualization Ver. Crystal Impact GbR, Kreuzherrenstr. 102, 53227 Bonn, Germany, **2016**

(141) Materials Studio Ver. Dassault Systèmes: **2014**

(142) Wu, G.; Rodrigues, B. L.; Coppens, P., The correction of reflection intensities for incomplete absorption of high-energy X-rays in the CCD phosphor. *J. Appl. Crystallogr.* **2002**, *35*, 356-359.

(143) Jakoncic, J.; Di Michiel, M.; Zhong, Z.; Honkimaki, V.; Jouanneau, Y.; Stojanoff, V., Anomalous diffraction at ultra-high energy for protein crystallography. *J. Appl. Crystallogr.* **2006**, *39*, 831-841.

(144) Krause, L.; Herbst-Irmer, R.; Sheldrick, G. M.; Stalke, D., Comparison of silver and molybdenum microfocus X-ray sources for single-crystal structure determination. *J. Appl. Crystallogr.* **2015**, *48*, 3-10.

(145) Ko, N.; Hong, J.; Sung, S.; Cordova, K. E.; Park, H. J.; Yang, J. K.; Kim, J., A significant enhancement of water vapour uptake at low pressure by amine-functionalization of UiO-67. *Dalton Trans.* **2015**, *44*, 2047-2051.

Appendices

A1. Synthesis of reported samples

All Zr-MOFs described herein were synthesized from a solution of $ZrCl_4$, water and organic linker in *N,N*-dimethylformamide (DMF), crystallized in glass vessels at elevated temperature under static conditions unless otherwise specified. In a typical synthesis, the following preparation sequence of the reaction solution was used: DMF was added to a glass beaker and heated to 60 – 100 °C under magnetic stirring. Water, typically 1 – 5 molar equivalents in respect to Zr was added. $ZrCl_4$ was added next, and stirred until a completely clear solution was obtained. Modulator was added next, typically in 10 – 30 molar equivalents in respect to Zr, and the solution was stirred until completely clear. The synthesis solution was then heated to the synthesis temperature, typically 120 °C, still while stirring. Finally, the linker was added, and stirring was maintained until a completely clear solution was obtained.

The solution was then transferred to one or more pretreated, pre-heated reaction vessels, which were then put in an oven and kept at the reaction temperature for the duration of the synthesis. When glass flasks were used, lids such as watch glasses were used to provide a semi-closed atmosphere and prevent unnecessary evaporation of DMF.

Separation and washing

Different procedures were used to recover powder and single crystal MOFs, as single crystals are vulnerable to mechanical degradation from stirring bars. Powder products were recovered by filtration, washed three times in DMF at 100 °C while stirring, washed three times with 2-propanol at room temperature, and dried in air at 150 °C. 2-propanol containing a few percent of water was found to make certain samples of UiO-67 decompose, so dry solvents were always used. The dried powders were stored in sample vials in desiccators.

The product of a single crystal synthesis would typically be found as a layer of intergrown crystallites at the bottom of the flask, and single crystals attached to the inclined walls of the flask. The solution was simply poured off, as the product tended to be stuck to the reaction vessel. Fresh DMF was poured into the vessel, and the crystals were brought into suspension by ultrasonic agitation. The suspension was then heated for at least one hour to bring residual linker and modulator into solution. This was repeated 3 times. After DMF washing, the crystals were washed repeatedly with a dry, less polar solvent to remove DMF, typically methanol, 2-propanol or tetrahydrofuran (THF). The crystals were either kept in this solvent or dried at 150 °C in air and kept in sample vials stored in desiccators.

Synthesis of single crystals of UiO-67-NO_2

10 mL of DMF was heated to 100 °C, and 35 μL (1.9 mmol) of water, 150 mg (0.65 mmol) $ZrCl_4$ and 2.37 g (19.4 mmol) was added and stirred until a completely clear solution was obtained. 214 mg (0.65 mmol) of H_2bpdc-$(NO_2)_2$ was then added, a clear solution was obtained and the solution kept at 120 °C for 48 hours. Weakly yellow crystals were recovered, washed 3 times with hot DMF and 3 times with 2-propanol. The crystals were kept in 2-propanol.

Synthesis of UiO-68-dimethyl (PCN-56)

Single crystals: 30 mL of DMF was heated to 60 °C, and 105 μL (5.81 mmol) H_2O, 451 mg (1.94 mmol) $ZrCl_4$ and 2.37 g (19.4 mmol) benzoic acid was added and stirred until a clear solution was obtained. 670 mg (1.94 mmol) Me_2-H_2tpdc was then added, a clear solution was obtained and the solution was kept at 120 °C for 72 hours. The solid crystalline product was isolated and washed.

Powder: 80 mL of DMF was heated to 135 °C, and 279 μL (15.5 mmol) H_2O, 1204 mg (5.17 mmol) $ZrCl_4$ and 6.31 g (56.7 mmol) benzoic acid was added and stirred until a clear solution was obtained. 1788 mg (5.17 mmol) Me_2-H_2tpdc was then added, a clear solution was obtained and the solution was stirred at 135 °C for 48 hours. The solid crystalline product was isolated by filtration and washed with acetone.

Synthesis of UiO-68-binaphthyl

Single crystals: 24 mL of DMF was heated to 60 °C, and 93 μL (2.58 mmol) H_2O, 241 mg (0.52 mmol) $ZrCl_4$ and 1.73 g (5.17 mmol) 4-nitrobenzoic acid was added and stirred until a clear yellow solution was obtained. 432 mg (0.52 mmol) H_2pbndc was then added, a clear solution was obtained and the solution was kept at 120 °C for 72 hours. The solid crystalline product was isolated and washed.

Powder: 120 mL of DMF was heated to 135 °C, and 279 μL (15.5 mmol) H_2O, 1204 mg (5.17 mmol) $ZrCl_4$ and 8.52 g (56.7 mmol) 4-nitrobenzoic acid was added and stirred until a clear solution was obtained. 2159 mg (5.17 mmol) H_2pbndc was then added, a clear yellow solution was obtained and the solution was stirred at 135 °C for 48 hours. The solid crystalline product was isolated by filtration and washed with acetone.

Synthesis of mixed linker UiO-68

120 mL of DMF was heated to 135 °C, and 335 µL (18.6 mmol) H_2O, 1445 mg (6.20 mmol) $ZrCl_4$ and 15.14 g (124 mmol) benzoic acid was added and stirred until a clear solution was obtained. 1073 mg (3.10 mmol) Me_2-H_2tpdc and 1296 mg (3.10 mmol) H_2pbndc was then added, a clear solution was obtained and the solution was stirred at 135 °C for 48 hours. The solid crystalline product was isolated by filtration and washed with acetone.

Synthesis of single crystals of UiO-69-dimethyl

20 mL of DMF was heated to 60 °C, and 19 µL (1.03 mmol) H_2O, 120 mg (0.52 mmol) $ZrCl_4$ and 1.89 g (15.5 mmol) benzoic acid was added and stirred until a clear solution was obtained. 218 mg (0.52 mmol) Me_2-H_2qpdc was then added, a clear solution was obtained and the solution was kept at 120 °C for 72 hours. The solid crystalline product was isolated and washed.

Synthesis of UiO-67-bpy(Cu)$_{0.2}$

20 mL of DMF was heated to 60 °C, and 47 µL (2.6 mmol) H_2O, 201 mg (0.86 mmol) $ZrCl_4$ and 3.15 g (25.8 mmol) benzoic acid was added and stirred until a clear solution was obtained. 167 mg (0.69 mmol) H_2bpdc and 42 mg (0.17 mmol) H_2bpydc was then added, a clear solution was obtained and the solution was kept at 120 °C for 72 hours. The solid crystalline product was isolated, washed and dried in air at 150 °C. To a solution of 10 mg $CuCl_2 \cdot 2H_2O$ in 2-propanol, a small amount of the obtained single crystals were submerged, and kept at 60 °C for 2 hours. Bright green crystals were obtained, washed repeatedly in THF, and dried in air at 150 °C.

Synthesis of UiO-67-bpy($PtCl_2$)

20 mL of DMF was heated to 60 °C, and 47 µL (2.6 mmol) H_2O, 401 mg (1.72 mmol) $ZrCl_4$ and 7.54 g (62.0 mmol) benzoic acid was added and stirred until a clear solution was obtained. 384 mg (1.55 mmol) Me_2-H_2bpdc and 42 mg (0.17 mmol) H_2bpydc was then added, a clear solution was obtained and the solution was kept at 120 °C for 72 hours. The solid crystalline product was isolated, washed and dried in air at 150 °C. To a solution of 10 mg K_2PtCl_4 in 5 mL DMF, a small amount of the obtained single crystals were submerged, and kept at 100 °C

for 2 hours. Bright yellow crystals were obtained, washed repeatedly in hot DMF, then THF, and dried in air at 150 °C.

A2. SC-XRD experimental notes

Data acquisition

SC-XRD experiments reported herein has been performed on both a laboratory source and at synchrotrons. The in-house instrument is a Bruker D8 Venture diffractometer, with both Mo Kα (λ = 0.71073 Å) and Cu Kα (λ = 1.5418 Å) radiation and a first generation Photon 100 CMOS detector. Synchrotron experiments were performed at the stations I911-3 at MAX2[134] (λ = 0.75 – 0.80 Å) with a Bruker MD2 mini-kappa diffractometer and a Rayonix MARCCD 225 detector, and at ID11 at ESRF[135] (λ = 0.3112) with a single axis home built diffractometer and a Frelon2k CCD detector. All data were collected while keeping the sample at 100 K.

The samples were inspected using a Leica c205 stereomicroscope. The crystals chosen for measurement were in each case representative of the sample as a whole, with respect to morphology, clarity and color.

Data reduction (the determination of sorted and corrected structure factors from a diffraction pattern) was performed with the Bruker APEX3 suite, consisting of SAINT (integration), SADABS (scaling and outlier rejection) and XPREP (structure factor merging and space group determination)[136].

Structure solution and refinement

All of the structures reported herein were solved using SHELXT[137] or SHELXS[77]. The structures were refined with SHELXL[78] using Olex2 as user interface.[106] Cif files were generated with EnCIFer[138] or PublCIF[139]. Molecular graphics were produced with Diamond[140], Olex2[106]and Materials Studio.[141]

Hydrogen atoms' positions and size parameters were generally constrained to the nearest neighboring atom by a riding model. Refinement restraints have been used only when necessary and there has been chemically rational to use them.

The refinements reported in this work make use of dummy atoms to account for poorly defined adsorbates. Additional atoms has not been introduced in the model if the magnitude of $\Delta\rho_{max}$ is comparable to $\Delta\rho_{min}$ in the Fourier difference map, to avoid overfitting due to increased number of free variables. The effect of SQUEEZE was investigated throughout the course of this work, and although lower R-factors could be achieved in most cases, no useful information or increased accuracy is gained in any of the structures.

Detector efficiency correction at I911-3

Initial analysis of data from I911-3 gave poor quality structural models, in which the atomic displacement parameters (ADP) converged to negative, non-physical values. To investigate the possibility of systematic errors, a data set was chosen for statistical analysis. "SOE-SC29" is a data set of 120 frames (0.5° frame width) acquired at I911-3 in May 2015. It consists of 14481 reflections in a resolution range of ∞ - 0.74 Å. Only 14 out of the 1311 unique reflections are missing due to CCD overload. The integrated reflections were scaled using the default settings in SADABS, which resulted in good R_{merge} values (full range R_{merge} of 3.5 %).

It has been reported that the effect of the photons' extended pathway to the phosphor at higher angles in CCD detectors has to be corrected, especially when the absorption coefficient is low.[142] The absorption of X-rays (of a fixed energy) by the sample can be described by a form of the Lambert-Beer law: $I(d) = I_0 e^{-\mu d}$, where d is the path of the photon through the phosphorous, μ is the linear absorption coefficient and I_0 and I are the intensities of the initial and transmitted beam, respectively. This effect becomes very strong when the diffraction angle is high: the photon pathway through the phosphor is twice as long at 60° as it is normal to the detector plane. Thus, the misinterpretation of reflection intensities can be wrong by as much as a factor 2 if there is a disagreement between the physical reality and the assumptions made by the integration algorithm. SAINT uses the following model for angle of incidence correction.

$$\frac{I_{corr}}{I_{obs}} = \frac{p}{1-(1-p)^t}$$

where p is the absorption coefficient read by SAINT and t is the relative thickness of the phosphor at the observed position. The default setting of SAINT ($p = 0.92$) is intended for laboratory instruments with fixed wavelengths, where the CCD phosphor and radiation source are matched to ensure high efficiency. The phosphor in a MARMOSAIC225 (Gd2O2S:Tb) is most efficient for softer X-rays and has an absorption efficiency of 0.8 (in the energy range of 8 – 12 keV) according to the manufacturer. At higher energies, the efficiency drops rapidly, to approximately 0.6 at photon energies of 16.5 keV utilized in the reported experiments.[143] At

ID11, where the same phosphor composition is used, absorption efficiency has previously been measured to 0.513 using a photon energy of 30 keV. Measuring the phosphor efficiency at I911-3 was not possible, but the value could be refined in newer versions of SADABS,[144] which found a phosphor absorption efficiency coefficient of approximately 0.5. The value may also be estimated by regression analysis of the relationship between the expected and calculated intensities, against the expression for angle of incidence correction (Figure 48). However, this method relies on data from a model where the ADP values of Zr are fixed by the user, creating a circular argument. Depending on the input variables, it was possible to obtain absorption coefficients of 0.2 to 0.6.

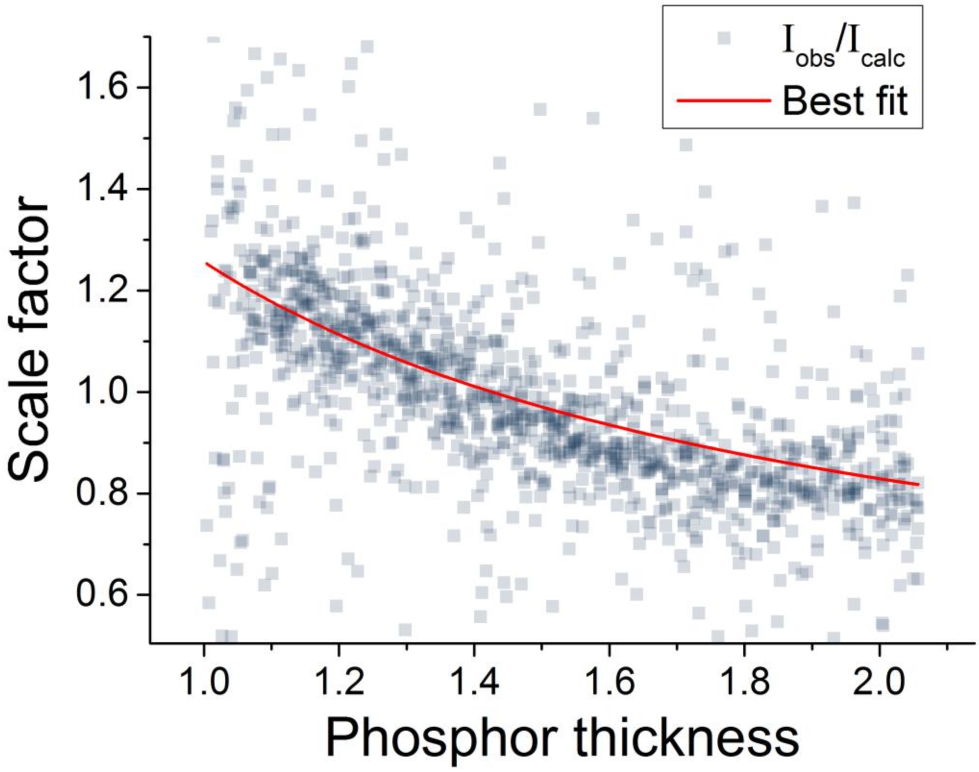

Figure 48. Regression analysis of phosphor absorption in the data set SOE-SC29. The relationship between measured and calculated reflection intensity is plotted against the relative phosphor thickness at the point of incidence, and fitted to expression (4) to obtain the absorpion efficiency, in this case 0.28. The I_{calc} values are obtained by restraining ADP values in the model.

Analysis of the integrated reflection intensities was performed, and summarized in Figure 49. It shows that a major improvement of signal to noise ratio and merging statistics is achieved when applying an absorption coefficient of 0.5 or lower. Using the data sets where $p \leq 0.5$, the refined structure models closely match those determined from data acquired at ID11 and in-house, and reported literature values.[71,124,145] It was decided to refine the absorption efficiency in SADABS for all data sets acquired at I911-3 after applying a static coefficient of 0.5 in SAINT. Although lower values of absorption gave similar results in the structure refinement, and in some cases slightly better reflection statistics, the theoretical value of absorption was emphasized. In addition, the detectors at ID11 and I911-3 uses the same Tb based phosphor, and the absorption efficiency should show dependence on the photon energy. In any case, the impact of changes in the absorption factor below 0.5 resulted in barely noticeable changes in the final models and confidence factors.

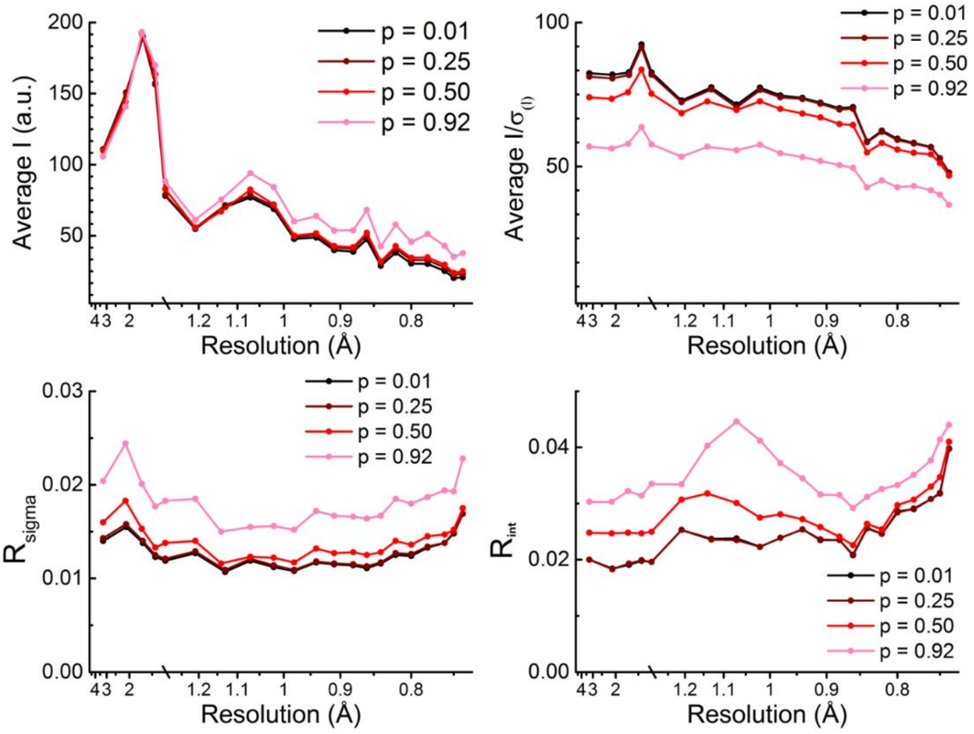

Figure 49. Comparison of data quality acquired at I911-3, but integrated using different values of detector absorption (p).

Source comparison

UiO-67 crystals of similar size were measured at the three X-ray sources used in this work to compare the quality of the D8 Venture data with synchrotron data. Reflection statistics are shown in Figure 50.

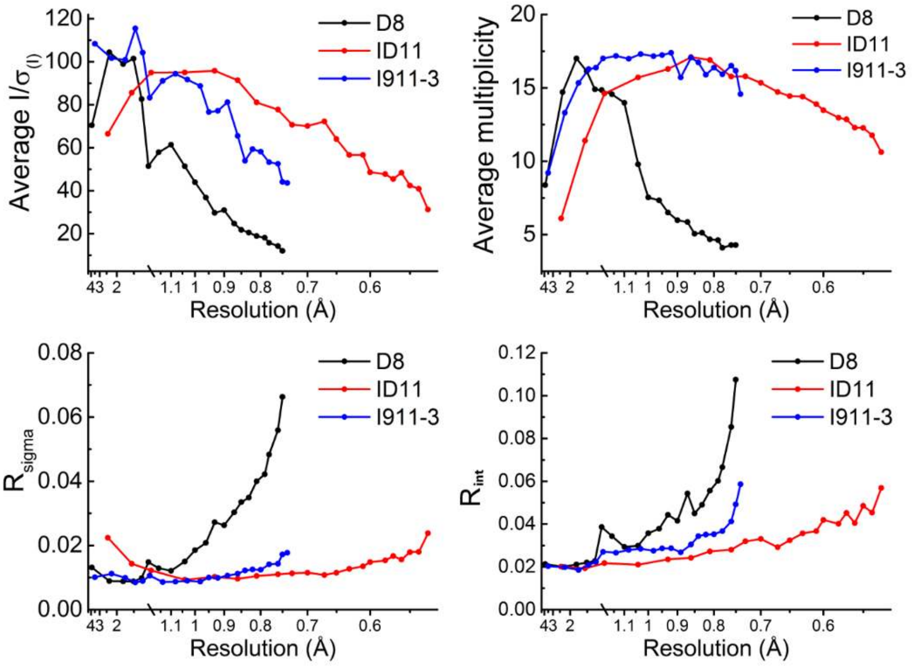

Figure 50. Comparison between reflection data for UiO-67 acquired at the D8 Venture, I911-3 and ID11.

Although higher resolution could be achieved at ID11, the quality of data was superior at I911-3. The structure refinement from I911-3 reaches a remarkably low R_1 factor below 1.5%. (wR_2 < 4%). Summary of the data collection and structure refinement details are found in Table 4.

Table 4.Comparison of crystal data and structure refinement of UiO-67 obtained at the three X-ray sources used in this work.

	Bruker D8 Venture	**ID11 (ESRF)**	**I911-3 (MaxLAB)**
	Laboratory source	Synchrotron	Synchrotron
Crystal data			
Chemical formula	$C_{84}O_{32}Zr_6\cdot 36(C)$	$C_{79.6}H_{22.6}O_{32}Zr_6\cdot 15(C)$	$C_{84}O_{32}Zr_6\cdot 8(C_{0.15})$
M_r	2068.16	2218.1	2134.98
Crystal system, space group	Cubic, $Fm\bar{3}m$	Cubic, $Fm\bar{3}m$	Cubic, $Fm\bar{3}m$
Temperature (K)	100	100	100
a (Å)	26.896 (1)	26.8814 (16)	26.8778 (8)
V (Å^3)	19456 (2)	19425 (3)	19417.0 (17)
Z	4	4	4
Radiation type	Mo $K\alpha$, $\lambda = 0.71073$ Å	$\lambda = 0.31120$ Å	$\lambda = 0.76000$ Å
μ (mm^{-1})	0.35	0.21	0.42
Crystal size (mm)	0.07 × 0.07 × 0.05	0.07 × 0.07 × 0.05	0.06 × 0.06 × 0.04
Data collection			
Diffractometer	Bruker D8 Venture	Single axis	Bruker MD2 microdiffractometer
Absorption correction	multi-scan	multi-scan	multi-scan
T_{min}, T_{max}	0.853, 0.971	0.749, 0.971	0.841, 0.971
No. of measured, independent andobserved [I > 2σ(I)] reflections	11386, 1261, 1153	47073, 3325, 3151	21309, 1305, 1242
R_{int}	0.03	0.028	0.027
$(\sin \theta/\lambda)_{max}$ (Å^{-1})	0.666	0.943	0.675
Refinement			
$R[F^2 > 2\sigma(F^2)]$, $wR(F^2)$, S	0.060, 0.210, 1.20	0.034, 0.103, 1.14	0.015, 0.039, 1.13
No. of reflections	1261	3325	1305
No. of parameters	66	66	59
No. of restraints	0	0	1
H-atom treatment	–	All H-atom parameters refined	μ^3-OH bond length restrained, all other parameters refined
	$w = 1/[\sigma^2(F_o^2) + (0.109P)^2 + 431.748P]$ where $P = (F_o^2 + 2F_c^2)/3$	$w = 1/[\sigma^2(F_o^2) + (0.0683P)^2 + 17.5833P]$ where $P = (F_o^2 + 2F_c^2)/3$	$w = 1/[\sigma^2(F_o^2) + (0.0152P)^2 + 19.622P]$ where $P = (F_o^2 + 2F_c^2)/3$
$\Delta\rho_{max}$, $\Delta\rho_{min}$ (e Å^{-3})	1.12, −1.95	1.14, −2.53	0.35, −0.24

Crystal structure refinement of reported MOFs

Table 5. Experimental details. Data collection and refinement of UiO-67 filled with 2-propanol used for qualitative assessment of adsorption sites in section 3.1.3 on page 32.

	UiO-67 (solvent filled)
Crystal data	
Chemical formula	$C_{296.59}O_{128}Zr_{24}$ (C_{30})
M_r	8735.12
Crystal system, space group	Cubic, $Fm\bar{3}m$
Temperature (K)	100
a (Å)	26.7971 (9)
V (Å^3)	19242.6 (19)
Z	1
Radiation type	synchrotron, λ = 0.76000 Å
μ (mm^{-1})	0.42
Crystal size (mm)	0.06 × 0.06 × 0.04
Data collection	
Diffractometer	Bruker MD2 microdiffractometer
Absorption correction	Multi-scan
	SADABS2014/5 (Bruker,2014/5) was used for absorption correction. wR2(int) was 0.1612 before and 0.1439 after correction. The Ratio of minimum to maximum transmission is 0.6532. The λ/2 correction factor is 0.00150.
T_{min}, T_{max}	0.480, 0.734
No. of measured, independent and observed [$I > 2\sigma(I)$] reflections	15132, 1289, 1222
R_{int}	0.082
$(\sin \theta/\lambda)_{max}$ (Å^{-1})	0.675
Refinement	
$R[F^2 > 2\sigma(F^2)]$, $wR(F^2)$, S	0.055, 0.159, 1.11
No. of reflections	1289
No. of parameters	84
No. of restraints	18
$\Delta\rho_{max}$, $\Delta\rho_{min}$ (e Å^{-3})	0.68, −0.67

Table 6. Experimental details, refinement summary of UiO-67-NO_2 discussed in section 3.2.3 on page 39.

	UiO-67-NO_2
Crystal data	
Chemical formula	$C_{336}N_{48}O_{208.61}Zr_{24}\cdot 6O$
M_r	10619.04
Crystal system, space group	Cubic, $Fm\bar{3}m$
Temperature (K)	100
a (Å)	26.8412 (3)
V (Å^3)	19337.7 (6)
Z	1
Radiation type	synchrotron, $\lambda = 0.75000$ Å
μ (mm^{-1})	0.43
Crystal size (mm)	0.1 × 0.1 × 0.07
Data collection	
Diffractometer	Bruker MD2 microdiffractometer
Absorption correction	Multi-scan
	SADABS2014/5 (Bruker,2014/5) was used for absorption correction. wR2(int) was 0.1074 before and 0.0419 after correction. The Ratio of minimum to maximum transmission is 0.9109. The $\lambda/2$ correction factor is 0.00150.
T_{min}, T_{max}	0.884, 0.971
No. of measured, independent and observed [$I > 2\sigma(I)$] reflections	30664, 1428, 1399
R_{int}	0.029
$(\sin \theta/\lambda)_{max}$ (Å^{-1})	0.704
Refinement	
$R[F^2 > 2\sigma(F^2)]$, $wR(F^2)$, S	0.033, 0.111, 1.26
No. of reflections	1428
No. of parameters	125
No. of restraints	67
$\Delta\rho_{max}$, $\Delta\rho_{min}$ (e Å^{-3})	0.36, −0.49

Table 7. Experimental details, refinement summary of UiO-68-dimethyl (PCN-56) discussed in section 3.2.6 on page 48.

	UiO-68-dimethyl	**UiO-68-dinaphthyl**
Crystal data		
Chemical formula	$C_{520.32}H_{192}O_{128}Zr_{24}\cdot 2.9(C)$	$C_{492}O_{128}Zr_{24}\cdot 16(O)$
M_r	9618.76	10402.2
Crystal system, space group	Cubic, $Fm\bar{3}m$	Cubic, $Fm\bar{3}m$
Temperature (K)	100	100
a (Å)	32.830 (5)	32.612 (7)
V (Å^3)	35385 (16)	34685 (22)
Z	1	1
Radiation type	synchrotron, $\lambda = 0.31120$ Å	synchrotron, $\lambda = 0.76000$ Å
μ (mm^{-1})	0.59	0.24
Crystal size (mm)	0.1 × 0.1 × 0.07	0.08 × 0.08 × 0.06
Data collection		
Diffractometer	Single axis	Bruker MD2 microdiffractometer
Absorption correction	Multi-scan	Multi-scan
	SADABS2014/5 (Bruker,2014/5) was used for absorption correction. wR2(int) was 0.0887 before and 0.0772 after correction. The Ratio of minimum to maximum transmission is 0.7122. The λ/2 correction factor is 0.00150.	*SADABS2014*/5 (Bruker,2014/5) was used for absorption correction. wR2(int) was 0.0996 before and 0.0921 after correction. The Ratio of minimum to maximum transmission is 0.8037. The λ/2 correction factor is 0.00150.
T_{min}, T_{max}	0.530, 0.744	0.780, 0.971
No. of measured, independent and observed [$I > 2\sigma(I)$] reflections	38154, 1841, 1470	13808, 1293, 1133
R_{int}	0.120	0.078
$(\sin \theta/\lambda)_{max}$ (Å^{-1})	0.626	0.556
Refinement		
$R[F^2 > 2\sigma(F^2)]$, $wR(F^2)$, S	0.050, 0.163, 1.17	0.075, 0.257, 1.17
No. of reflections	1841	1293
No. of parameters	68	56
No. of restraints	0	36
$\Delta\rho_{max}$, $\Delta\rho_{min}$ (e Å^{-3})	0.58, −0.65	0.42, −0.56

Table 8. Experimental details and stepwise refinement summary of UiO-69-dimethyl discussed in section 0 on page 49.

		UiO-69-dimethyl	
	$Fd\bar{3}m$	**$F\bar{4}3m$, no twin**	**$F\bar{4}3m$, inversion twin**
Crystal data			
Chemical formula	$C_{624}O_{128}Zr_{24}\cdot 4(O)$	$1.62(C_{648}O_{128}Zr_{24})\cdot 32(C)$	$1.62(C_{648}O_{128}Zr_{24})\cdot 32(C)$
M_r	11987.52	19766.82	19766.82
Crystal system, space group	Cubic, $Fd\bar{3}m$	Cubic, $F\bar{4}3m$	Cubic, $F\bar{4}3m$
Temperature (K)	100	100	100
a (Å)	38.995 (2)	38.995 (2)	38.995 (2)
V (Å^3)	59298 (10)	59298 (10)	59298 (10)
Z	2	1	1
Radiation type	synchrotron, λ = 0.31120 Å	synchrotron, λ = 0.31120 Å	synchrotron, λ = 0.31120 Å
μ (mm^{-1})	0.24	0.11	0.11
Crystal size (mm)	0.20 × 0.20 × 0.20	0.20 × 0.20 × 0.20	0.20 × 0.20 × 0.20
Data collection			
Diffractometer	Single axis	Single axis	Single axis
Absorption correction	Multi-scan	Multi-scan	Multi-scan
	SADABS2014/5 (Bruker,2014/5) was used for absorption correction. wR2(int) was 0.0804 before and 0.0585 after correction. The Ratio of minimum to maximum transmission is 0.7714. The λ/2 correction factor is 0.00150.		
T_{min}, T_{max}	0.574, 0.744	0.574, 0.744	0.574, 0.744
No. of measured, independent and observed [$I > 2\sigma(I)$] reflections	177989, 9985, 8808	180587, 19932, 17091	180587, 19932, 17091
R_{int}	0.034	0.033	0.033
$(\sin \theta/\lambda)_{max}$ (Å^{-1})	0.961	0.961	0.961
Refinement			
$R[F^2 > 2\sigma(F^2)]$, $wR(F^2)$, S	0.122, 0.331, 1.44	0.050, 0.193, 1.08	0.050, 0.192, 1.08
No. of reflections	9985	19932	19932
No. of parameters	100	226	227
No. of restraints	6	55	55
$\Delta\rho_{max}$, $\Delta\rho_{min}$ (e Å^{-3})	2.92, −2.40	1.55, −2.80	1.54, −2.81
Absolute structure parameter		0.497 (8)	0.54 (6)

Table 9. Experimental details, refinement summary of UiO-67-bpy($PtCl_2$) and UiO-67-bpy(Cu) discussed in sections 3.3.2 (page 58) and 3.3.7 (page 69) respectively.

	UiO-67-bpy($PtCl_2$)	**UiO-67-bpy(Cu)**
Crystal data		
Chemical formula	$C_{326.4}Cl_{9.6}N_{48}O_{128}Pt_{4.8}Zr_{24}\cdot 16(C)$	$C_{334}Cu_{1.66}O_{128}Zr_{24}\cdot 12(C)$
M_r	10298.74	8963.68
Crystal system, space group	Cubic, $Fm\bar{3}m$	Cubic, $Fm\bar{3}m$
Temperature (K)	100	100
a (Å)	26.749 (5)	26.6681 (4)
V (Å^3)	19140 (11)	18966.0 (5)
Z	1	1
Radiation type	synchrotron, λ = 0. 75000 Å	synchrotron, λ = 0.76000 Å
μ (mm^{-1})	1.32	0.49
Crystal size (mm)	0.05 × 0.05 × 0.03	0.06 × 0.06 × 0.04
Data collection		
Diffractometer	Bruker MD2 microdiffractometer	Bruker MD2 microdiffractometer
Absorption correction	Multi-scan	Multi-scan
	SADABS2014/5 (Bruker,2014/5) was used for absorption correction. wR2(int) was 0.0915 before and 0.0829 after correction. The Ratio of minimum to maximum transmission is 0.8717. The λ/2 correction factor is 0.00150.	*SADABS2014*/5 (Bruker,2014/5) was used for absorption correction. wR2(int) was 0.1082 before and 0.0860 after correction. The Ratio of minimum to maximum transmission is 0.8391. The λ/2 correction factor is 0.00150.
T_{min}, T_{max}	0.846, 0.971	0.8143, 0.9705
No. of measured, independent and observed [$I > 2\sigma(I)$] reflections	10088, 1287, 1239	16941, 1219, 1115
R_{int}	0.027	0.037
$(\sin \theta/\lambda)_{max}$ (Å^{-1})	0.684	0.665
Refinement		
$R[F^2 > 2\sigma(F^2)]$, $wR(F^2)$, S	0.030, 0.093, 1.13	0.044, 0.140, 1.16
No. of reflections	1287	1219
No. of parameters	86	57
No. of restraints	4	0
$\Delta\rho_{max}$, $\Delta\rho_{min}$ (e Å^{-3})	0.35, −0.22	0.48, −0.54

Table 10. Experimental details, refinement summary of UiO-67-bpy($PtCl_2$) by PSE, discussed in section 3.3.5 on page 65.

	UiO-67-bpy($PtCl_2$) (PSE, 2 weeks)	**UiO-67-bpy($PtCl_2$) (PSE, 6 months)**
Crystal data		
Chemical formula	$0.25(C_{336}H_{192}O_{128}Zr_{24})\cdot 6(O)\cdot 8(CO)$	$C_{336}Cl_{3.84}O_{128}Pt_{0.96}Zr_{24}\cdot 17(C)$
M_r	8273.64	9936.56
Crystal system, space group	Cubic, $Fm\bar{3}m$	Cubic, $Fm\bar{3}m$
Temperature (K)	100	100
a (Å)	26.749 (5)	26.6681 (4)
V (Å^3)	19140 (11)	18966.0 (5)
Z	1	1
Radiation type	synchrotron, λ = 0. 75000 Å	synchrotron, λ = 0.76000 Å
μ (mm^{-1})	0.4	0.61
Crystal size (mm)	0.06 × 0.06 × 0.04	0.06 × 0.06 × 0.04
Data collection		
Diffractometer	Bruker MD2 microdiffractometer	Bruker MD2 microdiffractometer
Absorption correction	Multi-scan	Multi-scan
	SADABS2014/5 (Bruker,2014/5) was used for absorption correction. wR2(int) was 0.0784 before and 0.0685 after correction. The Ratio of minimum to maximum transmission is 0.8705. The λ/2 correction factor is 0.00150.	*TWINABS2014*/5 (Bruker,2014/5) was used for absorption correction. wR2(int) was 0.0867 before and 0.0630 after correction. The Ratio of minimum to maximum transmission is 0.9151. The λ/2 correction factor is 0.00150.
T_{min}, T_{max}	0.8448, 0.9705	0.6828, 0.7461
No. of measured, independent and observed [$I > 2\sigma(I)$] reflections	8719, 1329, 1315	45389, 1289, 1253
R_{int}	0.022	0.063
$(\sin \theta/\lambda)_{max}$ (Å^{-1})	0.693	0.676
Refinement		
$R[F^2 > 2\sigma(F^2)]$, $wR(F^2)$, S	0.052, 0.176, 1.17	0.047, 0.165, 1.12
No. of reflections	1329	1289
No. of parameters	61	79
No. of restraints	2	7
$\Delta\rho_{max}$, $\Delta\rho_{min}$ (e Å^{-3})	1.05, −0.73	1.10, −0.79